DESIGN, PRODUCTION, AND ANALYSIS OF A LOW NOISE NAVIGATION GRADE FIBER OPTIC GYROSCOPE

DÜŞÜK GÜRÜLTÜLÜ NAVİGASYON SEVİYE FİBER OPTİK DÖNÜÖLÇER TASARIM, ÜRETİM VE ANALİZİ

AYLİN YERTUTANOL

PROF. DR. ABDULLAH CEYLAN
Supervisor

Submitted to the Graduated School of Science and Engineering of Hacettepe University as Partial Fulfillment of the Requirements for the Award of the Degree of Doctor of Philosophy in Nanotechnology and Nanomedicine.

2023

To my husband Murat
and
to my son Arat.

ABSTRACT

DESIGN, PRODUCTION, AND ANALYSIS OF A LOW NOISE NAVIGATION GRADE FIBER OPTIC GYROSCOPE

Aylin YERTUTANOL

Doctor of Philosophy, Department of Nanotechnology and Nanomedicine

Supervisor: Prof. Dr. Abdullah CEYLAN

January 2023, 131 pages

Inertial Navigation Systems (INS) use an independent navigation technique for tracking the position and direction of an object relative to a known starting point, orientation or velocity. INSs are used in a wide variety of applications such as aircraft, tactical and strategic missiles, spacecraft, submarines and ships. Interferometric fiber-optic gyroscopes (IFOGs) are widely used in military and industrial applications due to their high sensitivity and stability for the INS. Within the scope of this doctoral thesis, extensive research and development studies have been caried out for the improvement of the noise performance of an IFOG. The reduction of the bias errors caused by environmental changes in IFOG systems is one of the important hot topics in this area. As such, in this study, improvements and alternative structures have been proposed for the reduction of the systematic errors in the critical components of the IFOG to eventually obtain a low-noise IFOG configuration that is critical for high sensitivity. In addition to that, an alternative IFOG configuration minimizing the bias errors caused by environmental changes such as temperature and magnetic field, has been proposed.

For a better performing FOG, it is preferred that the light source, on the main unit, has low noise, high stability, and a wide spectral band. The commonly utilized light sources for FOGs are a fiber-based Amplified Spontaneous Emission (ASE) source and a super-luminescent diode (SLD). Therefore, an optical algorithm has been specifically developed in this study so as to perform optimum spectral measurements of the ASE light source and SLD. The examined optical spectra have clearly revealed that the experimental results are in good agreement with the simulation results. The spectral width of the ASE light source has been improved by 62% from 14.5 nm to 23.5 nm, the temperature dependence of the wavelength has been improved fourfold, and the spectral width has been improved fivefold compared to the minimum configuration of the ASE light source, and thereby the noise of the light source has been minimized.

The crystal polarization feature of the multifunctional integrated optical chip (MIOC) has been increased and with this feature the phase noise due to polarization non-reciprocity of the MIOC has been decreased. The system performances of MIOCs fabricated by Annealing Proton Exchange (APE) and Titanium diffusion (Ti-diffusion) methods have been examined and characterized, and the optimum configuration in terms of noise performance has been obtained by performance tests in IFOG. The system performance of the MIOC fabricated by the APE method and Ti-diffusion method without polarizer have been analyzed and the bias error is reduced more than 20 times by using MIOC fabricated by the APE method.

The fiber optic coil is the heart of the IFOG and it has been designed to minimize the environmental changes that are critical for the IFOG. These parameters, which are optimized to reduce the system noise that directly affects the IFOG performance, are calculated with different variables and their effect on the noise performance is observed. In the scope of this thesis, it is clearly observed that the new adhesive composition is proposed and this composition has improved Young Modulus more than 3 times the basic adhesive formula. With the experimental application of these parameters, low-noise IFOG is obtained. The temperature-dependent bias sensitivity of the fiber optic coil containing adhesive material with high mechanical strength is calculated as 0.16 (°/h)/(°C/min), and by the adhesive composition developed within the scope of this thesis provides an at least 18 times improvement compared to other designs. In this way, solutions are provided for critical points in system installation and contributed to the development of high-precision IFOG production and precision position determination systems.

The Faraday effect is a nonreciprocal error source that affects the performance of IFOG, especially the precision of IFOG. In this thesis, a literature search has been made for a more detailed examination of the Faraday effect on the IFOG, and a new and unique method has been developed to suppress this effect in the fiber optic coil. Our theoretical analysis has shown that two orthogonal polarities caused by the Faraday Effect are effectively suppressed by the proposed method and the experimental results are in good agreement with the expectations of our theoretical analysis. According to the experimental results, the bias error is reduced approximately 20 times from ±9.6 °/h/mT to ±0.5 °/h/mT without any additional part.

In summary, a low-noise and high-sensitivity IFOG has been developed as the output of this study. During this development, many innovative studies have been carried out and these studies have made significant contributions to the relevant literature. The acquisition of this important technology will take Türkiye one step forward in the production of IFOG and will make it one of the world's leading countries in this field.

Keywords: Fiber Optic Gyroscope (IFOG), Sagnac Effect, ASE, SLD, MIOC, Fiber optic coil, Shupe Effect, Faraday Effect

ÖZET

DÜŞÜK GÜRÜLTÜLÜ NAVİGASYON SEVİYE FİBER OPTİK DÖNÜÖLÇER TASARIM, ÜRETİM VE ANALİZİ

Aylin YERTUTANOL

Doktora, Nanoteknoloji ve Nanotıp Anabilimdalı

Tez Danışmanı: Prof. Dr. Abdullah CEYLAN

Ocak 2023, 131 sayfa

Ataletsel Navigasyon Sistemleri (ANS), bir nesnenin bilinen bir başlangıç noktasına, oryantasyona veya hıza göre konumunu ve yönünü izlemek için bağımsız bir navigasyon tekniği kullanır. ANS'ler, uçak, taktik ve stratejik füzeler, uzay araçları, denizaltılar ve gemiler gibi çok çeşitli uygulamalarda kullanılmaktadır. İnterferometrik fiber optik dönüölçerler (IFOD), ANS için yüksek hassasiyetleri ve kararlılıkları nedeniyle askeri ve endüstriyel uygulamalarda yaygın olarak kullanılmaktadır. Bu doktora tezi kapsamında IFOD için kapsamlı araştırma ve geliştirme çalışmaları yapılmıştır. IFOD sistemlerinde çevresel değişikliklerden kaynaklanan sapma hatalarının azaltılması bu alandaki önemli konulardan biridir. Bu çalışmada, yüksek hassasiyet elde etmek için kritik olan düşük gürültülü bir IFOD konfigürasyonu elde etmek için IFOD'u oluşturan birimlerdeki sistematik hataları azaltacak iyileştirmeler ve alternatif yapılar önerilmiştir. Buna ek olarak, sıcaklık ve manyetik alan gibi çevresel değişikliklerden kaynaklanan sapma hatalarını en aza indiren IFOD konfigürasyonu önerilmiştir.

FOD’un daha iyi performans göstermesi için ana ünitelerden biri olan ışık kaynağının düşük gürültülü, yüksek kararlılıklı ve geniş spektral bantlı olması tercih edilir. FOD için yaygın olarak tercih edilen ışık kaynağı, fiber bazlı yükseltilmiş rasgele emisyon (ASE, Amplified Spontaneous Emission) kaynağı ve bir süper ışıldayan diyottur (SLD). Bu doktora tezinde, dönüölçerde kullanılan ASE ışık kaynağı ve SLD’nin optimum spektal ölçümlerini yapmak için bir optik algoritma geliştirilmiştir. Optik spektrumlar incelenmiş ve deneysel sonuçların simülasyon sonuçlarıyla iyi bir uyum içinde olduğu açıkça görülmektedir. ASE ışık kaynağının spektral genişliğinin 14,5 nm’den 23,5 nm’ye %62 oranında iyileştirilmesi, dalga boyunun sıcaklığa bağımlılığının 4 kat, spektral genişliğin ise temel ASE ışık kaynağına göre 5 kat iyileştirilmesi sağlanmış, böylece ışık kaynağının gürültüsü en aza indirilmiştir.

Çok fonksiyonlu entegre optik aygıtın (MIOC, Multifunctinol Integrated Optical Chip) kristal polarizasyon özelliği arttırılmış ve bu özellik ile MIOC’nin polarizasyon karşılıklı olmamasından kaynaklanan faz gürültüsü azaltılmıştır. Tavlanmış Proton Değişimi (APE, Annealed Proton Exchange) yöntemi ve Titanyum difüzyon (Ti-difüzyon) yöntemi ile üretilen MIOC’lerin sistem performansları incelenip karakterize edilmiş ve IFOD’da yapılan performans testleri ile gürültü performansı açısından optimum konfigürasyon elde edilmiştir. APE yöntemiyle üretilen MIOC ve kutuplayıcısız Ti-difüzyon yöntemiyle üretilen MIOC’nin sistem performansı analiz edilmiş ve APE yöntemiyle üretilen MIOC kullanılarak bias hatası 20 kattan fazla azaltılmıştır.

Fiber optik sarım için kritik olan çevresel değişiklikleri en aza indirecek şekilde tasarlanmıştır. IFOD performansını doğrudan etkileyen sistem gürültüsünü azaltmak için optimize edilen bu parametreler, farklı değişkenler ile hesaplanarak gürültü performansı üzerindeki etkisi gözlemlenir. Yeni yapıştırıcı bileşiminin önerildiği ve bu bileşimin Young Modülü’nü temel yapıştırıcı formülüne göre 3 kattan daha fazla iyileştirdiği açıkça görülmektedir. Bu parametrelerin deneysel uygulaması ile düşük gürültülü IFOD elde edilmiştir. Yüksek mekanik dayanıma sahip yapıştırıcı malzeme içeren fiber optik sarımın sıcaklığa bağlı bias duyarlılığı 0,16 (°/h)/(°C/dk) olarak hesaplanmış olup, bu tez kapsamında geliştirilen bu yapıştırıcı bileşimi ile diğer tasarımlara göre en az 18 kat iyileşme sağlamaktadır. Bu sayede sistem kurulumundaki kritik noktalara çözümler sunulmakta ve yüksek hassasiyetli IFOD üretimi ve hassas konum belirleme sistemlerinin geliştirilmesine katkı sağlanmaktadır.

Faraday etkisi, IFOD'un performansını, özellikle IFOD'un hassasiyetini etkileyen karşılıklı olmayan bir hata kaynağıdır. Bu tez çalışmasında, IFOD üzerindeki Faraday etkisinin daha detaylı incelenmesi için literatür taraması yapılmış ve fiber optik sarımda bu etkiyi bastırmak için yeni ve özgün bir yöntem geliştirilmiştir. Faraday Etkisinin neden olduğu iki ortogonal polaritenin önerilen yöntemle etkili bir şekilde bastırıldığı ve deneysel sonuçların teorik analizle iyi bir uyum içinde olduğu teorik analizle gösterilmiştir. Deneysel sonuçlara göre bias hatası herhangi bir ek parça olmaksızın ±9,6 °/h/mT'den ±0,5 °/h/mT'ye yaklaşık 20 kat düşürülmüştür.

Özetle, bu tezin çıktısı olarak düşük gürültülü ve yüksek hassasiyetli bir IFOD geliştirilmiştir. Bu gelişim sırasında birçok yenilikçi çalışma yapılmış ve bu çalışmalar literatüre önemli katkılar sağlamıştır. Bu önemli teknolojinin edinilmesi Türkiye'yi IFOD üretiminde bir adım öne çıkaracak ve bu konuda dünyanın önde gelen ülkelerinden biri haline getirecektir.

Anahtar Kelimeler: Fiber Optik Dönüölçer (FOD), Sagnac, ASE, SLD, MIOC, Fiber Optik Sarım, Shupe-Etkisi, Faraday Etkisi

ACKNOWLEDGEMENTS

I would like to thank my advisor Prof. Dr. Abdullah Ceylan for the thoughtful comments and recommendations on this dissertation.

I also would like to thank Prof. Dr. Ekmel Özbay the director of NANOTAM/ABMN, where I carry out most of my work, for all of the opportunities he provided me and for his fatherly approach.

Many thanks to all of the participants especially Önder Akçaalan, Tuğba Andaç and Erkut Akbaş that took part in the study and enabled this research to be possible.

I would like to express my sincere gratitude to my friends, especially Özlem Şen, Pınar İstanbulluoğlu and Yasemin Aşık who always keep me going, feel my stress the most and always encourage me.

My biggest thanks go to my whole family, my mothers Estalin Karagöz and Zülfiye Yertutanol, my father Numan Yertutanol and my brothers Ercan Karagöz and Kadir Yertutanol, and my sisters Melina Karagöz and Behice Yertutanol for their endless support throughout my life, and for encouraging me during this graduate study.

Finally, I would like to thank my husband Murat Yertutanol for standing by me every day with his never-ending love, patience, and support.

Very special thanks to my son Arat Yertutanol, who joined us when I was studying hard for PhD qualification exam, for giving me unlimited happiness and pleasure.

Aylin YERTUTANOL

January 2023, Ankara

TABLE OF CONTENTS

LIST OF FIGURES

LIST OF TABLES

LIST OF ALGORITHMS

SYMBOLS AND ABBREVIATIONS

Symbols

Ti	Titanium
Au	Gold
$LiNbO_3$	Lithium Niobate
nm	Nanometer
º	Degree
h	Hour
ºC	Centigrade degree
t	Time
π	Pi constant
R	Radius
C_0	Speed of light in vacuum
Ω	Rotation at an ngular speed
L	Fiber length
n	Refractive index
$\Delta\phi$	Phase difference
ΔL	Path difference
A	Average area of the fiber optic coil
D	Fiber optic coil diameter
min	Minute
mT	Militesla
T	Temperature
GHz	Gigahertz
P	Optical Power
ω	Angular velocity
τ	Time spent by the light in the fiber optic coil
fm	Modulation Frequency
sin	Sine
Er	Erbium
Yb	Yterbium
Tm	Thorium
ppm	Parts per million

dB	Desibel
$LiNbO_3$	Lithium Niobate
k_b	Boltzmann’s constant
η	Photodiode efficiency
e	Electron charge
i_d	Dark current of detector
λ	Wavelength
$\Delta\lambda$	Bandwidth the of the light source
α	Longitudinal expansion coefficient of the fiber
s	Length of d_s segment of the fiber
θ	Shupe bias error
µm	Micrometer
N	Total number of turns in fiber optic coil
G	Gauss
β	Birefringence
B	Magnetic field
V	Verdet coefficient
αp	Polarization state coefficient
psi	Pounds per square
MPa	Mega Pascal
THz	Tera hertz
m	Meter
mA	Miliamper
%	Percentage
σ	Sigma
W	Watt
H_2O_2	Hydrogen Peroxide
HF	Hydrofloric Acid
Li	Lithium
H	Hydrogen
V_π	π voltage
Au	Gold
σ	Stress
ε	Strain
P	Pressure
L	Length

E	Modulus of elasticity
C	Carbon black
Pa	Pascal
Si	Silicone
SiH_4O	Silanol
$C_3H_6O_2$	Glycidyl
SiH4	Silane
Al	Aluminium
Ss	Stainles steel
ζ	Faraday rotation per unit length
E	Electrical field

Abbreviations

INS	Inertial Navigation Systems
MEMS	Micro Electro Mechanical Systems
IFOG	Interferometric Fiber Optic Gyroscope
ASE	Amplified Spontaneous Emission
SLD	Super Luminescent Diode
MIOC	Multifunctional Integrated Optical Chip
APE	Annealed Proton Exchange
ANS	Ataletsel Navigasyon Sistemi
IFOD	Interferometrik Fiber Optik Dönüölçer
PID	Proportional Integral Derivative
CW	Clock-wise
CCW	Counter clock-wise
WDM	Wavelength division multiplexer
OCT	Optical Coherent Tomographt
ARW	Angle Random Walk
SF	Scale Factor
PM	Polarization Maintaining
PNR	Polarization non-reciprocity
PM-IFOG	Polarization maintaining IFOG
PIN	Positive- Intrinsic Rezistance -Negative
NB	Noise bins
PS	Parameterized signal

SW	Spectral width
OSA	Optical Spectrum Analyzer
RMS	Root mean square
APC	Angle polished connector
GFF	Gain flattening fiber
LD	Laser diode
TEC	Thermo electric cooler
PVD	Physical vapor deposition
UV	Ultraviolet
DI	De-ionized
PCB	Printed Circuit Board
ASTM	American Society of Testing Materials
BS	British Standards
DIN	Deutsches Institut für Normung
ISO	International Standards Organization
GPTMS	Glycidyloxypropyltrimethoxysilane
VTMO	Vinyltrimethoxysilane
PCF	Photonic crystal fiber
SM	Single Mode
ISP-IFOG	Inverse Symmetric Polarization Interferometric Fiber-Optic Gyroscope
Er-fiber	Erbium Doped Fiber
PZT	Piezo Electric Transducer

1 INTRODUCTION

The working principle of FOGs is based on the direct measurement of the phase difference between two counterpropagating waves through fiber that constitutes a fiber optic coil. The interferometric FOG, as a kind of angular velocity sensor which is based on the Sagnac effect [1], has the advantages of high performance, high precision, and low cost. Therefore, it has broad applications in many fields such as aircrafts, overseas and space application. IFOG, as a kind of FOG is a direct measurement of the phase difference between two propagating waves through fiber that constitutesconstituent a fiber optic coil. IFOG's working principle is also based on the direct measurement of the phase difference between two propagating waves through the fiber that constitutes a fiber optic coil.

Although IFOGs have many advantages, the sensitivity performance of IFOGs depend on the time-dependent variations in the optical path due to under environmental changes, such as thermal perturbations [2], radiation [3] , vibration [4], and Earth's magnetic field [5], [6], [7]. These environmental changes cause an unwanted bias error that should be minimized to improve the sensitivity of IFOG. Therefore, in this study, light source, MIOC, and the fiber coil of IFOG design have been focused on to ultimately manufacture the best performing and most cost effective system.

The studies performed within the scope of this study have been organized in five chapters. Chapter 2 covers the Fundamentals of IFOG configuration. The Sagnac Effect, which is the basis of the IFOG is explained. The optical components that build up the IFOG and their functions have been studied. Broadband light sources such as a super-luminescent diode (SLD) and fiber based amplified spontaneous emission (ASE) light source have been described in detail. The multifunctional integrated optical chip (MIOC) as a substantial component in closed-loop high precision IFOGs and the coil as the heart of the IFOG are explained. Noise sources, effect of noise on the performance of IFOG and the ways to improve the performance under noise are discussed.

The optical and thermal characterizations of the IFOG and the effective solutions are given in Chapter 3. The light source, MIOC and Fiber optic coil are studied in this part.

The light sources, Er-doped fiber ASE and SLD have been simulated, experimentally analyzed and the results are compared. The area of the Er-doped fiber ASE sources has led to research in the fiber optics technology in the foreground in a relatively short period. An ASE source is preferred due to an optical wavelength close to 1550 nm and it provides an efficient and low-noise light in IFOG. Rare-earth doped fibers are also used for applications as sensors and broadband sources for FOGs [8].

In this study, the spectrum of an ASE source with Er-doped fiber was measured and the results were compared with a commercial SLD (Super Luminescent Diode) source for FOG applications. The temperature dependent wavelength characterization of ASE source is studied. The ASE source is analyzed by measuring the wavelength under temperature changes. The temperature characterization of Er-doped all-fiber ASE source and SLD have been investigated. The spectral width of the ASE light source has been improved by 62 %, the temperature dependence of the wavelength has been improved fourfold, and the spectral width has been improved fivefold compared to the minimum configuration of the ASE light source. According to the results, an all-fiber ASE source has shown a more stable temperature response in the range of -40°C to 85°C.

The system performances of MIOCs fabricated by Annealing Proton Exchange (APE) and Titanium diffusion (Ti-diffusion) methods have been examined and characterized, and the optimum configuration in terms of noise performance has been obtained by performance tests in IFOG. The FOG performance with two MIOCs fabricated by the APE method and Ti-diffusion method without polarizer have been analyzed and the bias error is reduced more than 20 times by using MIOC fabricated by the APE method.

Another important part, which was investigated in Chapter 3, is a fiber optic coil. The focus is on the characterization of a fiber optic coil that includes the effect of adhesive composition. A novel adhesive composition is developed, and a high Young Modulus for an adhesive with the new composition is obtained within the scope of this study. The bias sensitivity of the fiber optic coil, which contains an adhesive material with high mechanical strength, for which temperature-dependent rate measurements are made, is calculated as an average of 0.16 (°/h)/(°C/min) over the entire temperature range. It has been clearly observed that it has improved at least 18 times compared with the other designs. Since the fiber optic coil contains an adhesive material with high mechanical strength, the rate measurement resulting from mechanical stress against temperature change is at least tenfold greater when compared with the results of fiber optic coil produced with a mixture of base adhesive and a drying agent or with the results of a fiber optic coil without any adhesive. It is clearly observed that the adhesive composition proposed by the author has improved at least eighteenfold compared with the other design.

Chapter 4 focuses on another original work, which improves the performance of fiber optic coil under a magnetic field. The chapter summarizes the Faraday Effect Induced bias error on the performance of IFOG, gives the solutions that can be found in the literature, and proposes an alternative solution to reduce this unwanted bias error. The proposed solution has been theoretically analyzed and simulation results for this solution have been given. The measurement results have been provided. This achievement is clarified thorough theoretical and experimental study of the Faraday-effect-induced bias error in a FOG. According to the experimental results, the bias error is reduced approximately 20 times from ±9.6 °/h/mT to ±0.5 °/h/mT. The proposed solution has been compared with the literature in terms of the cost effectiveness, area minimization (minimum component), ease of manufacturability, and performance improvement.

Chapter 5 summarizes the overall work carried out during this thesis study and clarifies the contribution of this work to the relevant literature. Discussions and recommendations for future studies are also given.

2 FUNDAMENTALS OF THE FIBER OPTIC GYROSCOPE

In this chapter, the working principle of IFOG, namely the Sagnac Effect, is defined first, and then the configuration of IFOG is given. Thereafter, the fundamental elements of IFOG are explained with their working principles and important properties. Finally, the limiting factors for the performance of IFOG, namely error mechanisms, are analyzed. While analyzing the error mechanisms, the methods that can be found in the literature for correcting these errors are also summarized in this chapter. It should also be noted that these correcting mechanisms have their own limitations, and improvements for correcting mechanisms of these errors are proposed as an original contribution of the author in Chapter 4 of this thesis.

1.1. Sagnac Effect

The working principle of IFOG is based on the Sagnac effect. The Sagnac effect was observed in 1913 with the French Studied and demonstrated by George Sagnac. The Sagnac effect is described as the relative phase differences between two counterpropagating waves that have traveled an optical light path in the opposite direction in a fiber optic coil. When the fiber optic coil rotates about its symmetry axis, this these two counterpropagating waves in the fiber optic coil experience a phase shift and this can be detected by a photodetector. The phase difference between two counterpropagating waves are transferred as the detected rotation of the gyroscope.

The rotating disk is shown in Figure 2.1. For a given point on perimeter, labeled 1, identical waves propagate in the clockwise and counter-clockwise directions [9]. If the initial angular velocity is null, photons that travel at the speed of light in vacuum c_0 will arrive at starting point 1 after a trip length of 2πR in time $t = 2\pi R/c$.

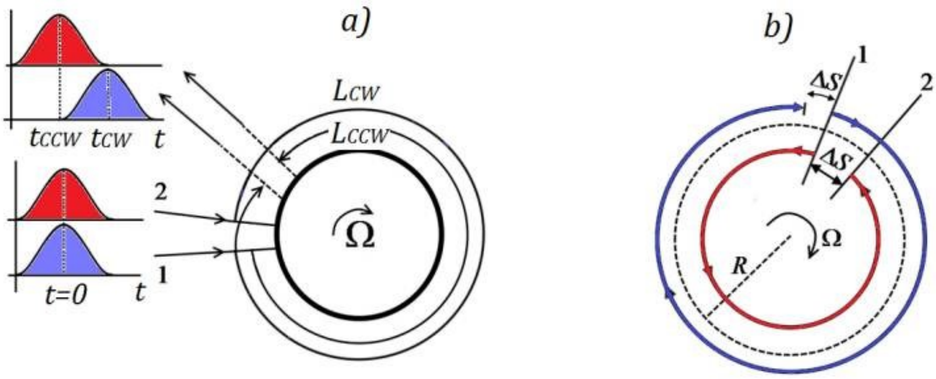

Figure 2.1. In a disk rotating with a CW angular velocity (a) different rotation induced optical paths of the clockwise and counter-clockwise CCW optical beams, LCW and LCCW, respectively; and (b) identical difference, ΔS, between the rotation induced optical paths of the clockwise and counter-clockwise optical beam, and the standing optical path

If the initial angular velocity is not null, the photons that propagate in the counter-clockwise direction, called CCW, will arrive at the starting point, now called 2, due to the motion caused by the rotation, after a trip length of L_{CCW}, shorter than $2\pi R$, given as Equation 2.1

$$L_{CCW} = 2\pi R - R\Omega t_{CCW} = c_{CCW} \cdot t_{CCW} \qquad 2.1$$

where $R\Omega$ is the tangential angular speed of the ring and t_{CCW} is the time to cover the distance L_{CCW} that is equal to the product of speed of light in counter-clockwise direction c_{CCW} and time t_{CCW}. In vacuum, it results in $c_{CCW} = c_0$.

In the same way, the clockwise photons, called CW, will arrive at the starting point, now called 2, due to the motion caused by the rotation, after a trip length of L_{CW}, longer than $2\pi R$:

$$LCW = 2\pi R - R\Omega tCW = cCW \cdot tCW \qquad 2.2$$

The different sign of $R\Omega$ is related to the angular velocity: Indeed, by supposing a clockwise rotation, clockwise photons cover a longer distance than counter-clockwise ones.

If light propagates in a medium characterized by a refractive index *n* [6], by considering the relativistic composition of propagation speed and tangential speed of medium, c_{CCW} can be rewritten as:

$$c_{ccw} = \frac{\frac{c_0}{n} + R\Omega}{1 + \frac{R\Omega}{nc_0^2}} = \frac{c_0}{n} + R\Omega\left(1 - \frac{1}{n^2}\right) + \cdots \qquad 2.3$$

While c_{CW} is:

$$c_{cw} = \frac{\frac{c_0}{n} - R\Omega}{1 - \frac{R\Omega}{nc_0^2}} = \frac{c_0}{n} - R\Omega\left(1 - \frac{1}{n^2}\right) + \cdots \qquad 2.4$$

where the right side of the previous expressions are the Taylor series explanation of the first term.

Now, $\Delta\tau$ is equal to:

$$\Delta t = t_{CW} - t_{CCW} = 2\pi R\left[\frac{2R\Omega - (c_{CW} - c_{CCW})}{c_{CW} \cdot c_{CCW}}\right] \qquad 2.5$$

Substituting Equations (2.3) and (2.4) and into Equation (2.5) the following is obtained:

$$\Delta t = t_{CW} - t_{CCW} = 2\pi R\left[\frac{2R\Omega - 2R\Omega\left(1 - \frac{1}{n^2}\right)}{\frac{c_0}{n^2}}\right] = \frac{2\pi R 2R\Omega}{c_0^2} = \frac{4A\Omega}{c_0^2} \qquad 2.6$$

The $\Delta\tau$ results should be the same as the in vacuum case, and due to this, the time difference corresponds to a phase shift of

$$\Delta\Phi = \frac{2\pi\Delta t}{\frac{\lambda_0}{c_0}} = \frac{2\pi\Delta t}{\frac{\lambda}{c}} = \frac{8\pi A}{\frac{\lambda_0}{c_0}}\Omega \qquad 2.7$$

The rotation of the fiber optic coil creates a phase difference (Δϕ) between the two counterpropagating waves. If there is a rotation at an angular speed Ω, due to the Sagnac effect, the counter propagating waves will have a path difference of ΔL, given by:

$$\Delta L = \frac{\Delta\phi}{2\pi}\lambda = \frac{4A}{c_0}\Omega \qquad 2.8$$

generating an interference fringe shift expressed as:

$$\Delta z = \frac{LD}{\lambda c}\Omega \qquad 2.9$$

or the phase difference (Δϕ) is given in Equation-2.10. The rotation of the fiber optic coil creates a phase difference (Δϕ) between the two counterpropagating waves

$$\Delta\Phi = 2\pi\frac{LD}{\lambda c}\Omega \qquad 2.10$$

Here, L is the fiber optic coil length, D is the fiber optic coil diameter, λ is the operating wavelength, c is light velocity in vacuum and Ω is the rotation rate. Based on this Equation 2.10, it can be seen that the sensitivity of IFOG can be improved by increasing the total coil length *L* and increasing the fiber optic coil diameter or decreasing the wavelength.

1.2. Configuration of a Fiber Optic Gyroscope

IFOGs using a fiber optic coil as the optical path can be designed in two different configurations as an `open-loop' or 'closed-loop' gyroscope. The optical phase modulation technique is used in both configuration by applying a modulating voltage, and a consequent optical pathlength variation due to the elasto-optic effect are generated.

Open loop IFOG mainly uses piezoelectric modulator (PZT) for modulation and demodulation, and it is mainly used in low-precision fields. Closed loop IFOG is mainly used in the high precision fields. In the closed loop IFOG, MIOC is used instead of PZT because the modulation frequency of PZT is too low to be used as a closed-loop feedback control component and it is possible to produce stable and controllable sensors, by using MIOC in a closed loop configuration.

In ‘open-loop’ systems, PZT is directly integrated on the fiber optic path. With this, it is possible to have a cost reduction of approximately 40% when we compared to the close-loop system. A scheme of the ‘Open Loop’ IFOG configuration is given in Figure 2.2.

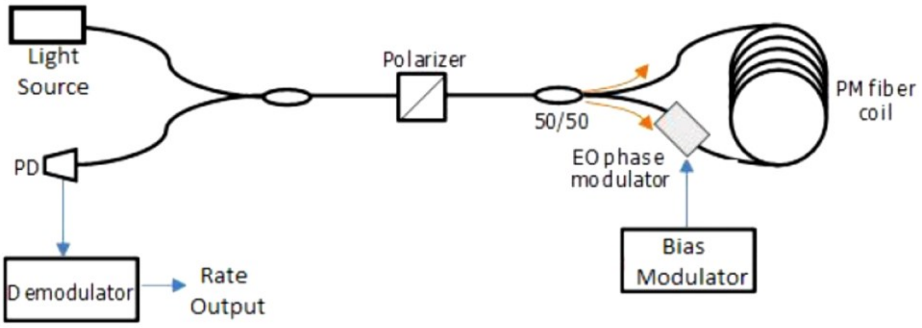

Figure 2.2. ‘Open Loop’ IFOG configuration

MIOC has higher modulation bandwidth (GHz) than the original all-fiber scheme (a phase of modulation is achieved by winding a length of fiber on a PZT piezoelectric ceramic cylinder), and better amplitude-frequency characteristics, which can realize multi-harmonic signals modulation (such as square wave, step wave, etc.), and is suitable for various closed-loop signal processing schemes. Closed loop systems provide high sensitivity compared to open loop systems due to the feedback alghorithm. ‘Closed loop’ IFOG diagrams are given in Figure 2.3.

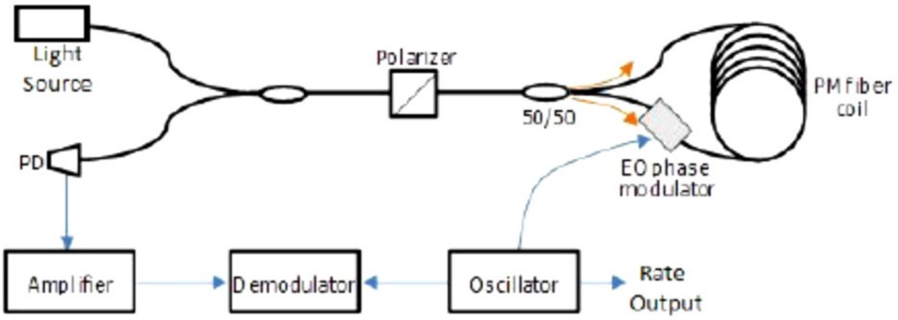

Figure 2.3. ‘Closed loop’ IFOG configuration

When the fiber optic coil is rotated, clockwise or counterclockwise, a phase shift occurs between counterpropagating waves. This phase shift (Sagnac effect) is detected by the photodetector and the output signal is sinusoidally varied. The Proportional Integral Derivative (PID) controller generates a signal that compensates for the Sagnac effect. Therefore, while the Sagnac effect is eliminated, the angular velocity change information resulting from the phase shift is also obtained.

The signal produced at the output of the PID controller is passed through a low pass filter. This signal is then converted into quanta levels with the help of a quantizer and applied to the phase modulator. At this stage, the PID controller compensates for the Sagnac effect and forces the system to work in balance. Photodetector output signal of the system in Figure 2.3 is expressed as Equation 2.11,

$$\mathrm{Pd} = 0.5\mathrm{P0}(1 + \cos(\Delta\Phi\mathrm{s}\,(\mathrm{t}) - \Delta\Phi\mathrm{m}(\mathrm{t})) \tag{2.11}$$

Here, $\Delta(\boldsymbol{t})$ indicates the Sagnac phase shift and $\Delta\boldsymbol{\Phi m}(\boldsymbol{t})$ indicates the bias phase change in phase modulation. Sine-shaped bias phase modulation $(\boldsymbol{t})$ can be expressed as Equation 2.12.

$$\Phi m(t) = \Phi 0 \sin(\omega m t) \tag{2.12}$$

Here ωm=2πfm and fm are the modulation frequency of the modulator. In addition to the Sagnac phase shift caused by the physical rotation of the gyroscope, a bias phase change will occur due to phase modulation. Bias phase change $\Delta(\boldsymbol{t})$ can be calculated as Equation 2.13.

$$\Delta\Phi m(t) = \Phi 0\,[\sin(\omega m t) - \sin(\omega m t - \omega m \tau)] \tag{2.13}$$

While one of the lights traveling in two opposite directions in the gyroscope coil passes through the modulator at time t, it encounters the other light at the modulator at time t- τ.

τ=nL/c is the time spent by the light in the fiber optic coil. n is the effective refractive index of fiber, L is the total length of fiber optic coil and c is the vacuum speed of light.

Maximum angular velocity sensitivity, which has the π/2 phase shift when the gyroscope is stationary, is provided in the phase modulator.

IFOG designs with square-wave phase modulation can be programmable with four-point, five-point or six-point phase modulation techniques to improve the accuracy of the gyroscope [10–12]. In general, the square-wave modulation is used as a bias modulation technique for maximum sensitivity. Square-wave modulation enables shifting the working point of the IFOG when the working point of the IFOG is ± π/2. When the system is subjected to a rotation rate, the square-wave curve, which has peak-to-peak amplitude, is proportional to the rotation speed value [13].

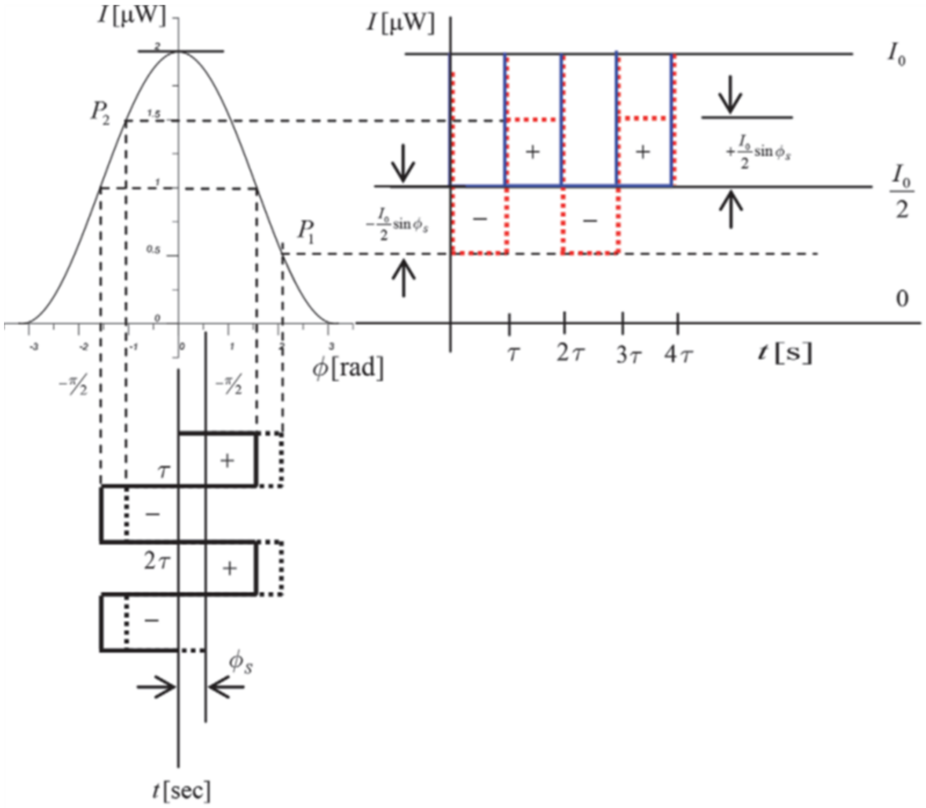

Figure 2.4. The interference of the IFOG with square-wave phase modulation

Therefore, the calculation of effective phase shift induced by the phase modulation process between CW and CCW optical waves at the output of fiber optic coil after their respective roundtrip can be expressed as follows:

$$\Delta\Phi(t) = \Phi\text{CCW}(t) - \Phi\text{CCW}(t) \qquad 2.14$$

here $\Delta\boldsymbol{\Phi}(\boldsymbol{t})$ represents the time waveform of applied phase modulation and τ is the transit time around the fiber optic coil. To obtain the result at Equation 2.14, it has been assumed that CW and CCW waves enter the fiber optic coil at opposite ends. Then, in the case of square-wave phase modulation, as represented in Figure 2.4, analytics give a constant phase values, namely, $\pi/2$ (continuous black wave) when no-rotation is applied to the system.

However, when a non-zero rotation is applied, a phase difference equal to $\phi\Phi$, a Sagnac phase shift must be added to the phase. The explanation of the blue and red lines output response curves of photo-detector, which are given in Figure 2.4, is as follows. When the rotation rate is equal to zero, the projection of the points of the input square waveform on the response curve of the interferometer gets a pectinate-shaped output waveform as given in Figure 2.4. The phase modulator gives the zero intensity for the phase shift measured between counter-propagating waves with a feedback loop as given in Equation 2.15.

$$P(t) = {}^{I_0}\!/_{2}\,[1 + cos(\Delta\phi_s(t) + \Delta\phi_m(t) - \Delta\phi_f(t))] \qquad 2.15$$

A feedback phase shift driven by the modulator depends on the transient time τ and is expressed as shown in Equation 2.16 and when phase shift is applied as a digital ramp signal, each ramp waits for coil transition time in each step, goes up until the Sagnac phase shift and the resulting feedback phase shift is given in the Equation 2.17.

$$\Delta\phi_f(t) = \phi_f(t) - \Delta\phi_f(t - \tau) = -\Delta\phi_s(t) \qquad 2.16$$

$$\phi_f(t) = \phi_f(t - \tau) - \Delta\phi_s(t) \qquad 2.17$$

The digital ramp that needs to be reset at a non-infinity point can generate an error unless the reset amplitude is equal to an integer multiple of 2π. The reset amplitude can be set to any 2π multiples up to the maximum applicable voltage to the phase modulator [14].

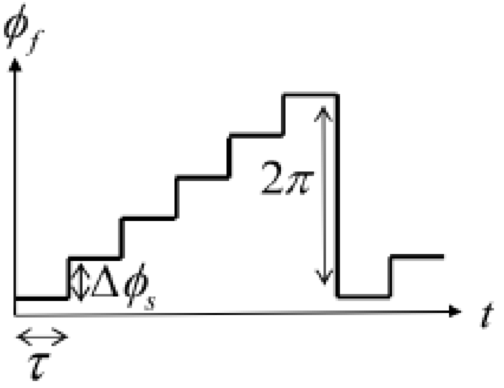

Figure 2.5. Digital step ramp for the closed loop.

1.3. Fundamental Elements of IFOG and Their Working Principles

1.3.1. Light Source and Optical Detection

The light source of the fiber optic gyro is one of the most basic units in which the light traveling through the optical system is emitted. The basic parameter of the fiber optic gyroscope scale factor is directly related to the wavelength of light source and, therefore the light source characteriztion of FOG is critically important for the high-performance gyros. IFOG systems need as low noise, high wavelength stability, and broadband light source as possible. In this part, a broadband light source with a known Kerr-effect and low backscattering will be used to provide the best performance. Typical broadband light sources, SLD) and fiber-based ASE light source are two widely used light sources in IFOGs. For a different wavelength regime the gain fiber can be selected as Yb-doped, Er-doped, and Th-doped fibers for 1000 nm, 1550 nm and 2000 nm respectively. For the minimum optical loss, the optical spectrum region around 1500 to 1650 nm is preferred. In IFOG systems generally, telecom wavelength (1550 nm) is used due to their being low loss, low cost and easy to find.

SLD is a semiconductor device that emits a low-coherence light of a broad spectrum and also high brightness for the desired wavelength. SLD has a compact design as a light source with broad bandwidth and short coherence length, all solid state and low drive voltage requirements and SLD is widely used as a light source for IFOG in the literature. SLDs have similar manufacturing processes as semiconductor laser diodes. Although such light sources provide a broadband and high-intensity light output, which are known to prevent problems such as Kerr Effect and Rayleigh Scattering, their weak wavelength stability under temperature changes creates a disadvantage for the use of SLD. Moreover, their wavelength stability and scale factor stability are not sufficient for high performance IFOGs. However, the poor wavelength stability of SLD under thermal changes such as 400 ppm/°C is an important disadvantage for high performance IFOG systems [15–17].

A fiber-dopped ASE light source configuration has a more complex design than SLD. A fiber-doped ASE light source has a couple of optical components such as a pump laser diode, a gain fiber, a wavelength division multiplexer (WDM) and an isolator to obtain light at the desired wavelength.

An ASE light source that has a central wavelength at 1550 nm with a 15 nm broadband is used to eliminate the interference errors due to splice angle errors, back reflections and poor quality of polarization maintaining optical components.

Various optical components are used to transmit the optical signal from the light source to the MIOC and to detect the phase difference in the signal coming from the sensor coil. A detection unit consisting of coupler, polarizer and photodector, transmits the optical signal from the light source to the sensor unit to the sensor unit consisting of fiber optic coil and MIOC. The end of this coupler, which is on the input side according to the light's input direction, directs the signal from the sensor unit, which contains the rotation information, to the photodetector, depending on the interference in the fiber optic coil.

1.3.2. MIOC

Integrated optics technology can improve the performance and compactness of IFOGs. The multifunctional integrated optical chip (MIOC) is a substantial component in the closed-loop IFOG configuration that widely used in high precision IFOGs. It combines a waveguide with a 3 dB Y-coupler for the coil splitter, wideband phase modulators, and a >40 dB the polarizer [18], [19], [20]. The MIOC has a high modulation bandwidth (GHz) that can realize multi-harmonic signals modulation (such as square wave, step wave, etc.), and is suitable for various closed-loop signal processing schemes. Moreover, the polarizer, coupler, and phase modulator are integrated on the same substrate, which reduces the size of the gyroscope, is beneficial to mass production, and leads to a cost reduction. Lastly, the polarization extinction ratio of the MIOC is around 40-90 dB, which can effectively suppress the polarization related error of the IFOG. The MIOC is connected to other optical components through optical fibers in high-precision fiber optic gyroscopes especially navigation grade gyroscopes.

The MIOC has a Y-shaped waveguide that splits the light beam coming from a light source into two arms and splits the light beams that propagate through the fiber optic coil [21]. As a phase modulator, the MIOC changes the phase velocity of the light, which propagates in one arm of the Y-shaped waveguide, by changing the refractive index with a voltage applied to the modulator electrodes [22]. By the change of the refractive index of the one arm, the phase shift occurs between the two light beams. $LiNbO_3$ is the most suitable material for MIOC fabrication, due to its unique electro-optic and stable chemical properties [23], [24] . There are two main waveguide fabrication techniques on $LiNbO_3$. One is the titanium (Ti) diffusion method and the other one is annealed proton exchange (APE) method [25]. These fabrication methods of the MIOC are developed and the detailed characterization results are recorded in Section 3.2.

After the MIOC fabrication process, the polarization-maintaining (PM) fiber pigtails are aligned to the input and the output arms of the LiNbO3 waveguide [23], [26], [27] by an ultraviolet-curable epoxy that has a special optical property [24].

1.3.3. Fiber Optic Coil

Among the many factors affecting the performance of the Fiber Optic Gyroscope (IFOG) is that the sensing fiber optic coil is the most critical component that determines the measurement sensitivity of the IFOG. The structure of fiber optic coil is mainly composed of a spool, polarization maintaining fiber and an adhesive. The fiber spool supports the fiber layers and the fiber is fixed by the curing adhesive. The spool can be removed to obtain a frameless fiber optic coil, after the fiber is wound around a spool. To the fiber optic coil there are supplied two counter-propagating lights, one light beam propagating in the clockwise direction through the fiber optic coil and the other beam propagates in the counterclockwise direction. Rotation of the fiber optic coil induces a phase shift between the two counter-propagating lights due to the Sagnac effect. The rotation induced phase shift is used to measure the angular velocity of a part to which the fiber-optic gyroscope is attached.

In order to accurately measure the phase shift, the light propagating in the fiber must be subjected to the same conditions along the whole optical path; but the environmental factors such as temperature change, external vibration, magnetic field and mechanical stresses make regional differences in the index of the light beams in the counterpropagating direction. This unwanted phase difference is known as the Shupe effect and the detailed description of this effect has been described in Section 1.5. Symmetrical winding pattern such as quadruple, octupole, hexapole or reverse-hexapole winding patterns with panda type PM fiber is preferred to minimize the Shupe Effect. The most common winding pattern in the literature is the quadrupole winding pattern that provides symmetry and a good stress performance in the fiber optic coil. In the "Progress in Navigation-Grade IFOG Performance" study, it is stated that the Shupe error decreased with the square of the number of layers compared to cylindrical winding (starting from one end of the winding to the end) when using the quadruple winding pattern [28]. This result is a theoretical result and the superiority of the quadruple winding to the cylindrical winding has been seen in the simulations. According to the quadrupole winding pattern, the fiber optic coil structure has a special design that repeats every four layers. There are two similar quadrupole winding patterns that are shown in the schematic view of the cross section of the patterns in Figure 2.6.

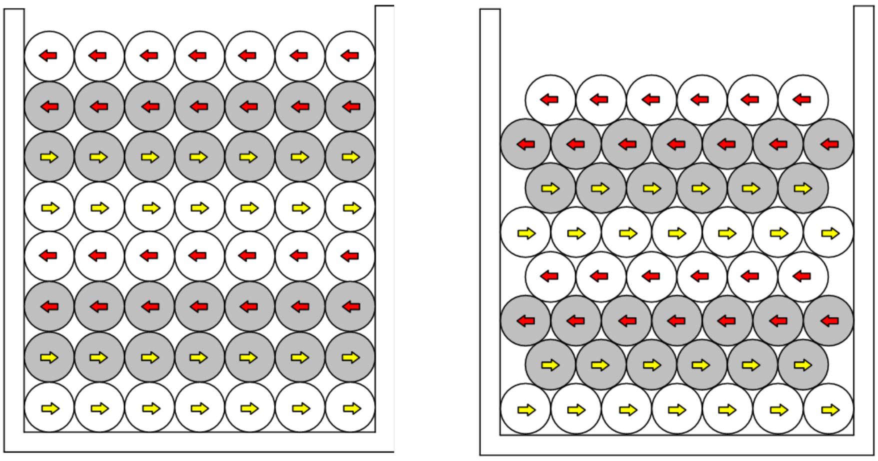

Figure 2.6. Schematic view of the cross section for the quadrupole winding pattern

The figure on the right side represents the basic quadrupole winding pattern and the one on the left represents the modified quadrupole winding pattern. The circles in Figure 2.6

represent an optical fiber cross section. The circles shown in bold include the left fiber end; and the optical fiber indicated in white by means of the right fiber end.

The fiber optic coil, which is the basic component that determines the performance of the IFOG, must be produced in such a way that the counter-propagating light from the optical fiber forming the coil is exposed to the same environmental conditions inside the fiber optic coil. At that point, the surface quality of the fiber optic coil is quite important. While there is a gap or jamming error between fiber turns or layers in the fiber optic coil winding process, the bias error or 3D inhomogeneous distortions occur in the fiber optic gyroscope detailed in the next section. In the study published by Z. Li et al. in 2013, winding asymmetry is associated with fiber length and number of layers, and if the fiber optic coil length decreases and the number of layers increases, the winding asymmetry will decrease [29].

This improvement does not always provide a complete solution. It is emphasized that trimming should be applied for the thermal symmetry in practice [30]. It is stated that the fibers remaining from both ends of the fiber optic coil after trimming should be located as close to each other as possible in order to minimize both diametrical and axial errors [31].

In order to increase the fiber optic coil quality, errors occurring in the coil can be detected with optical coherent tomography (OCT) or crosstalk analysis [32] . The adhesive used should have a viscosity of less than 25000 cp and silver particles should be added to increase thermal conductivity. Besides silver, “Gelest SIT7900.1 additive for increasing the working time and “Dow Q9-6300” additive for increasing the adhesion are recommended [33]. The use of carbon black doped silicone increases the thermal conductivity in the fiber optic coil, thereby reducing the gyroscope constant error considerably [34]. By adding 10-25% air-bubbles such as Expancel into the adhesive, an adhesive is obtained that will absorb the applied pressure from the optical fiber and coil material [35]. In addition to the above solutions, the author has an original adhesive design that increases the Young modulus and also the proposed adhesive decreases the temperature sensitivity of the bias that improves the temperature performance of the fiber optic coil. The proposed adhesive is used in the fiber optic coil and the performance of the fiber optic coil is measured, the details of which can be found in Section 3.3.2 and 3.3.3.

Since the expansion coefficients of the spool material and the optical fiber are similar, the bias error due to temperature is reduced. However, reducing the spool contact with the fiber optic coil will also reduce this error. For this, a metal such as titanium should be chosen as the spool material, or the application of a gap or thin layer of soft silicon, preferably between the spool roller and the fiber optic coil, at this increases the performance [36]. In one study, it is stated that putting a buffer layer between the flange of the spool and the fiber optic coil, is a good solution to reduce the pressure from the outside. However, having some space between the spool roller and the fibers forming the coil is a suitable method to reduce this effect [37].

It has been stated that the thickness of the buffer layer that will form on the flange of the spool can preferably be between 100 and 600 μm [38]. In one study, in order to equalize the lengths of the fibers between the fiber optic coil and the MIOC and to ensure that the fibers are in the same direction, the one end of fiber optic coil bent 180° on the coil surface is preferably stated to have been withdrawn. The fibers between the fiber optic coil and MIOC are properly wound on the fiber optic coil outer surface and the fibers between the fiber optic coil and MIOC is fixed with silicon adhesive [39]. The use of carbon black doped silicone adhesive significantly reduces the gyroscope bias error due to vibration and the thermal effect [34].

1.4. Performance of IFOG and Error Mechanism

Any effect that distorts the reciprocity of light in an IFOG causes an error in the output signal, which may be noise or drift. These errors are indistinguishable from a rotation rate and, therefore may be misinterpreted as a rate signal. Understanding the primary error sources of IFOG allows these errors to be minimized with several alternative design solutions. This thesis focuses on closed-loop IFOG and its performance. The minimum closed-loop configuration consists of four main groups as a light source, optical detection unit, MIOC and coil. Fiber optic gyroscopes, like all other sensors, measure with a certain error and the amount of these errors determines the gyro performance. These error mechanisms are scale factor stability, Angle Random Walk (ARW) and bias errors. These will be detailed in following paragraphs.

The scale factor in the gyroscope is the ratio of the gyro output per unit rotational speed. It is ideal that the scale factor is constant, so the turn signal is in rotation. It varies linearly with speed. An off loop configuration scale factor increases linearity and stability. The biggest cause of error in gyroscopes is the unstable mean wavelength.

Angle random walk (ARW) is a critical noise source of a fiber optic gyroscope and it determines gyro performance. The low noise and high-performance gyroscopes require low ARW and the light source has a high bandwidth is preferred for the low noise gyroscope [40]. Detectable minimum rotation is proportional to thescale factor (SF) of a gyroscope. The SF of the IFOG as a critical parameter of ARW is related with the input rotation rate and phase shift. ARW which is the sum of several noise sources, is given below as shown in Equation [41].

$$ARW = \frac{\sqrt{2}\lambda c}{2\pi \mathrm{LD}} \sqrt{\frac{4k_bT}{R\eta^2P^2} + \frac{\mathrm{e}i_d}{L\eta^2P^2} + \frac{\mathrm{e}}{\eta P} + \frac{\lambda^2}{4c\Delta\lambda}} \qquad 2.18$$

where λ, c, L, D are the central wavelength, the speed of light in a vacuum, fiber optic coil length and diameter of fiber optic coil, respectively. The k_b is the Boltzmann's constant, T is the temperature, R is the resistance of the transimpedance amplifier, η is the photodiode efficiency, P is the optical power at photodiode, e is the electron charge, i_d is the dark current of detector, and Δλ is the bandwidth of the light source.

The photon shot noise due to the quantum nature of light, is the standard deviation of the rate of arrival of photons to the photodetector [42]. Semiconductor PIN photodiodes are the primary choice as a detector for IFOGs thanks to their high quantum efficiency [1]. A detector that has a high quantum efficiency choice is important for low shot noise [43].

Interferometric fiber optic gyroscopes typically use a solid-state laser (semiconductor laser) as a light source to generate light at wavelengths in the near infrared range between 0.83 μm and 1.55 μm. This type of light source emits broadband light, the broadband spectral components of which interact with one another within the fiber optic path and produce a type of noise known as relative intensity noise. Relative intensity noise is a limiting factor in the noise performance of fiber optic gyroscopes. Several approaches have been used in the prior art to reduce the effects of relative intensity noise. These include noise subtraction in the open loop configuration, a closed loop system using bias modulation feedback and a closed loop system using light source pumping current feedback. Noise subtraction in the open loop configuration is limited in practice because it uses a reference channel that is believed to have perfect gain stability. A closed loop system using bias modulation feedback serves to reduce relative intensity noise, but worsens the gyro bias stability and the gyro scale factor linearity. A closed loop system using light source pumping current feedback is limited in terms of bandwidth and does not suppress any higher-frequency components of the relative intensity noise. These higher frequency components significantly contribute to output randomness and corresponding degradation in the performance of the fiber optic circuit. The resulting signal-to-noise ratio establishes a noise floor based on the contribution of the relative intensity noise, that limits the effectiveness of a servo system or control loop such as closed loop system using light source pumping current feedback that uses the phase modulation of the light source pumping current.

The Kerr effect describes that the electric fields of the counter-propagating beams can cause changes in the index of refraction. This occurs by the fluctuation of the optical power level of light source and may result in a phase shift between CW and CCW beams due to the fact that the two signals may not have the same optical power [44]. This effect can be minimized with using a broadband light source, improving MIOC technology and using a square-wave modulation technique, reduced power for fiber and using hollow core fiber [45,46]. It has been proven that the Kerr effect and backscatter phase errors can be reduced by using a broadband light source [47]. As for other errors, there are points that need to be addressed and worked through.

The bias error can simply be defined as the measurement error of the gyroscope [48,49]. In theory regarding the case of IFOG with no-rotation, there is no phase difference between counterpropagating waves. In practice, some error mechanisms can cause phase shift between the reciprocal signals. When the bias is stable, measurements can be calibrated and eliminated. However, most error mechanisms are often not stable and they are sensitive to environmental changes.

The bias mechanisms in the IFOG can be both optical and electronic. Shupe effect, Faraday effect, Kerr effect, MIOC modulation errors, backscattering errors, polarization errors, relative intensity noise are the main error mechanism. These error mechanisms and solution methods in the literature have been examined, and some improvements are studied within the scope of this thesis.

The IFOG has defined several reciprocity requirements such as polarization. The polarizer is used to ensure polarization reciprocity. The polarizer allow only one polarization is to be maintained for the sensor, while the other polarization is eliminated to minimize nonreciprocal light. For the high performance IFOG, a polarizer with higher PER is required for the suppression of a polarization non-reciprocity (PNR) error. This PER requirement is a limitation for both the PM- IFOG [50,51] and the depolarized IFOG [52–55]. As a conclusion, the polarization errors can be minimized using high birefringence PM fiber, minimizing splice misalignments and using maximized PER of the MIOC [56].

1.5. Environmental Factors

Environmental factors can affect the phase drift between the counterpropagating light, thereby introducing a bias or error. Environmental factors such as temperature, vibration and magnetic fields. These factors are both time-varying and unevenly distributed throughout the coil and they induce variations in the optical light path that each counterpropagating wave encounters as it travels through the coil. The phase shifts induced upon the two waves are not equal, causing an undesirable phase shift which is indistinguishable from the rotation rate induced signal.

1.5.1. Thermal Shupe Effect

It is well-known that temperature-related changes in the fiber optic coil affect system performance and this effect is known as the ‘Shupe effect’ in the literature [57] . In the design of IFOG with the fiber optic coil, it is important to correlate the Shupe effect- induced bias error with the symmetry of the fiber optic coil. This relation is simply expressed as;

$$\theta_E = \frac{n_c}{4NA}\left(\frac{dn_c}{dT} + \alpha n_c\right)\int_0^L (2s - L)(T(t,s) - T(0,s))ds \qquad 2.19$$

where t is time, n_c is the nominal refractive index of the fiber core , N is the total number of turns, A is the average area of the turns, L is the total length of fiber, $\frac{dn_c}{dT}$ is the temperature coefficient of n_c , α is the longitudinal expansion coefficient of the fiber, s is the length of d_s segment of the fiber and T (t,s) is the temperature of fiber segment 's' at the time t. As seen here, the bias error depends on the variation of the refractive index of the light. For this reason, this is the geometric effect of temperature changes on the coil. Bias errors due to the temperature change in a small region can be expressed as

$$d\theta_E(t,s) = \frac{n_c L}{4NA}\left(\frac{dn_c}{dT} + \alpha n_c\right)\left(\frac{2s}{L} - 1\right)[T(t,s) - T(0,s)]\, ds \qquad 2.20$$

where $\frac{L}{4NA}$ factor is related with the geometry of the coil. If the mean radius of the floors < r >, the radial spacing d between the floors, the number of turns in each floor is $\frac{N}{M}$, then $\frac{L}{4NA}$ is expressed as,

$$\frac{L}{4NA} = \frac{2\pi\left(\frac{N}{M}\right)\sum_{i=-M/2}^{i=M/2}(<r> + di)}{4\pi\left(\frac{N}{M}\right)\sum_{i=-M/2}^{i=M/2}(<r> + di)^2} \approx \frac{1}{2<r>\left[1 + \frac{M^2 d^2}{12 <r>^2}\right]} \qquad 2.21$$

Temperature-dependent change in the length of fiber segment s is expressed as,

$$dx(t,s) = \left(\frac{dn_c}{dT} + \alpha n_c\right)[T(t,s) - T(0,s)]ds \qquad 2.22$$

If M is greater than 2, the convergence is quite good. Equation (2) using Equations (3) and (4) is expressed as,

$$d\theta_E(t,s) \approx n_c \frac{dx(t,s)}{2<r>}\left(\frac{2s}{L} - 1\right) \qquad 2.23$$

When the length dx is added to the optical length segment s, the optical midpoint of the fiber is shifted. Shupe bias error with midpoint shift is provided by,

$$d\theta_E(t,s) \approx n_c \left|\frac{2s}{L} - 1\right| \frac{dx_m(t,s)}{<r>} = n_c \left|\frac{2s}{L} - 1\right| d\varphi_m \qquad 2.24$$

Then total Shupe bias error is expressed as;

$$\theta_E(t) \approx \frac{n_c}{<r>} \int_0^L \left|\frac{2s}{L} - 1\right| \, dx_m \, (t, s) \qquad 2.25$$

And the total displacement of fiber midpoint is expressed as;

$$\Delta x_m \, (t) = \int_0^L dx_m \, (t, s) \qquad 2.26$$

For a sufficiently uniform distributed temperature change, the Shupe error is the mean is expressed as,

$$\theta_E(t) \approx n_c \frac{\Delta x_m \, (t)}{2 < r >} \qquad 2.27$$

where nc/2 is approximately 1 here, the total Shupe error is associated with the rotation of the fiber's midpoint around the winding axis.

One of the effects of temperature on the IFOG performance is the elasto-optic effect [58]. According to the study by Mohr et al., published in 2004, the time dependent temperature distribution difference in the coil causes the stress distribution change as well as the Shupe effect. This error, known as the elasto-optic effect, causes the bias error Ω(t). Elasto-optic effect is expressed as,

$$\Omega(t) = \frac{n}{2}\frac{L}{R}\int_0^1 \{A.\dot{\varepsilon}_z(z,t) - B.\dot{\varepsilon}_r(z,t)\}\left(1 - \frac{2z}{L}\right) d\frac{z}{L} \qquad 2.28$$

where n is refractive index of fiber, it is seen that the time dependent rotation error depends on the radial and longitudinal strains. Here, $\dot{\varepsilon}_z(z,t)$ is the radial direction, $\dot{\varepsilon}_r(z,t)$ is the longitudinal direction, the time dependence difference of the stresses at the point z. The A and B coefficients represent Pockels coefficient and refractive index of the fiber.

1.5.2. Faraday Effect

Magnetic field-induced bias error is defined as the Faraday effect, and the most common source of this bias error is polarization nonreciprocity errors. Polarization nonreciprocity errors, unlike other fixed error sources, change over time and, therefore, are very difficult to eliminate by system calibration.

The fiber optic coil made of special fibers, PM, are used to reduce non-polarization errors [59]. These fibers have protection zones against external stress, and since the linear polarity in these fibers will not be affected by Faraday phase drift, it reduced the magnetic field dependence [60]. In theory, the refractive index difference between the fast and slow axes of PM fiber through the fiber optic coil remains constant. However, in practice, a pressure applied to the fiber forming the fiber optic coil will make a difference in the refractive index between the fast and slow axes. The refractive index difference changes the beat-length, which directly affects the birefringence. Since the magnetic field-induced phase shift is also related to these values, the fiber behavior in the fiber optic coil directly affects the Faraday-induced phase difference.

The Faraday phase error is on the order of 1 to 10 μrad per 1 G (1 mT). In Hotate and Tabe's studies, it is shown that the use of PM fiber did not completely absorb the Faraday phase shift because the birefringent axes in the fiber could not be adjusted precisely [61]. When the principal axis of a linear birefringent of PM fiber is rotated, the eigen polarization modes cannot remain in a precise linear polarity [60]. This axis rotation is called fiber twist. Because of this buckling, a circular birefringence effect $\Delta\beta c$ is added to the linear birefringence and birefringence is expressed as $t + \Delta\beta c$. Here, the $\Delta\beta c$ effect is minimal beside the $\Delta\beta$ effect.

Due to the Magnetooptic Faraday effect, a longitudinal magnetic field B causes a shift in the phase of circularly polarized light by an amount determined by the Verdet coefficient V of the medium. This phase shift depends on the relative direction of the magnetic field and light propagation vectors. Phase shift for a linearly polarized light, depending on the variable in magnetic field orientation as shown in the following Equation

$$\Phi F = V.B.L \tag{2.29}$$

where V is Verdet constant of which unit is rad/T·m, B is the magnetic field and L is the fiber length.

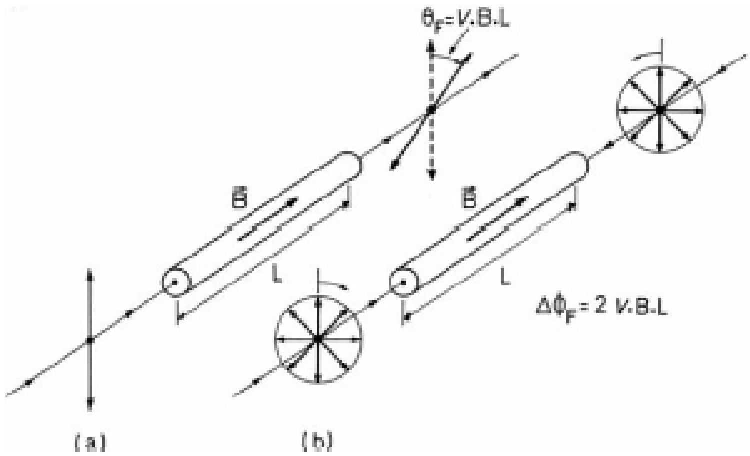

Figure 2.7. Faraday effect of a piece of fiber: (a) rotation of linear polarity and (b) phase difference between two opposing circular polarities

The Faraday phase shift can also be expressed as,

$$d\Phi F = \alpha p\ (z)\ V \cdot B \cdot dz. \tag{2.30}$$

Here, αp (z) is a coefficient depending on the polarization state. This value is equal to zero when there is linear polarity and ± 1 in circular polarity according to polarity orientation [60].

The magnetic field on the fiber optic coil will analyze the Faraday effect responsible for in-plane (along the x and y axes) magnetic sensitivity as described by Hotate and Tabe [61]. The second will focus on the effect that causes transverse magnetic sensitivity (along the magnetic z-axis) as explained by Logozinski [62]. The placement of the fiber optic coil in a coordinate plane is as shown in the figure, and the z-axis has been chosen as the vertical axis direction for the fiber optic coil, with the unit length s along the fiber.

The Faraday effect is a magneto-optic phenomenon that returns a linear polarization as circular birefringence and induces a phase shift in a circular polarization. Circular birefringence is proportional to the longitudinal component B of the magnetic field.

The use of PM fiber in fiber optic gyroscopes makes the polarization elliptical as a result of the linear birefringence of the PM fiber and axial bending of the fiber although the polarization in the fiber optic coil is linear, which makes the system susceptible to the Faraday effect [61].

Uniform bending gives uniform sensitivity, but the effect is integrated across the fiber optic coil and the overall sensitivity to the external magnetic field is zero due to Ampere's law. Magnetic Field B is alternatively in the direction of propagation and in the opposite direction and, therefore, compensates for the total effect.

A coil of radius R, a Verdet constant V, a fiber birefringence stroke length Λ, a length of fiber L, a scale factor SF, a twist rate (S) along curvilinear abscesses, and an in-plane magnetic field S can be described by the formula:

$$S = \frac{SF}{2\pi^2} V\Lambda \int_0^L t_w(s) \cos\left(\frac{S}{R}\right) \cos(\theta) ds \qquad [\circ/h/G] \tag{2.31}$$

J. Noda et al. measured the Verdet constant at different wavelengths of the commonly used Panda fiber and showed that this value is ~0.60 rad/T/m at 1550 nm wavelength [63]. Kumar et al., in their study, showed that a fiber optic coil with a lower beat-length are less sensitive to magnetic field in a study using fibers from different PM fiber manufacturers such as Corning, Fujikura, Nufern, and Fiber Core [64].

If the polarization state inside the fiber optic coil is stable, the external magnetic field does not create any fluctuation in the Sagnac phase difference. However, the low birefringence in single-mode fiber and the twist of fiber can cause a change in the Sagnac phase difference of the external magnetic field. A Faraday effect under external magnetic field is expressed as [65]

$$B = VHL \tag{2.32}$$

here, V is the Verdet Constant, L is the length of exposure or the length of the fiber under the magnetic field, and H is the magnetic field strength. With the use of PM Fiber in the Fiber optic coil, there is no change in the polarization axis due to the Faraday effect due to the high birefringence effect. The bias error due to the Faraday Effect has opposite polarity in the fast and slow axes [66]. Electric and Magnetic field vectors are expressed with the Jones Matrix. It is also convenient to use the Jones Matrix Method to calculate the bias error in gyroscopes [67]. The derivations of the bias error due to the Faraday Effect is detailed in Chapter 4.

$$\delta = \frac{8B_0 r}{\Delta\beta} \cdot \sqrt{2m\pi W} \tag{2.33}$$

$$\Delta\beta = \frac{2\pi}{L_b} \tag{2.34}$$

In the “Progress in Navigation-Grade IFOG Performance” study, they are reduced by using μ-metal magnetic shielding [28]. Carpenter HyMu "80"® and Carpenter High Permeability "49"® are used as the magnetic shielding material developed for fiber optic coil [32].

1.5.3. Vibration

Vibration can cause intensity fluctuation through components in the optical light path in an IFOG and it also causes phase fluctuation through physical rotation movement of the fiber optic coil. In practice, vibration, shock or both of them should be considered when the potential drift sources are concerned. The stress change of fiber optic coil, the optical device pigtail movement and the structural resonance would increase dynamic error under the vibration. It is difficult to mathematically simulate the vibration effects because each fiber optic coil manufacture is quite different from each other. Vibration-induced bias can be reduced by the careful selection of adhesive material of fiber optic coil because of its modulus of elasticity.

The vibration sensitivity of a sensor coil results from processes within the coil that introduce a non-reciprocal phase error into the output, which cannot be distinguished from the rate signal. The bias vibration sensitivity is caused by a non-reciprocal phase shift in the light propagating in opposite directions, which in turn results from the changes in the fiber length and the refractive index, which are caused by vibrational expansion via the photoelastic effect. It is known that vibration-induced bias errors can be reduced by using an adhesive potting material with a Young's modulus is increased. It is known that the adhesive have 1,000 to 20,000 psi (~7 to ~13.8 Mpa) Young's modulus are sufficient to meet both the bias vibration requirement and the low thermal stress [68].

3 CHARACTERIZATION OF THE FIBER OPTIC GYROSCOPE

The IFOG configuration that characterized and optimized in this chapter, includes a light source unit, an optical detection unit, a fiber optic coil and an MIOC (Figure 3.1). In this chapter each part of the IFOG configuration has been studied including the effect of the environmental factors and an IFOG has been built by combining the best configuration of these three parts and the proposed combination minimizes the measurement errors of the IFOG under temperature variation.

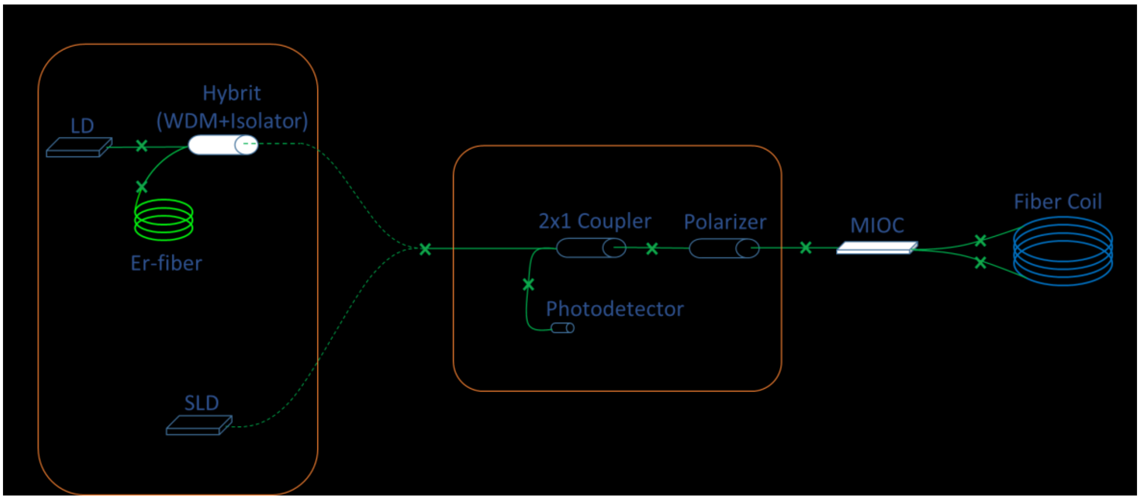

Figure 3.1. IFOG Configuration characterized in Chapter 3.

3.1. Light Source

It is clearly described in Chapter 1.3.1 that low noise, high stability, and a wide spectral band light source are preferred in high performance IFOG systems. The commonly preferred light sources for fiber optic gyroscopes are a fiber-based ASE light source and an SLD, and these sources are characterized as low noise, high stability, and wide spectral bandwidth sources. This section includes the simulation and the characterization of the SLD and the fiber-based ASE light source that have been described in detail in Section 1.3.

3.1.1. Light Source Simulation

In this section, ASE Light Source and SLD simulations are studied. VPIcomponentMaker™ developed by VPI Systems is a premium simulation software that enables the analysis, evaluation and design of optical components, systems, and networks. VPI Photonics provide the precise simulation of fiber optic based optical components, Er/Yb/Tm doped amplifiers and light sources, continuous wave and pulsed fiber optic sources, optical signal processing for telecommunications, high power, and ultra-fast applications.

Fixed and dynamic Er/Yb/Tm/encoded fiber and waveguide models offer the opportunity to simulate signal amplification, noise generation, and higher-order limiting effects in core or cladding pumped configurations at single or multiple wavelengths. The required properties and parameters of each component can be adjusted in the simulation program. In addition, data obtained in the laboratory environment can be used for most of the modules, so that the components whose data are available can be simulated in the most realistic way. By editing the simulation properties, the resolution methods and resolutions of the created simulations can be adjusted. The split-step method is generally used as the solution method. In addition, different analysis and optimization methods such as sweep, tuning and transient can be performed in the simulations.

In the simulation program, different signal representations are allowed to make strong use of the duality between the calculations in the time and frequency domain and to apply the most efficient model in each case. In an amplified system, the bandwidth of the modulated carriers may be much narrower than the bandwidth of ASE (amplified self-emission) noise propagating throughout the system. However, it is important to simulate the entire noise bandwidth, as it will lead to electrical noise after photodetection.

ASE noise covers more than a 5 THz bandwidth, and if we define it as an SFB (Single Frequency Band) signal, a sampling rate of 5 THz would be required, giving 5,000 samples per ns or in real time. This would be inefficient if the system's signal bandwidth is less than 5 THz. For this reason, a more complex approach is given with the definition of Noise Bins (NB) by separating noise and optical data signals in the spectrum and describing noise with a special form of parameterized signal representation.

Noise Bins assumes that the noise spectral density is constant over a data block (set by the TimeWindow global parameter). Therefore, the noise can be represented with the average spectral density (in two polarizations). NB adapts to the bandwidth to provide a coarse but efficient spectral resolution and at the white noise limit, a single noise box can represent the entire noise spectrum. In this way, analyzes can be made by reducing the number of samples and the simulation time is reduced.

VPI Photonics simulations are based on the Split-Step method where the fiber is split into segments or segments in optical system simulations [69]. For each segment, dispersion and nonlinearity in time domain effects are included separately. The dispersion is treated as a frequency-dependent phase shift in the frequency domain and non-linearity in the time domain as a momentary power-dependent phase shift. The stride length can be adapted to give the maximum phase shift per stride. The Split-Step method, which is used in the simulations carried out in this thesis, provides a solution for aperiodic or periodic boundary conditions.

The schematic of the simulated ASE Light Source is seen in Figure 3.2. In the simulation scheme, forward and backward ASE Light Source configurations are built with 980 nm 200mW Laser Diode, 980/1550 WDM and a filter, and Er-doped fiber. Since the backward configuration has high power gain, it has continued to work with the backward direction as shown in Figure 3.2.

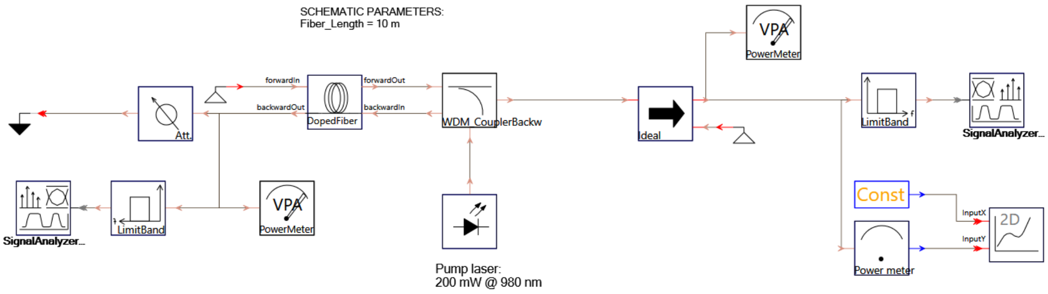

Figure 3.2. Schematic diagram of Er-doped ASE light source with VPI-photonics

The properties of each optical component are investigated and the optical parameters of the components used in the IFOG are specified and set into the blocks for the simulation model to be compatible with the measurement set-up. The specifications of the erbium doped fiber, which is one of the most important parts of the model, are determined according to the Er-fiber used in the measurement setup. The parameters of the erbium doped fiber used in the ASE light source model are given in the table below (Table 3.1).

Table 3.1. Er-doped fiber specifications

Properties	Unit	Value
Peak absorption at 1530 nm	[dB/m]	30
MFD at 1550 nm	[10^-6 m]	5.9
core NA		0,25
Erbium concentration	[ions/m^3]	1,28E+25
Core diameter	[10^-6 m]	6,3
Overlap Factor		0.92 0.91 0.9

The power gain of the ASE Source due to the Er-fiber length increase is performed at the start of the analysis. In the simulation, the forward ASE configuration is preferred due to the low power response of backward configuration. ASE output power versus the length of Er-doped fiber is calculated (Figure 3.3).

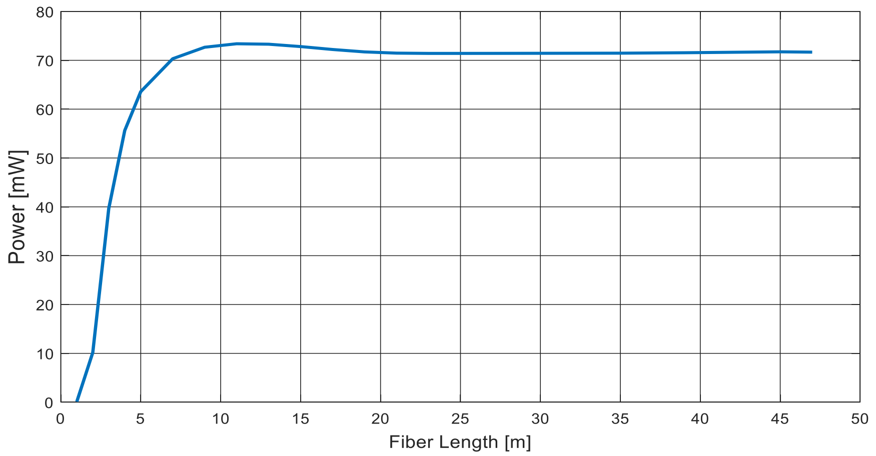

Figure 3.3. ASE output power versus Er-doped fiber length of the light source

When the Er-fiber length increases, the optical power of ASE light source increases up to 10m Er-fiber length, and then the optical power becomes stable as shown in Figure 3.3.

Since the atoms excited in the far parts of the fiber do not have enough energy to reach the output, the output power does not increase even if the fiber length increases after a certain value. The output power increases linearly with the increase of Erbium doped fiber length up to 9.7 m, and there is no change in the output power after this length.

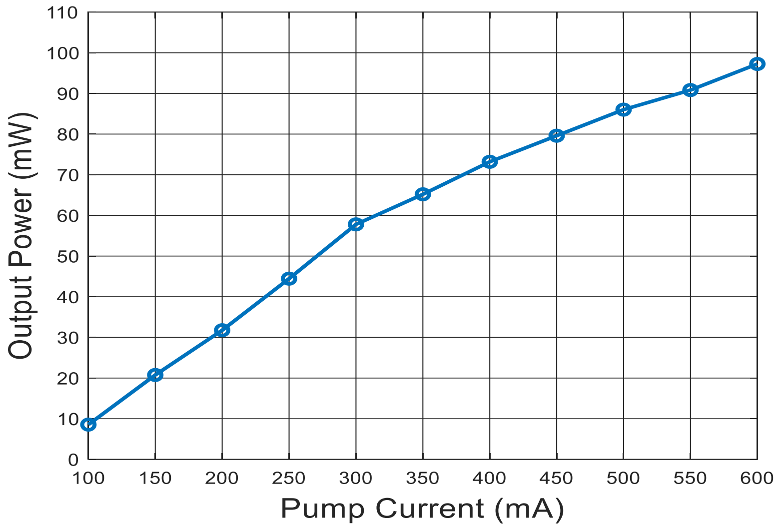

Figure 3.4. ASE output power versus the laser diode pump current

The ASE output power increases linearly while the laser diode pump current increases as shown in Figure 3.4. The optical spectrum of the ASE Source with the 10m length Er-fiber length is given in Figure 3.5.

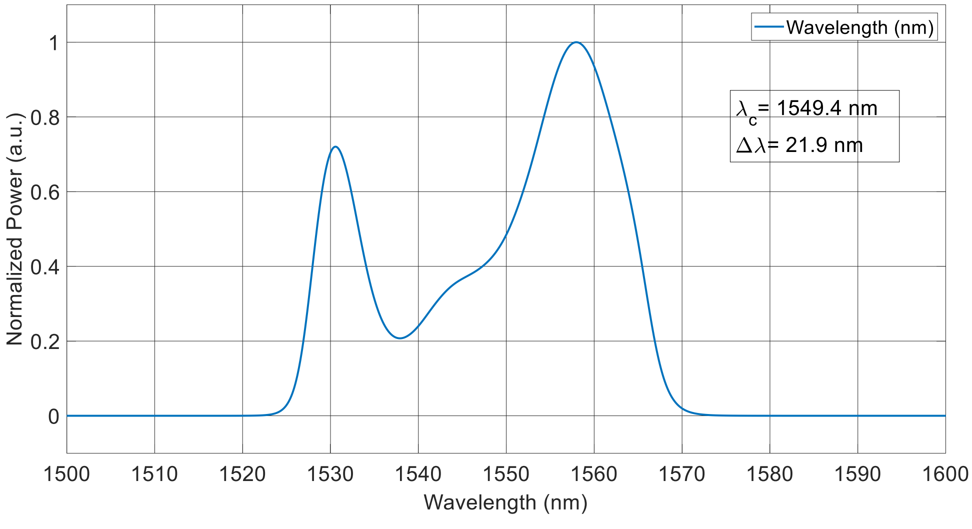

Figure 3.5. Optical spectrum of ASE light source with VPI-photonics

SLD light sources have a spectral profile close to the Gaussian shape and produce low fluctuation, high power, and broadband light centered at a 1550 nm wavelength. An onboard thermistor allows the temperature control and thereby the optical power and optical spectrum are stabilized. The VPI-photonics light source model schematic of the SLD is given in Figure 3.6.

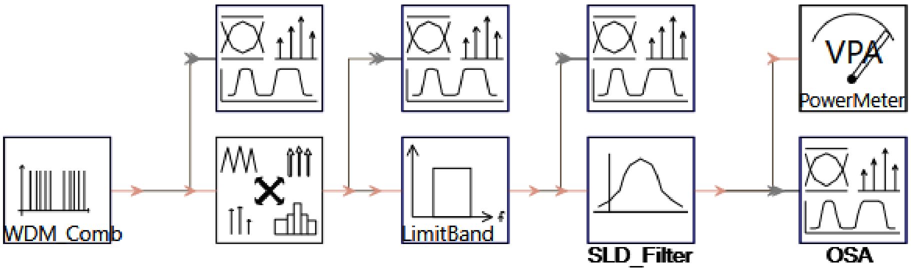

Figure 3.6. Schematic diagram of SLD with VPI-photonics

In the model, an optical signal with flat optical spectrum and wide bandwidth is build first. Then, these signals are passed through an optical filter in the form of the spectrum of the light source, and the SLD light source is simulated. The signals are first created from PS (Parameterized Signal) type and then converted to SB (Sampled Band) type with the SignalConverter block.

The optical spectrum of the simulated SLD is given in Figure 3.7.

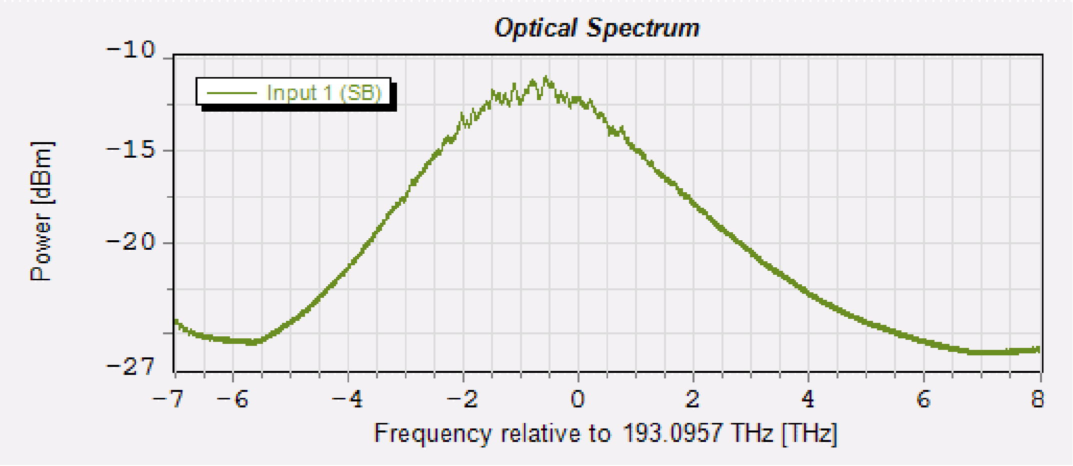

Figure 3.7. Optical spectrum of SLD with VPI-photonics

When the optical spectrum of SLD given in Figure 3.6 is compared to the optical spectrum of ASE as shown in Figure 3.4, it can be concluded that the SLD has the broad bandwidth than Er-doped fiber based ASE light source. The IFOG construction is started by forming the installation and detailed analysis of the Er-doped fiber based ASE light source as the primary optical unit.

3.1.2. Er-doped Fiber Based ASE Light Source

A semiconductor fiber-coupled pump diode that has a 976 nm center wavelength with a 1-2 nm bandwidth is used. Er-doped fiber is chosen as a gain fiber to create an ASE signal for the range of 1550 nm wavelength. WDM with a 980/1550 nm is used to separate the ASE signal and the pump signal and WDM is also a pump to the gain fiber.

A 980 nm or 1480 nm centered wavelength semiconductor pump diode, corresponding to the absorption wavelength of the Er-ions needs to be used to pump the Erbium-doped fiber light source. The pump diode laser must have a wide operating temperature range in terms of optical power to allow sufficient optical power to be obtained for the optical path, wavelength stability to remain within the pumping band of the Er-doped fiber and electrical power consumption. As a result of the examinations, although 1480 nm pump diodes, can be another possibility considering the more up-to-date technology, high amount of power, low cost and ease of supply, it is decided to use 980 nm center wavelength diodes for the ASE light source.

The core of the gain fiber is doped with Erbium ions and is typically pumped with 980 or 1480 nm which are the most efficient wavelength for absorption and produce gain around 1550 nm (C-Band) or 1590 nm (L-Band). Photons in the radiation band (1500 - 1600 nm) that occur with spontaneous emission are amplified by the stimulated emission medium. This phenomenon is called amplified spontaneous emission (ASE). Due to the spectroscopic nature of erbium, (Er-ions have a 3-4 level systems), the radiation center wavelength can shift (typically in the range of 1530 -1560 nm) according to the change of the inversion level along the fiber. The erbium-doped fiber length must be a sufficient length to absorb most of the pumping light coming from the diode laser and, therefore, maximum efficiency can be used for the IFOG systems.

WDM is a compact optical component that is used to transmit the pump light (980 nm) to Erbium-doped fiber (1530 - 1560 nm) and receive the optical signal with 1530 - 1560 nm wavelength formed in Er-dopped fiber either output of Er-dopped fiber or in signal port. According to output port, the ASE is called forward ASE (output from Er-dopped fiber) or backward ASE (output from signal port). In this thesis, we always use backward ASE due to higher efficiency and no residual pump. WDM provides ASE output by combining the signals of two fibers carrying two different wavelengths into a single fiber. In addition to WDM guiding for different wavelengths, there is also a need for an isolator, which is a unidirectional optical gateway that transmits the light unidirectionally. Therefore, the back-reflection signal from the transmitted signal will be blocked and protected from the unwanted modulation for the ASE source.

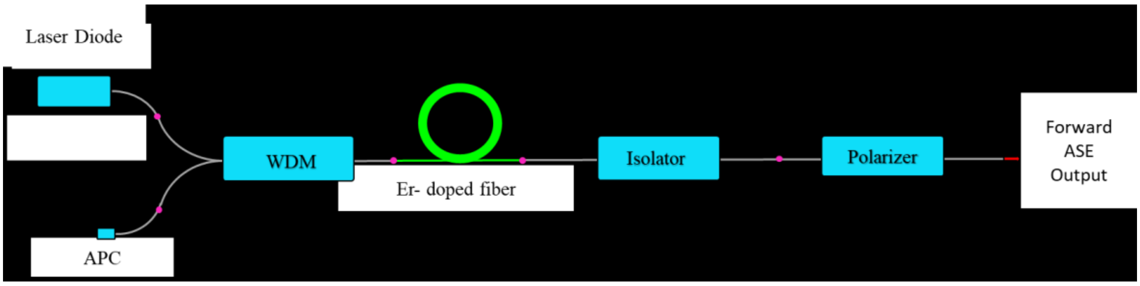

Figure 3.8. ASE configuration in the forward direction

The ASE light source performance is verified with the measurements. In order to carry out the measurements, two different ASE light source configurations are constructed. The installed forward and the backward direction ASE light source configuration are shown in Figure 3.8 and Figure 3.9, respectively.

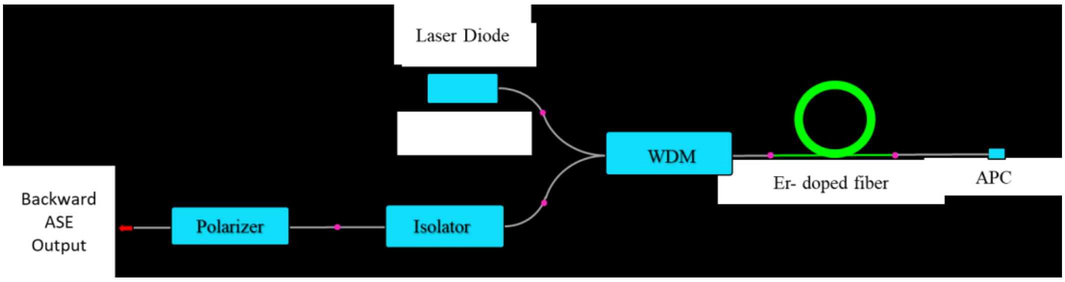

Figure 3.9. ASE configuration in the backward direction

First, we start to measure the forward and backward ASE output performance in terms of the ASE output power and the ASE light source spectrum. The optical configurations have the same optical components. The optical output powers are measured for both configurations for different pump power levels at room temperature, as shown in Figure 3.10. As can be seen in Figure 3.10, for the pump power range of 124–182 mW, the optical power efficiency is much higher in the backward configuration than forward configuration.

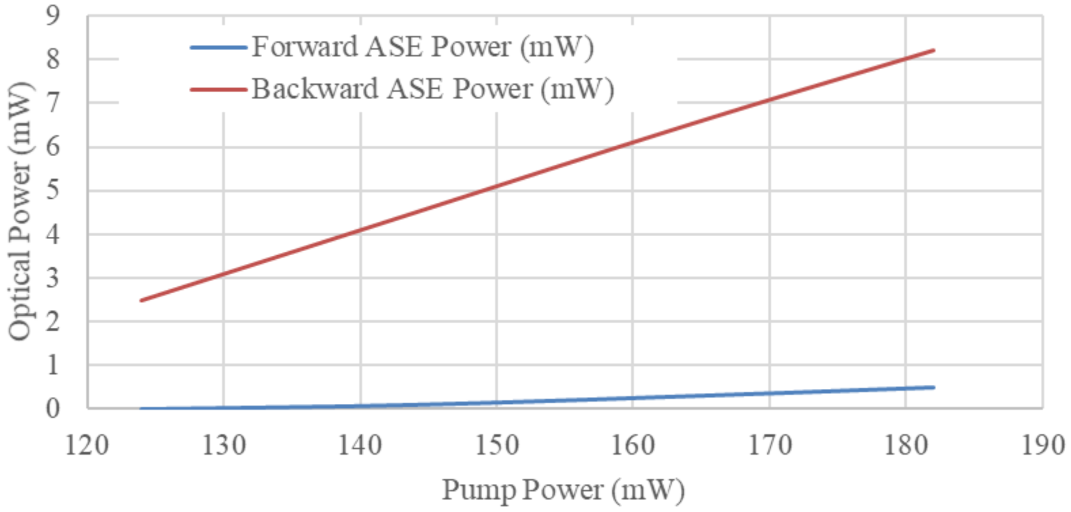

Figure 3.10. Optical power versus the pump power for forward and backward ASE (for approx. 1.6 m Er-added fiber length)

Figure 3.11 shows the optical spectrum at different pump currents in the backward and forward configuration. The curves roughly show a ladder shape as the central wavelength has jumps with the increase of pump power. The output spectrum of an Er-doped ASE light source in backward configuration shows a shape with two peaks: near 1530 nm and 1550 nm. The 1560 nm peak plays a dominant role at low pump power and the 1530 nm peak plays a dominant role at high pump power. As can also be seen in Figure 3.11, the central wavelength (nm) increases while the pump power increase in both configurations.

It can be clearly seen among the optical spectrum measurement of both the backward and forward direction that the backward direction ASE power is more efficient in increasing pump power.

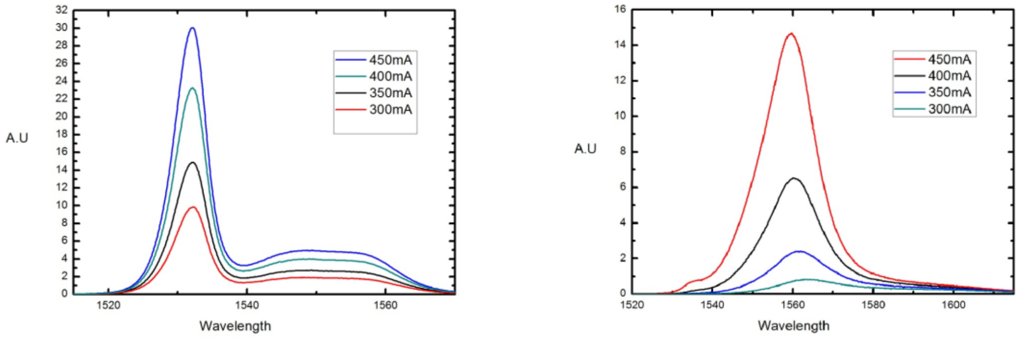

(a) (b)

Figure 3.11. Optical spectrum according to the pump diode current in (a) the backward and (b) forward direction

As a result of this measurement, the ASE light source, which is constructed within the scope of this thesis, has been studied with the backward direction configuration since the power gain is high. A Laser Diode is a 976 nm centered wavelength semiconductor, an Er-doped fiber is used for gain medium, and a hybrid component that includes both a WDM and an isolator guides the 1550 nm output signal for the backward direction configuration of the ASE light source as shown in Figure 3.12.

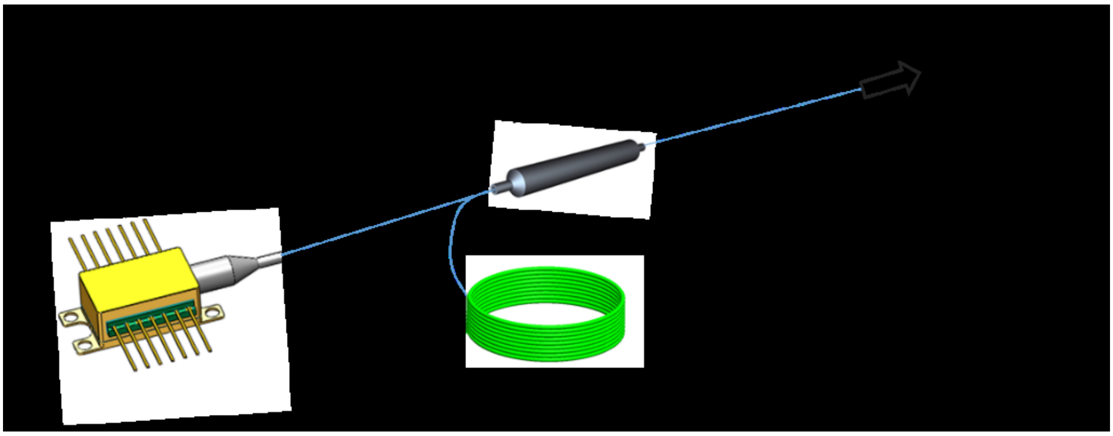

Figure 3.12. Schematic diagram of the Er-doped ASE light source

For the temperature and laser controller, the Thorlabs ITC4005 model is used to feed the laser diode at a predetermined temperature and driving current. Light source ASE power is measured by power-meter, and the spectral measurements is examined with an optical spectrum analyzer (OSA).

Figure 3.13. Picture of optical spectrum analyzer (OSA) used for optical spectrum measurements

The mean wavelength of the light source is calculated according to the following Equation 3.1

$$\lambda_{\text{mean}} = \frac{\int \lambda \cdot p(\lambda) \cdot d\lambda}{\int p(\lambda) \cdot d\lambda} \qquad 3.1$$

where λ is the wavelength and p(λ) is the optical power depending on each wavelength. The spectral width of the light source is calculated according to the Equation below (Equation 3.2) .

$$SW = \int p(\lambda) \cdot d\lambda \qquad 3.2$$

Various configurations of the light source studies is carried out to increase the wavelength stability of the ASE light source. In order to increase the spectral width and wavelength stability of the optical spectrum, different fiber lengths and fiber termination methods have been studied for Er-doped Fiber used in ASE light source design.

Initially, the light source configuration studies are carried out for different lengths of Er-doped fiber. Figure 3.14 shows the light source assembled on a table. (the laser diode is not shown in the figure).

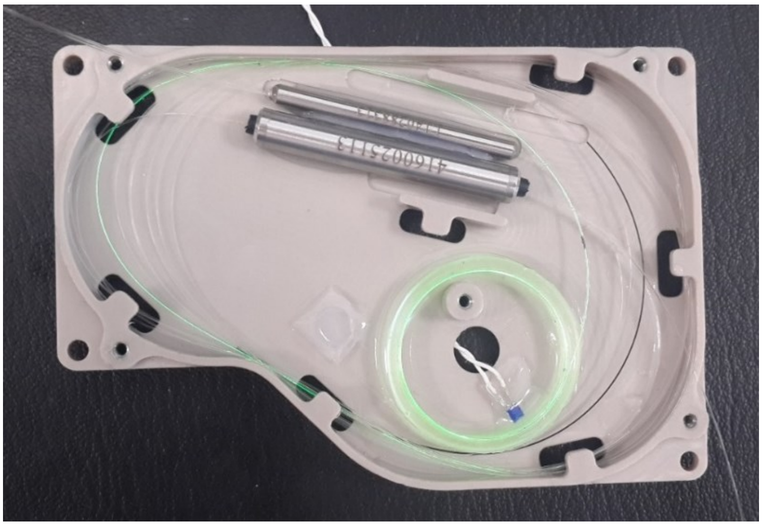

Figure 3.14. ASE light source with Er-doped fiber assembled on the table

The light source spectrum characterization studies are started by making an optical spectrum measurement at room temperature of the ASE light source installed with 6m long Er-doped fiber. As a result of the power measurements, it is determined that the use of a minimum of 6 m Er-doped fiber is appropriate. The optimum length is determined according to the number of Er-doped fiber doping concentricity.

According to the optical spectrum obtained for the light source driven with 400 mA current, the center wavelength (λc) and spectral width (Δλ) values are calculated as 1541 nm and 15.4 nm, respectively. LD is driven with 400mA drive current that is sufficient to provide minimum power consumption.

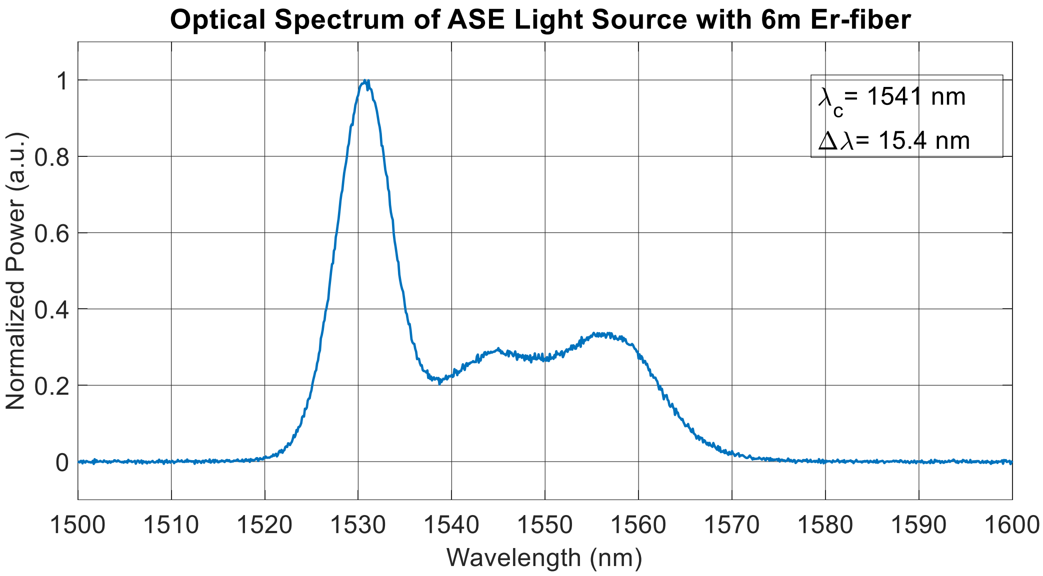

Figure 3.15. Optical spectrum of an ASE light source with 6m Er-fiber

Different operating temperatures in the range of −40 °C to 85 °C are performed in climatic chamber and the schematic view of the measurement set-up is given in Figure 3.16. Center wavelength changes, RMS of wavelength linewidth and optical power measurements are performed for the all-fiber Er-doped ASE and SLD source. All of these results that included wavelength and optical power characterization in this study is taken by OSA. This was done to ensure that the power measurement by OSA is confirmed by using an optical power detector.

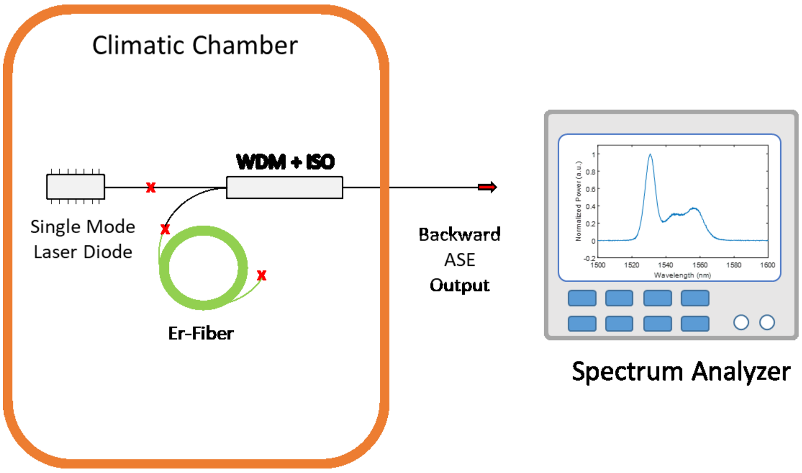

Figure 3.16. Temperature characterization setup of Er-doped ASE source

The wavelength analysis of this light source is measured in the temperature range of - 40 °C to +85 °C, and the mean wavelength shift depending on the temperature variation is calculated as 4.51 ppm/°C (Figure 3.17). The temperature dependent wavelength stability (1σ) is calculated as 63 ppm over the entire temperature range (Figure 3.18).

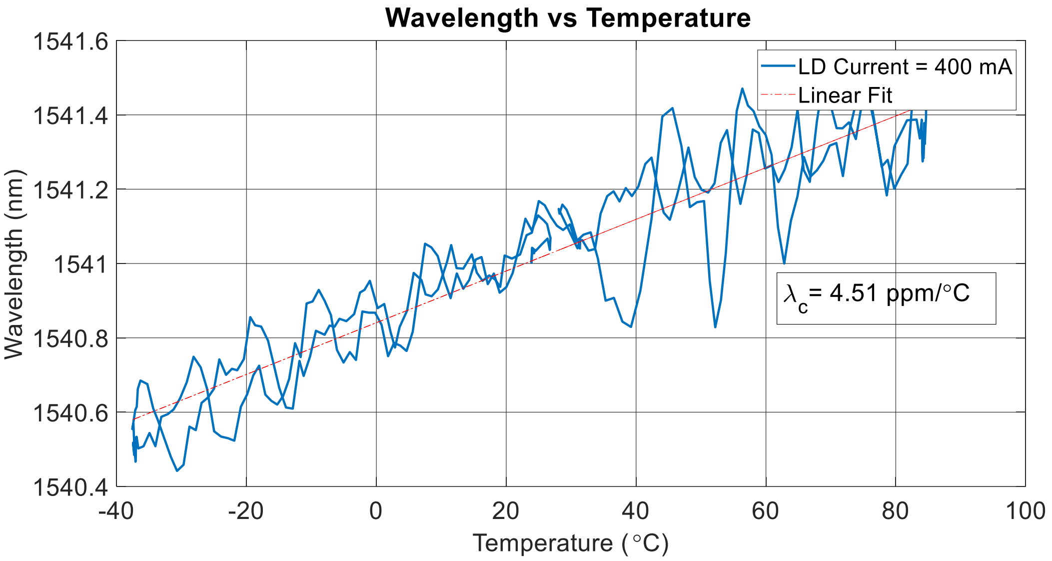

Figure 3.17. The wavelength versus the temperature of the ASE light source with 6m Er-fiber

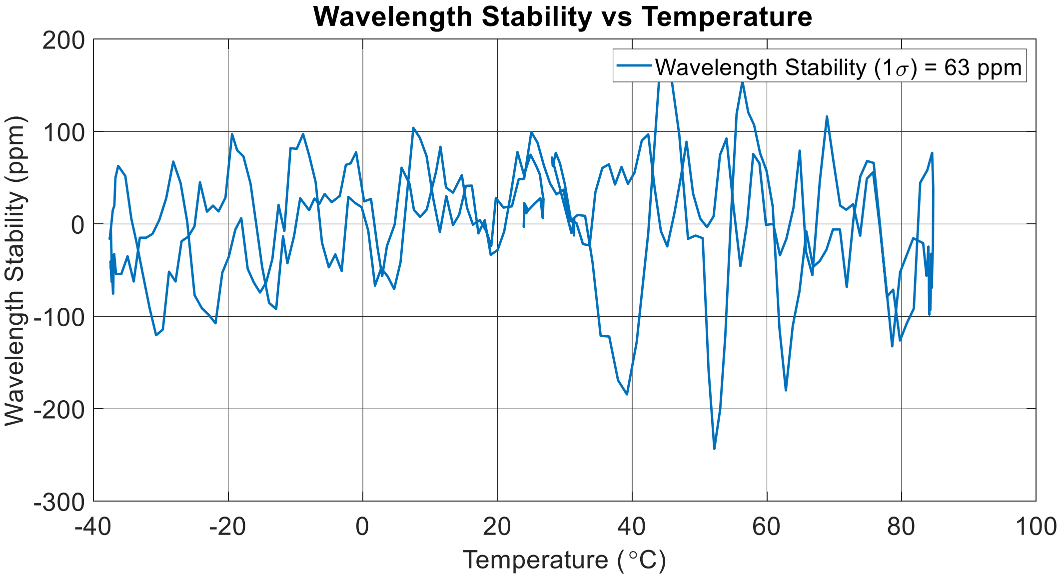

Figure 3.18. The wavelength stability versus the temperature of the ASE light source with 6m Er-fiber

According to the temperature-dependent spectral width measurement, the temperature-dependent spectral width value changes linearly and is calculated as 922 ppm/°C over the entire temperature range. The output optical power of the light source is measured under temperature change and it is calculated that the optical power changed by 13% over the entire temperature range (Figure 3.19).

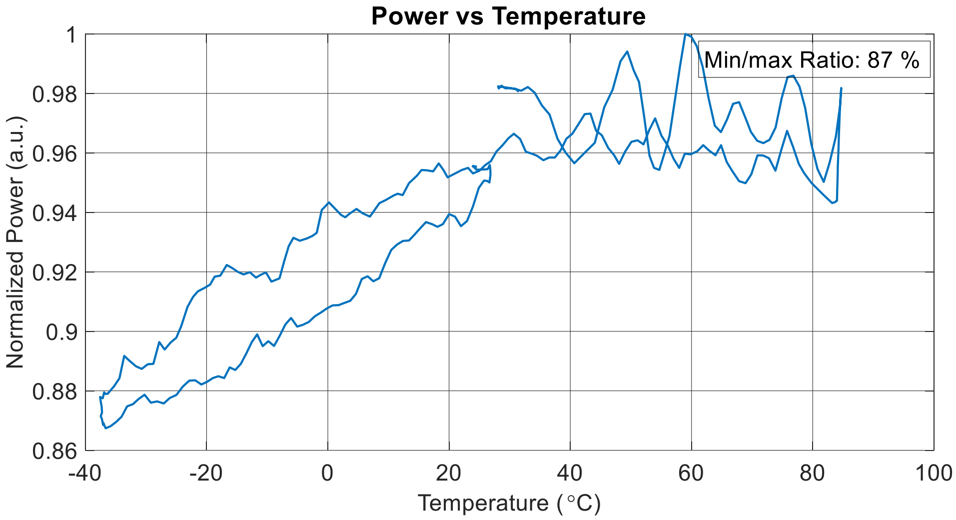

Figure 3.19. The ASE output power versus the temperature of the ASE light source with 6m Er-fiber

Based on the simulation results given in Figure 3.3, the maximum gain is obtained from the Er-fiber by using a 9.6 m long fiber. In order to obtain this analysis experimentally and to make temperature-dependent characterizations with this configuration, a light source is constructed with 10 m long Er-fiber and analyzed.

According to the optical spectrum obtained for the light source driven with 400 mA current, the center wavelength (λc) and spectral width (Δλ) are calculated as 1543.7 nm and 18.8 nm, respectively. According to the first spectrum measurement result of the source at room temperature, a broader spectral width is obtained from ASE light source with 10 m Er-fiber than the ASE light source with 6 m Er-fiber.

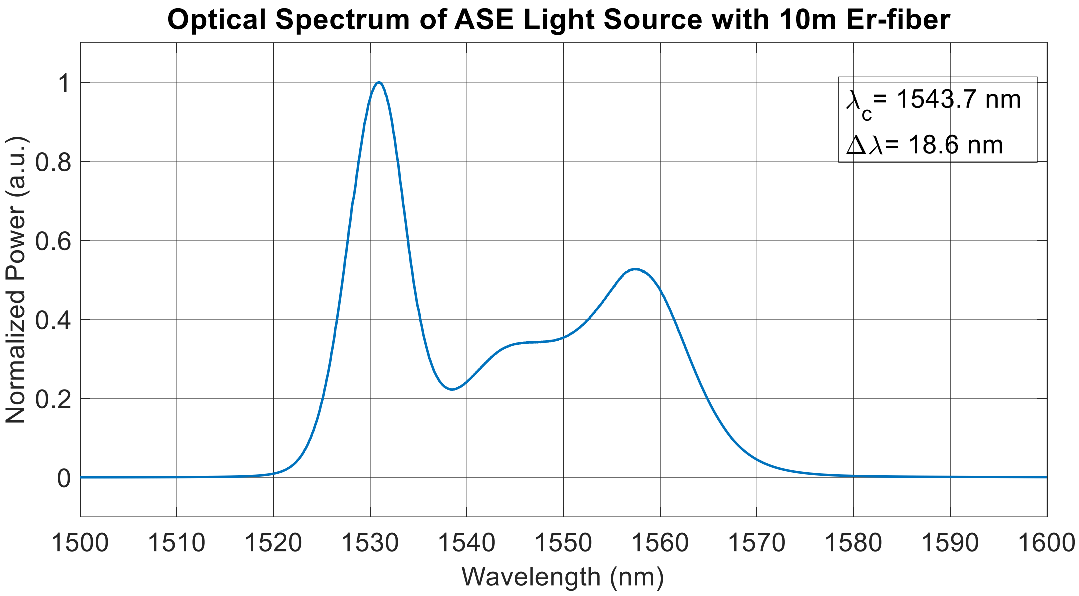

Figure 3.20. Optical spectrum of the ASE light source with 10m Er-fiber

Wavelength characterization of this light source is made in the temperature range of -40 °C to +85 °C, and the wavelength variation depending on the temperature is calculated as 3.24 ppm/°C. The temperature dependent wavelength stability (1 σ) is calculated as 41 ppm over the entire temperature range.

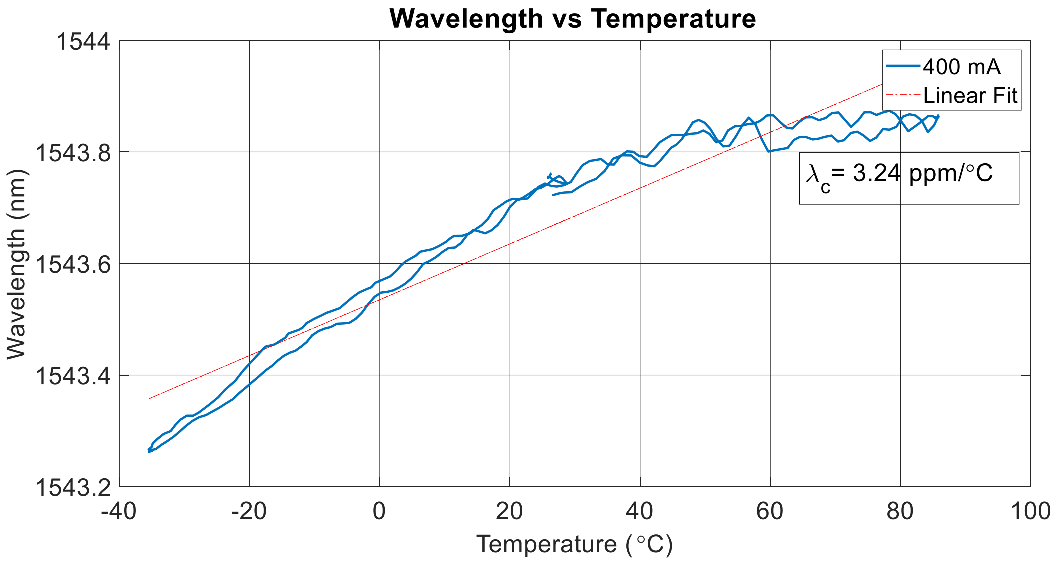

Figure 3.21. Wavelength versus temperature of ASE light source with 10m Er-fiber

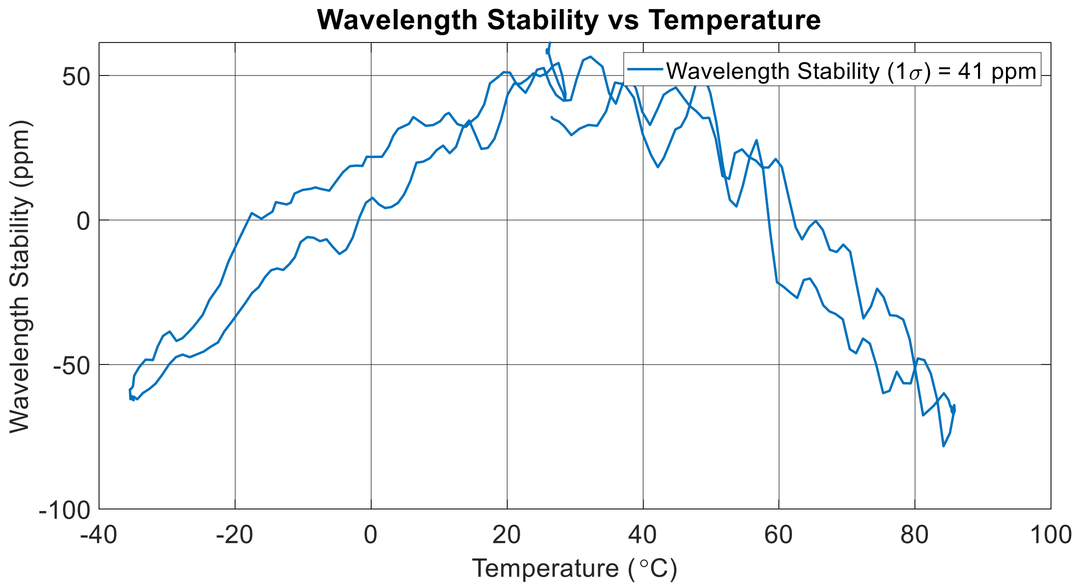

Figure 3.22. The wavelength stability versus the temperature of the ASE light source with 10 m Er-fiber

According to the temperature-dependent spectral width measurement, the temperature-dependent spectral width value changes linearly and is calculated as 823 ppm/°C over the entire temperature range. The output optical power of the light source is measured under temperature and it is calculated that the optical power changed by 9 % over the entire temperature range.

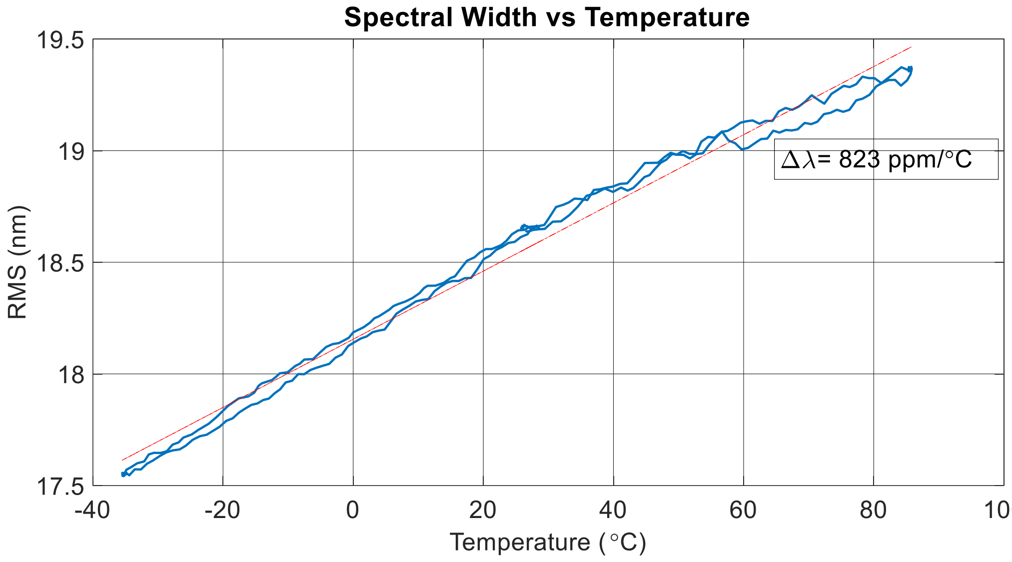

Figure 3.23. Spectral width versus the temperature of the ASE light source with 10m Er-fiber

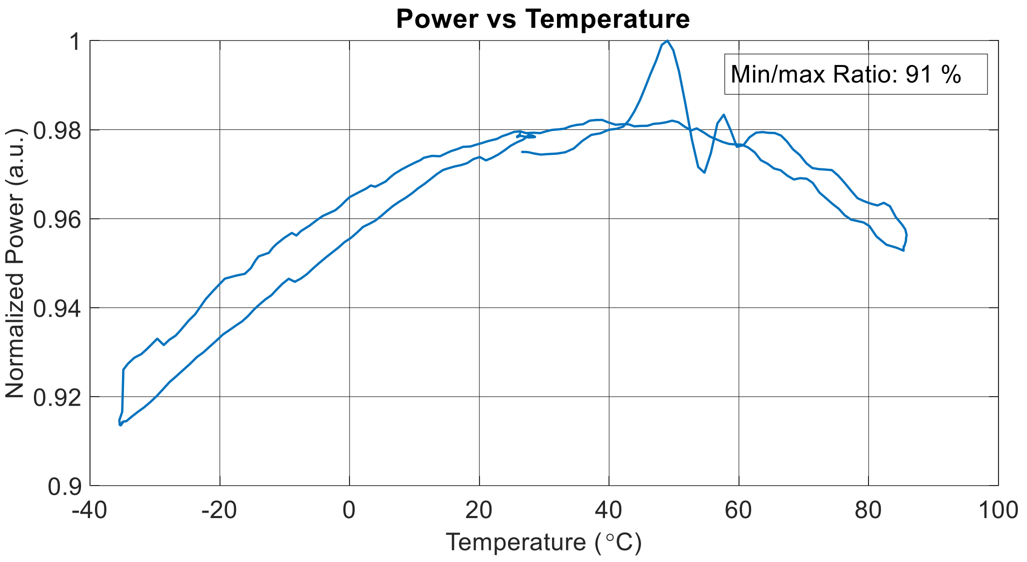

Figure 3.24. The power versus the temperature of the ASE light source with 10 m Er-fiber

All the measurement results of the ASE light source installed with the length of 6 m and 10 m Er-fiber are given in Table 3.2.

Table 3.2. Measurement results of the ASE light sources with 6 m and 10m long Er-fiber

ASE Light Source	Wavelength (nm)	Spectral Width (nm)	Wavelength stabilization (ppm/°C)	Wavelength stabilization (ppm)	Spectral width (ppm/°C)	Optical Power loss (%)
With 6 m Er-fiber	1541	15.4	4.51	63	944	13
With 10 m Er-fiber	1543.7	18.8	3.24	41	823	9

It is clearly seen in Table 3.2 that the ASE light source with 10 m Er-fiber has many advantages such as near 1550 nm spectrum and a broad spectral width at room temperature, more stable wavelength and low power loss under temperature variation advantage compared ASE light source with 6 m long Er-fiber.

Different Er-fiber termination methods have been studied for the light source installed with 10 m long Er-fiber which has good measurement results. To analyze the different termination methods for Er-doped fiber, the wavelength and spectral measurement results are evaluated comparatively by measuring the spectrum at room temperature.

In this section, Er-fiber termination methods have been studied with the light source installed with 10 m long Er-fiber, since the spectral width is optimum for IFOG systems which is characterized in detail in Section 3.1. The basic termination method in the literature is splicing the angle polished connector (APC) to the free end of the Er-fiber. Many termination methods have been studied such as knot the fiber, splice the coreless fiber, add the gain flattening fiber (GFF), and additional Er-fiber.

At a start as a termination method, fiber knot termination and APC splice methods are compared. Optical spectrum measurements of the ASE light source installed with 10 m Er-fiber are made at room temperature for fiber knot and APC termination methods, and the results are given in Figure 3.25.

According to the optical spectrum obtained for the light source driven with 400 mA current, the center wavelength (λc) and spectral width (Δλ) values are calculated as 1552.3 nm and 19 nm, respectively for knot termination. In addition, the center wavelength (λ_c) and spectral width (Δλ) values are calculated as 1552.5 nm and 18.9 nm, respectively for APC termination. As seen in the results, the knot and APC termination are quite similar to each other.

Secondly, as a termination method, fiber knot termination and coreless fiber splice methods are compared. Optical spectrum measurements are made at room temperature for fiber knot and APC termination methods of ASE light source installed with 10 m Er-fiber, and the results are given in the figure.

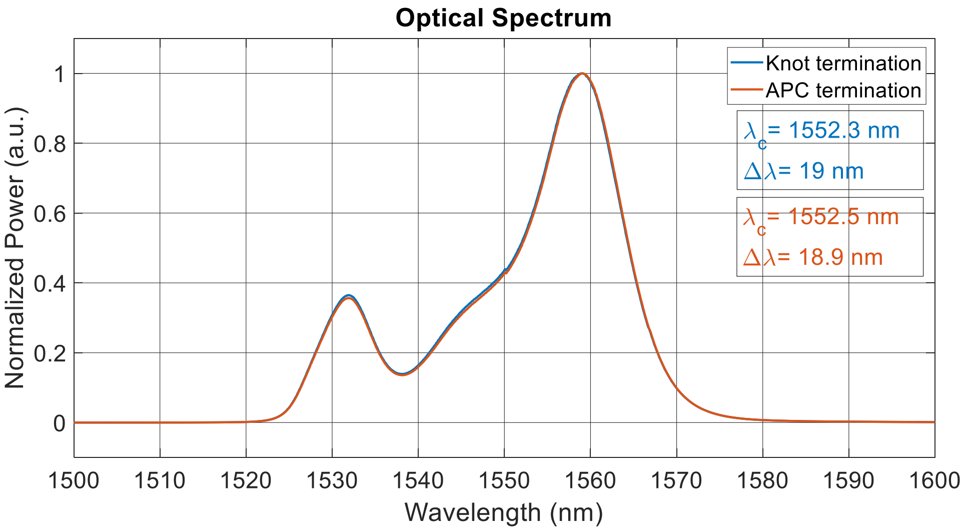

Figure 3.25. Optical spectrum of the 10 m Er-fiber ASE light source comparison of a fiber knot and APC termination methods

According to the optical spectrum obtained for the light source driven with 400 mA current, the center wavelength (λc) and spectral width (Δλ) values are calculated as 1552.3 nm and 19 nm, respectively, for fiber knot termination and the center wavelength (λc) and spectral width (Δλ) values are calculated as 1525.5 nm and 18.9 nm, respectively for APC termination.

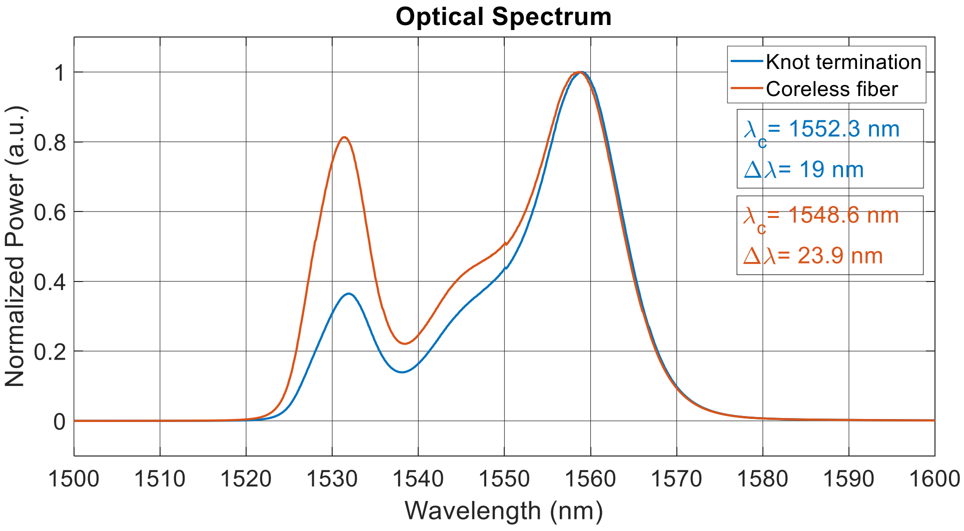

Figure 3.26. Optical spectrum of the 10 m Er-fiber ASE light source comparison of a fiber knot and coreless fiber termination methods

Lastly, as a termination method, coreless fiber splice methods and coreless fiber splice methods with 1m extra fiber are compared. Optical spectrum measurements are made at room temperature for the fiber knot and APC termination methods of ASE light source installed with 10 m Er-fiber, and the results are given in the figure.

Optical spectra are measured at room temperature for the termination methods of adding extra Er-fiber after the coreless fiber of the ASE light source installed with 10 m Er-fiber, and the results are given in Figure 3.27.

According to the optical spectrum obtained for the light source driven with 400 mA current, the center wavelength (λc) and spectral width (Δλ) values are calculated as 1554.7 nm and 16.7 nm, respectively for the termination methods adding an extra 1 m Er-fiber after the coreless fiber.

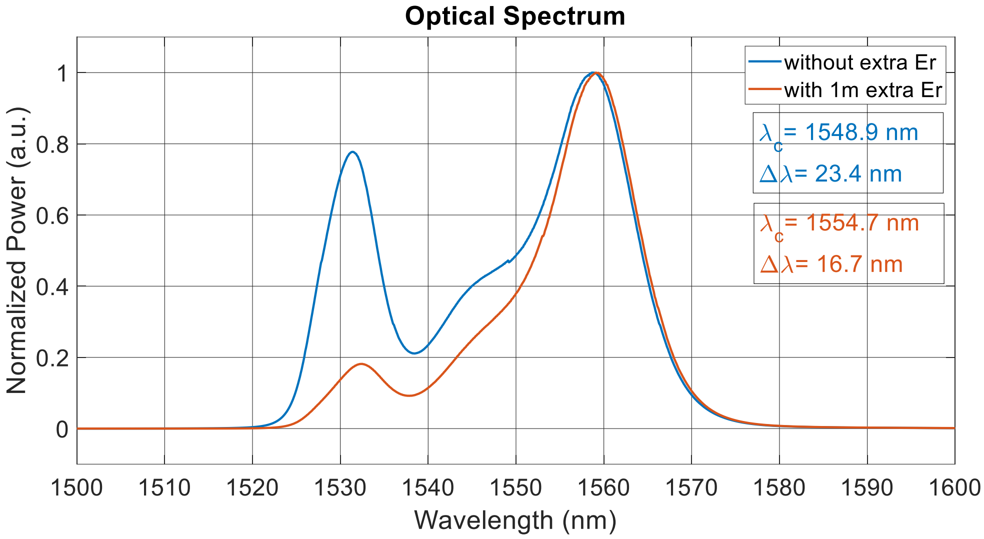

Figure 3.27. Optical spectrum of 10 m Er-fiber ASE light source comparison of an additional 1m extra Er-fiber and without any additives

The wavelength and spectral measurement results have been evaluated according to the various termination methods, and it is preferred to work with coreless fiber termination method for the broad spectral width.

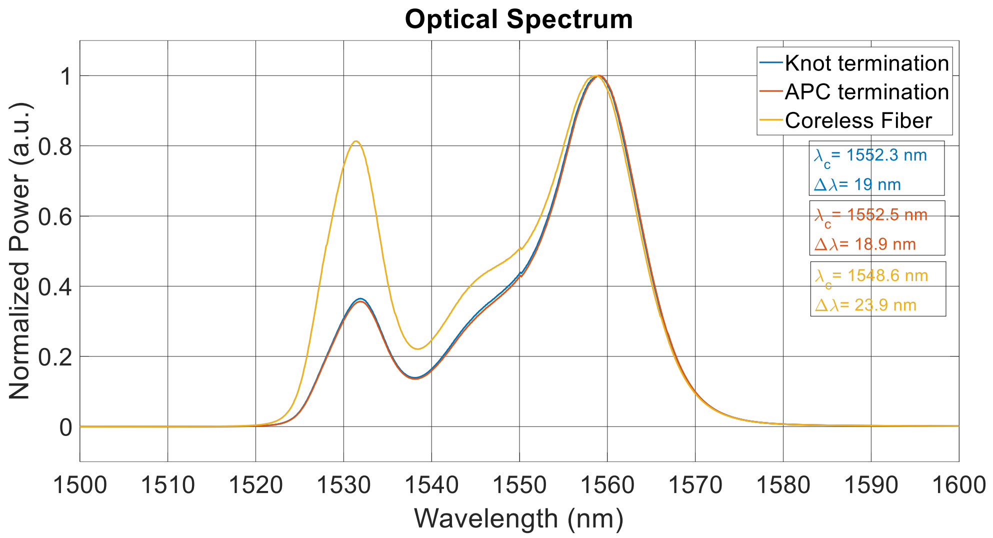

Figure 3.28. Optical spectrum of the 10 m Er-fiber ASE light source comparison of different fiber termination methods

3.1.3. SLD Light Source

According to the optical spectrum obtained for the SLD light source driven with 400 mA current, the center wavelength (λ_c) and spectral width ($\Delta\lambda$) values are calculated as 1559.9 nm and 51.6 nm, respectively.

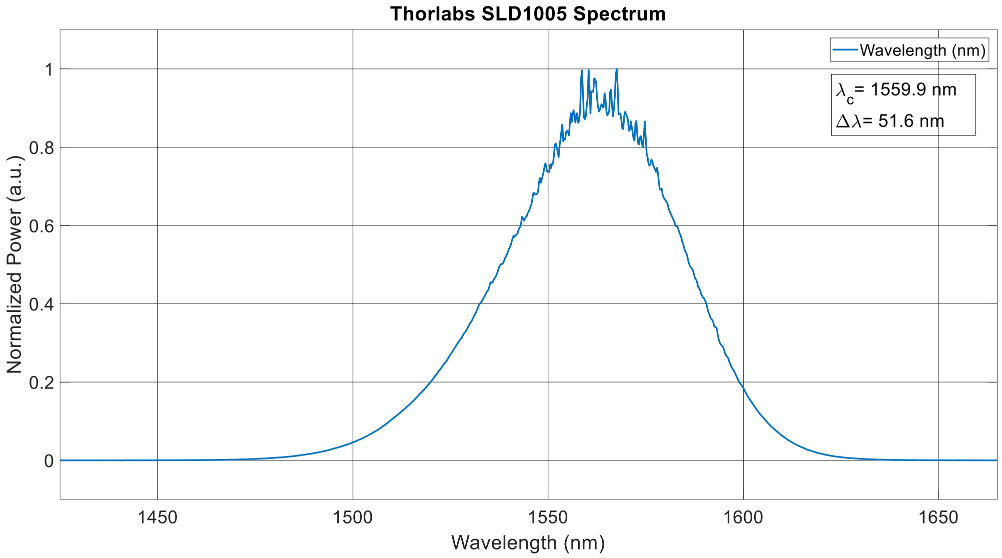

Figure 3.29. Optical spectrum of SLD

Different operating temperatures in the range of −40 °C to 85 °C are performed in a climatic chamber. Center wavelength changes, wavelength linewidth and optical power measurements are performed for both all-fiber Er-doped ASE and SLD source. All of the results including the wavelength and optical power characterization in this paper were taken by OSA in order to be sure that the power measurement by OSA is confirmed by using optical power detector.

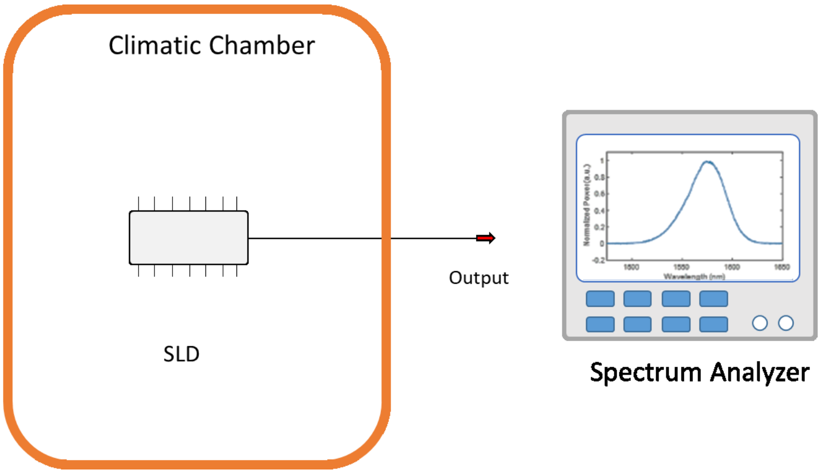

Figure 3.30. Temperature characterization setup of SLD

Wavelength characterization of this light source is made in the temperature range of – 40 °C to +85 °C, and the wavelength variation depending on the temperature is calculated as 3.13 ppm/°C. The temperature dependent wavelength stability (1 σ) is calculated as 42 ppm over the entire temperature range.

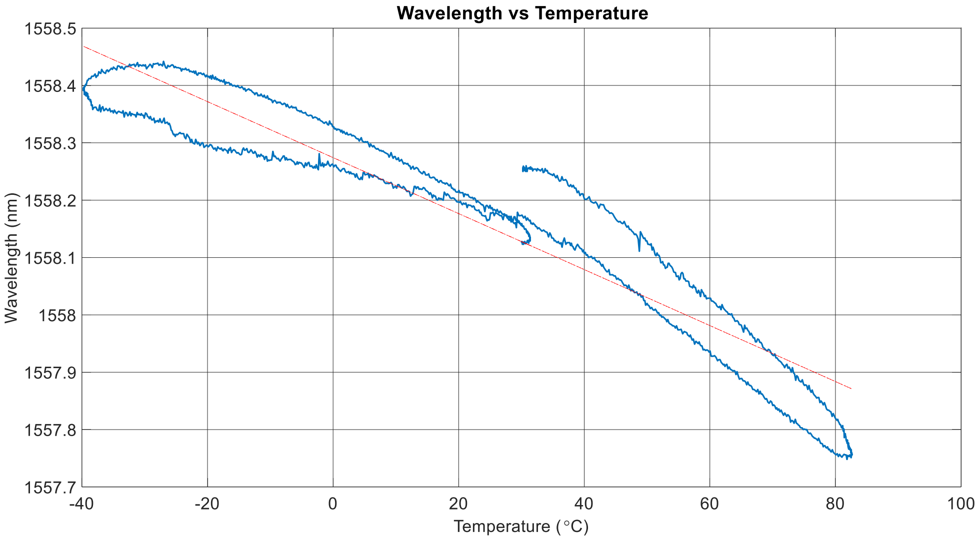

Figure 3.31. Wavelength versus the temperature graph of the SLD light source

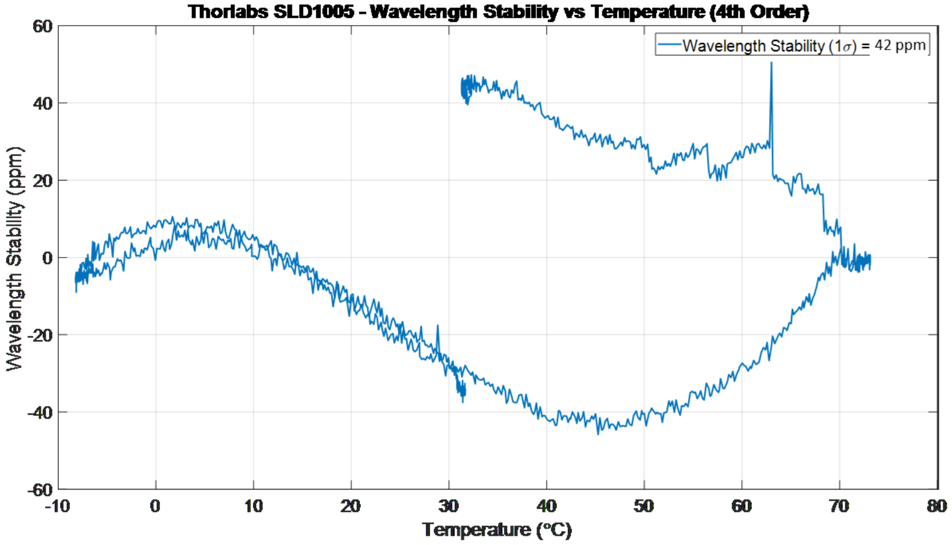

Figure 3.32. The wavelength stability versus the temperature graph of the SLD light source

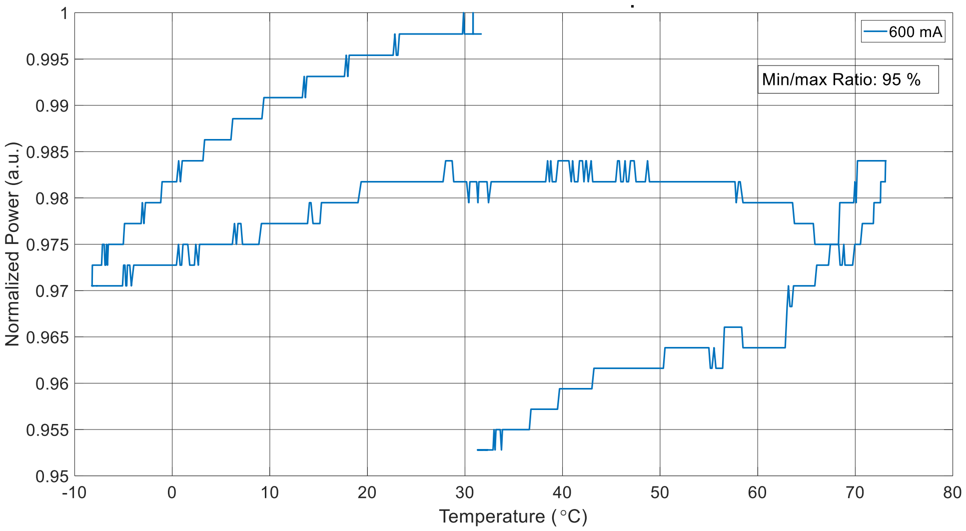

Figure 3.33. The power versus the temperature graph of the SLD light source

All measurement results of the ASE light source installed with 6m and 10 m long Er-fiber, different termination methods and SLD are given in the table shown below.

Table 3.3. Comparison of the ASE light source and SLD specifications

Light Source	Er-doped ASE Light Source			SLD
Er-fiber length	6m	10m	10m	-
Termination Method	Knot	Knot	Coreless fiber	-
Wavelength (nm)	1541	1543.7	1549	1559.9
Spectral Width (nm)	14.5	18.8	23.5	51.6
Temperature Dependence of Wavelength (ppm/°C)	4.51	3.24	1.17	3.13
Wavelength Stability (ppm)	63	41	46	42
Temperature Dependence of Spectral Width (ppm/°C)	944	823	193	555
Optical Power Loss (%)	13	9	7	5

The fiber-based ASE light source configuration is selected as 980 nm pump laser, WDM and a 10m long Er-doped fiber with the coreless fiber termination in the above-mention studies. According to the optical spectrum obtained for the light source driven with 400 mA current, the center wavelength (λc) and spectral width (Δλ) values are calculated as 1549 nm and 23.5 nm, respectively.

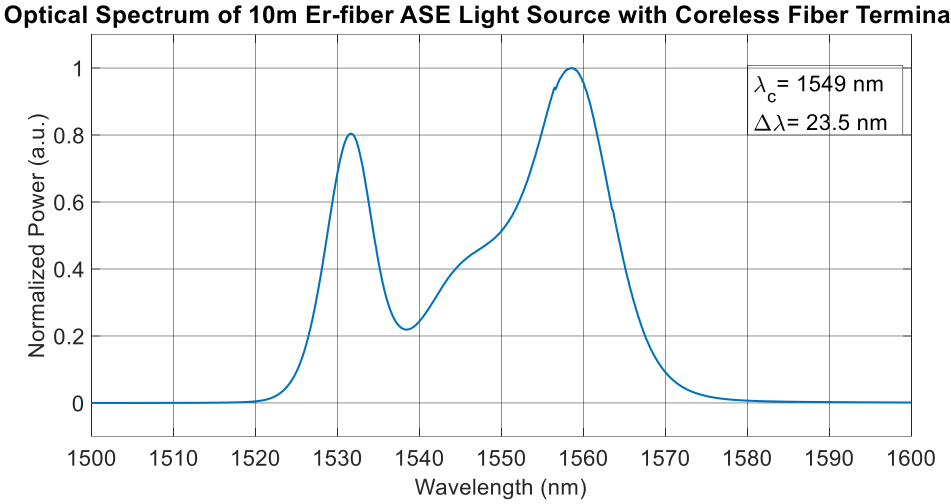

Figure 3.34. Optical spectrum of the 10 m Er-fiber ASE light source with coreless fiber termination

Wavelength characterization of this light source is made in the temperature range of -40 °C to +85 °C, and the wavelength variation depending on the temperature is calculated as 1.17 ppm/°C. The temperature dependent wavelength stability (1 σ) is calculated as 46 ppm over the entire temperature range.

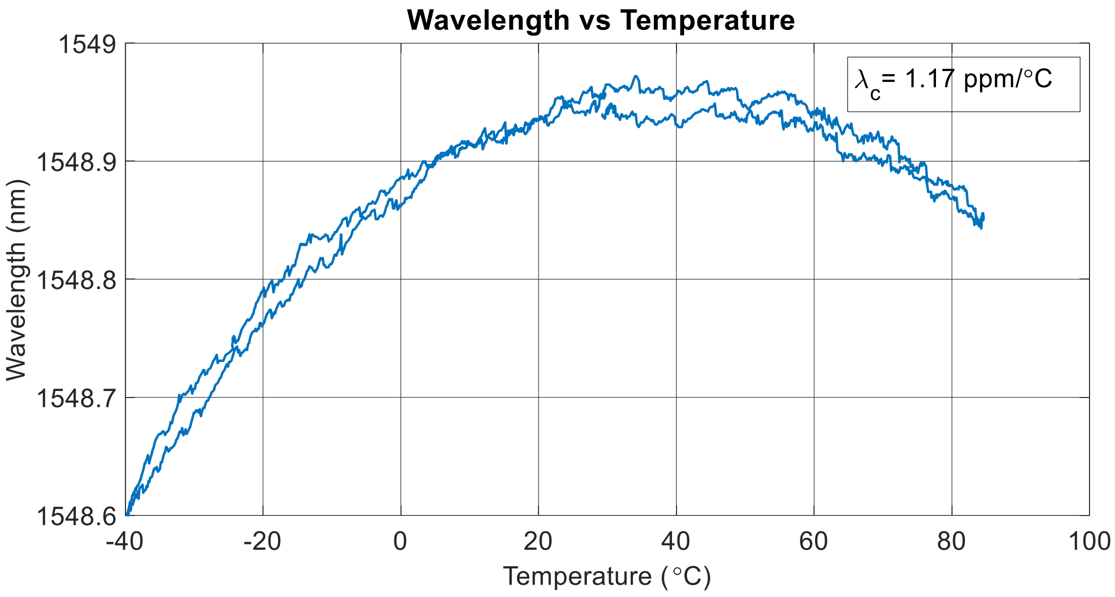

Figure 3.35. Wavelength versus the temperature of the 10 m Er-fiber ASE light source with coreless fiber termination

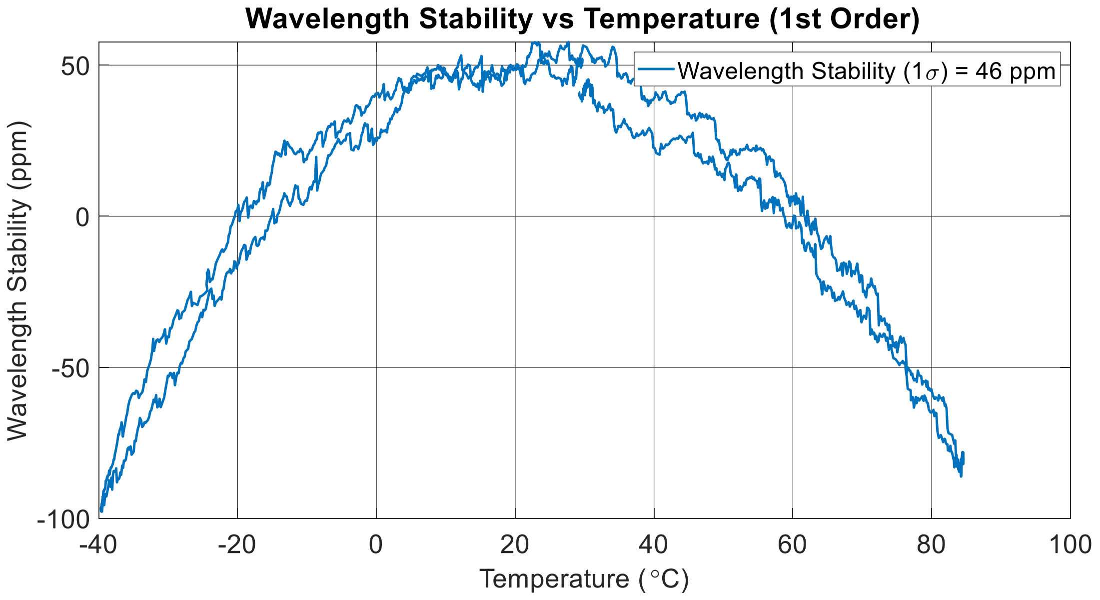

Figure 3.36. The wavelength stability versus the temperature of the 10 m Er-fiber ASE light source with coreless fiber termination

According to the temperature-dependent spectral width measurement, the temperature-dependent spectral width value changes linearly and is calculated as 193 ppm/°C over the entire temperature range. The output optical power of the light source is measured under temperature and it is calculated that the optical power changed by 7% over the entire temperature range.

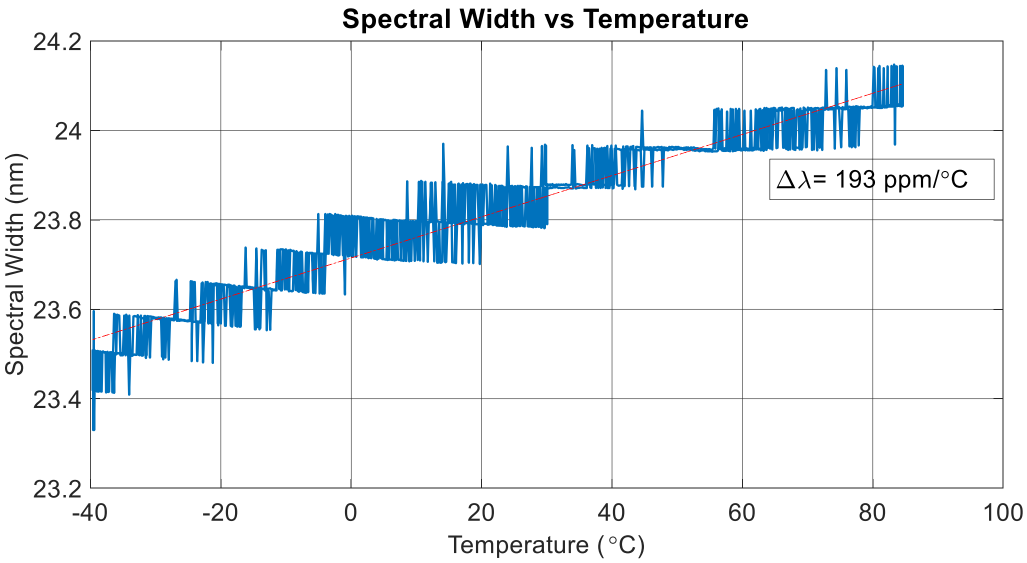

Figure 3.37. Spectral width versus the temperature of 10 m Er-fiber ASE light source with coreless fiber termination

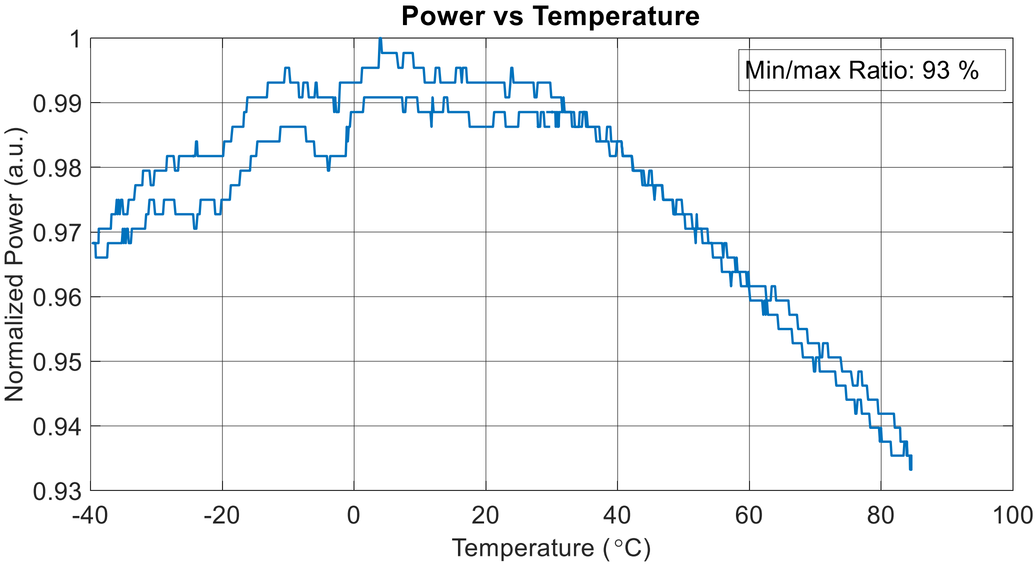

Figure 3.38. Power versus the temperature of the 10 m Er-fiber ASE light source with coreless fiber termination

The power consumption of the light source is measured under temperature and it is calculated that the power consumption of laser diode, temperature controller and the cumulative is calculated over the entire temperature range as 0.61 W, 1.52 W and 2.13 W, respectively. The output optical power of the laser diode is measured under temperature and it is calculated that the pump power changed by 7% over the entire temperature range.

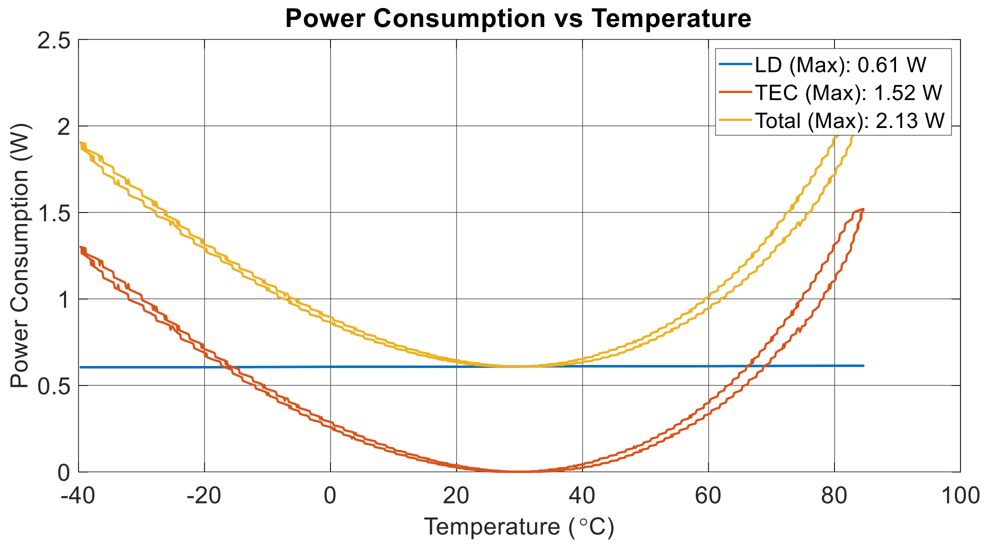

Figure 3.39. Power consumption versus the temperature of the 10 m Er-fiber ASE light source with coreless fiber termination

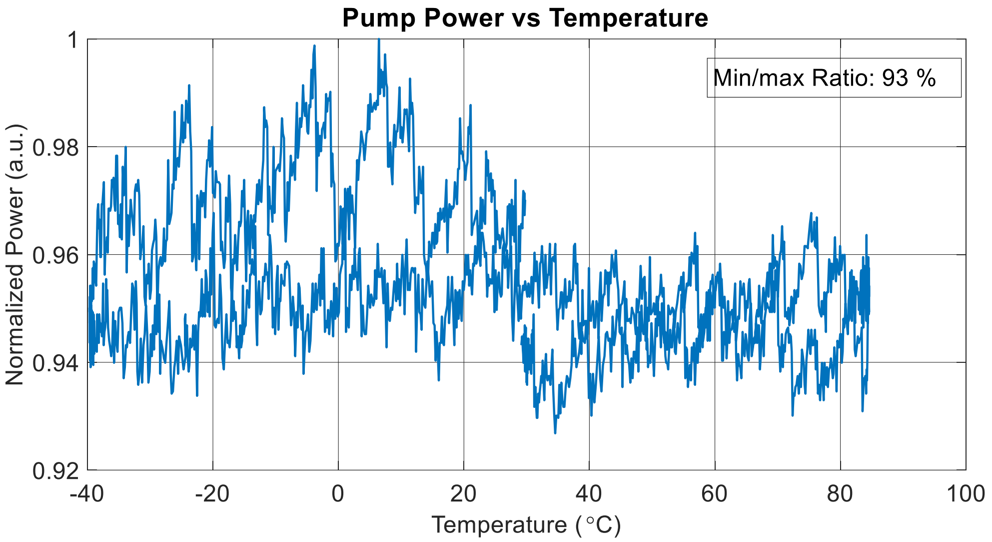

Figure 3.40. 1 LD pump power versus the temperature of the 10 m Er-fiber ASE light source with coreless fiber termination

Measurement results of the 10 m Er-fiber ASE light source with coreless fiber termination is given in Table 3.4.

Table 3.4. Measurement results of the 10 m Er-fiber ASE light source with coreless fiber termination

	Wavelength (nm)	Spectral Width (nm)	Temperature Dependence of Wavelength (ppm/°C)	Wavelength Stability (ppm)	Temperature Dependence of Spectral Width (ppm/°C)	Temperature Dependence of Optical Loss (%)
10m Er-fiber	1549	23.5	1.17	46	193	7

After the optimizations and comparisons of optical measurements, the length of the erbium doped fiber is determined as 10 m and the power of the pump laser is determined as 0.23 W. As a result of the light source characterization, an ASE power is obtained as 68 mW at the output of the light source. When the optical spectrums are examined and it is clearly seen that the experimental results are in good agreement with the simulation results. Center wavelengths and bandwidths are also match well (Figure 3.41).

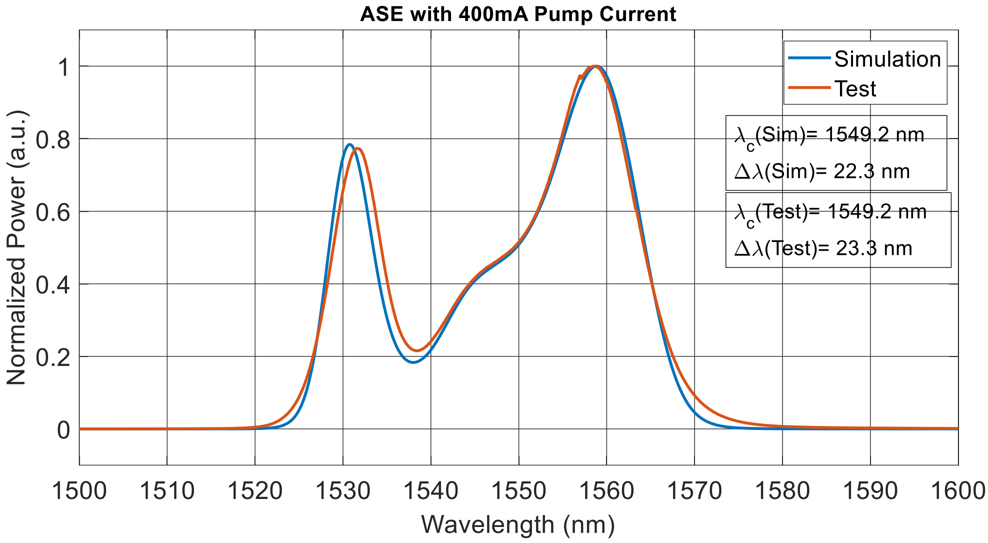

Figure 3.41. Experimental and simulation results of the optical spectrum of the 10 m Er-fiber ASE light source

The modeling of the SLD light source was studied quite successfully using the VPI Photonics simulation program. As can be seen in Figure 3.42, the optical spectrums are examined and it is clearly seen that the experimental results are in good agreement with the simulation results. In the simulation environment, the output power is measured as 29 mW and this power can be adjusted as desired. The 3 dB bandwidth is measured as approximately 45 nm.

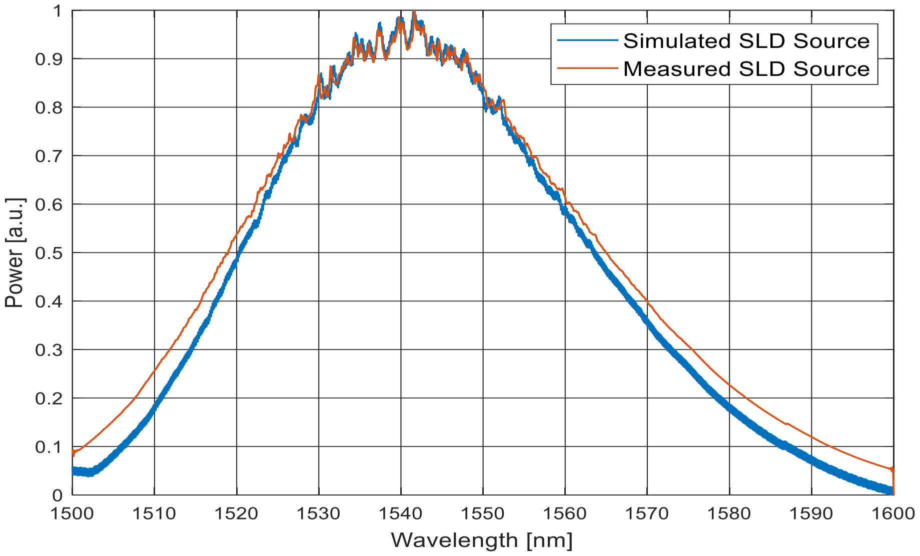

Figure 3.42. Experimental and simulation results of the optical spectrum of SLD

3.2. Characterization of MIOC

In this section, MIOC fabricated by Ti-diffused and APE method is characterized. The patterning process on the substrate is performed in a clean room with photolithography steps. to make a waveguide. Waveguide patterns can be created on a 3" diameter substrate to produce multiple devices with photolithographic techniques.

As a start of this section, lithography techniques used for fabrication of the MIOC with Ti-diffusion and APE methods is briefly described, and then single axis IFOG is established using these MIOCs integrated with the fiber pigtails and tested for the bias measurements under temperature variations.

3.2.1. MIOC Fabrication with Ti-diffusion Method

In Ti-diffusion method, titanium waveguide patterns are formed on the $LiNbO_3$ crystal surface. Photolithographic techniques are primarily used to create a waveguide pattern on the LiNbO3 crystal. Ti-diffusion method for MIOC fabrication is processed as shown in Figure 3.43.

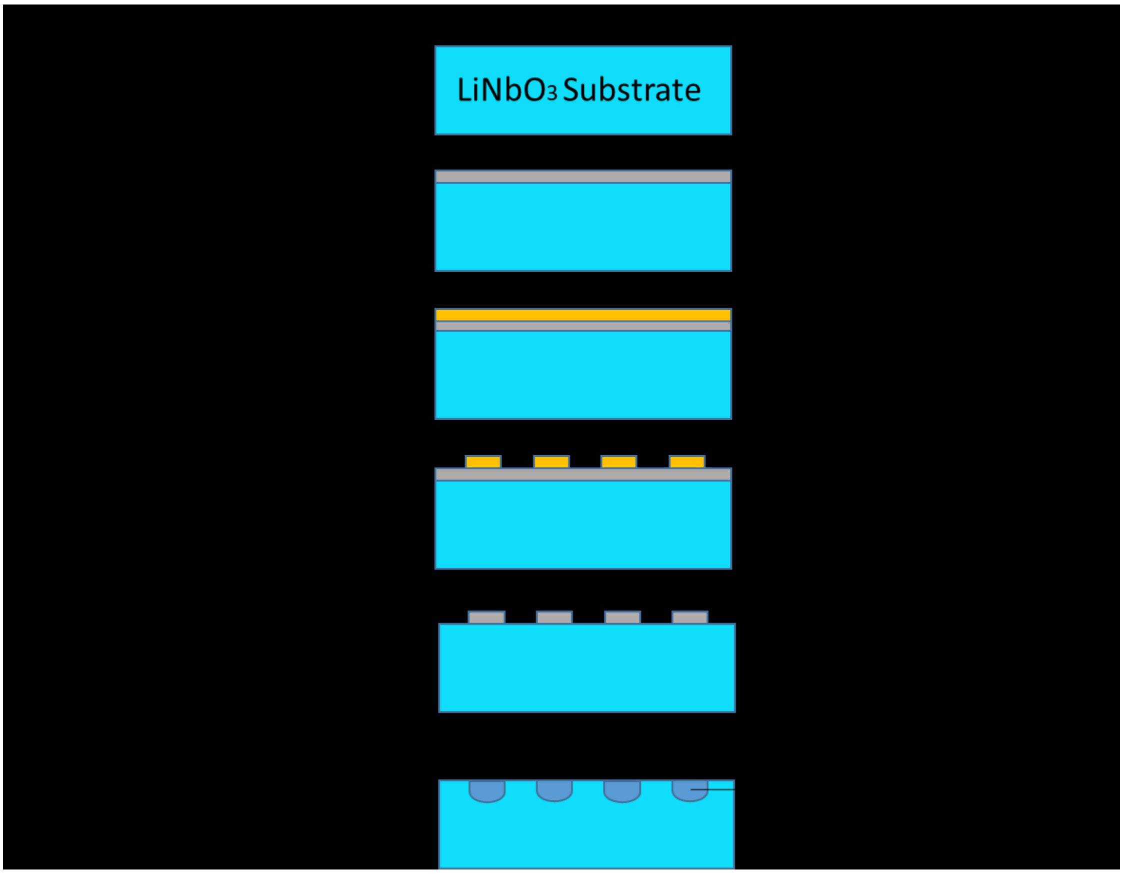

Figure 3.43. Ti-diffusion method for MIOC fabrication

As a first step, a 3" x-cut $LiNbO_3$ wafer is coated with 80 -90 nm thick titanium metal using an electron beam physical vapor deposition (PVD) system as shown in Figure 3.44.

Figure 3.44. PVD system

After that, the wafer is coated with a positive photoresist using a generic spin coater (Figure 3.45-a), and then the wafer is baked around 100 ˚C for 2-3 minutes using a hot plate (Figure 3.45-b).

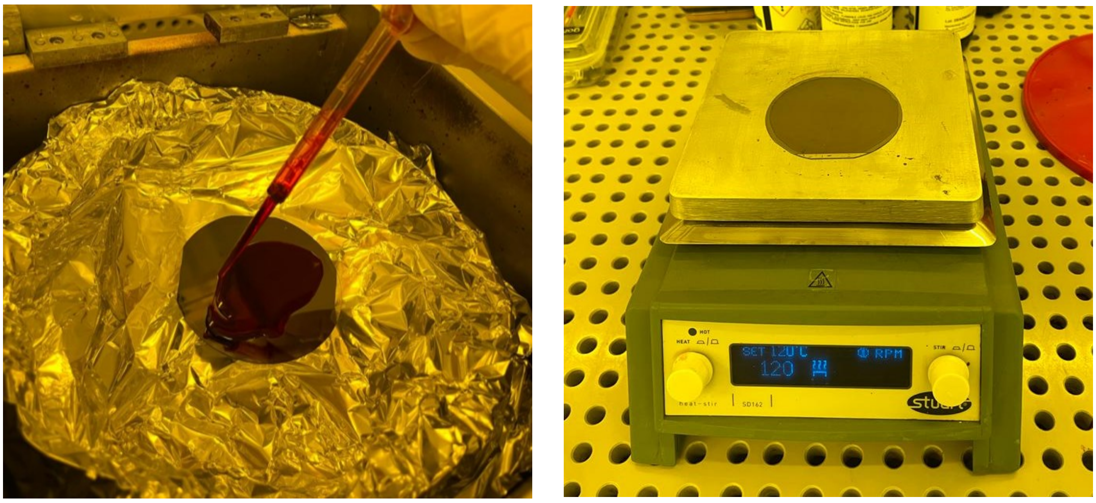

Figure 3.45. (a) Spin coating process of Ti-coated $LiNbO_3$ wafer and (b) LiNbO3 wafer before UV exposure

The wafer is exposed to UV light to pattern waveguides with a special mask using a mask aligner as shown in Figure 3.46. Resist-coated wafer is loaded into the Mask Aligner (MA-6), aligned with the mask and then UV light is applied. In this way, the pattern on the mask is transferred to the wafer surface.

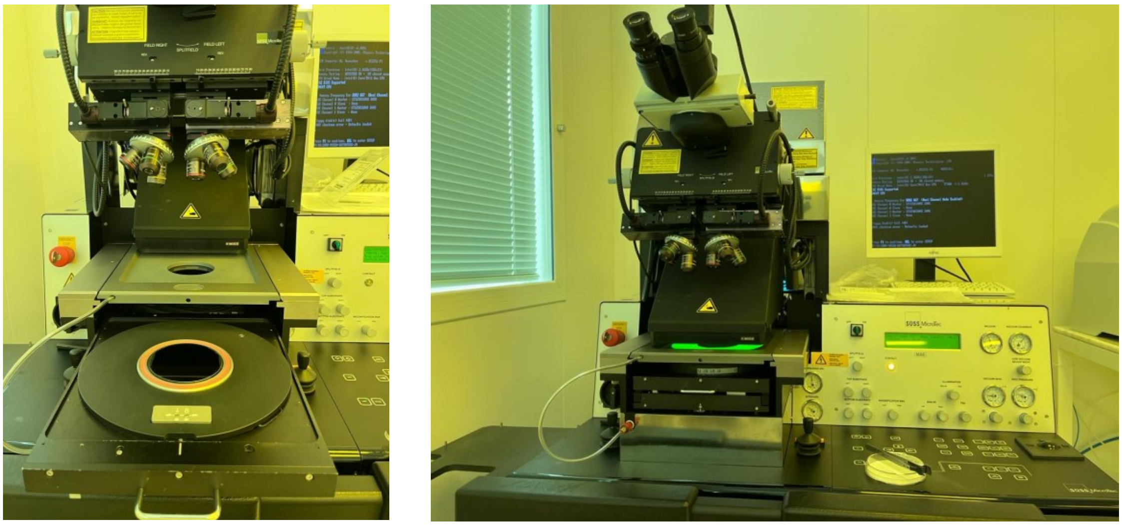

Figure 3.46. Mask aligner and photolithography system (Karl Suss MA6)

After the UV exposure, the patterns are developed in a special solution. LiNbO3 wafer before the fabrication process and LiNbO3 wafer with waveguide patterns are given in Figure 3.47 (a) and (b), respectively.

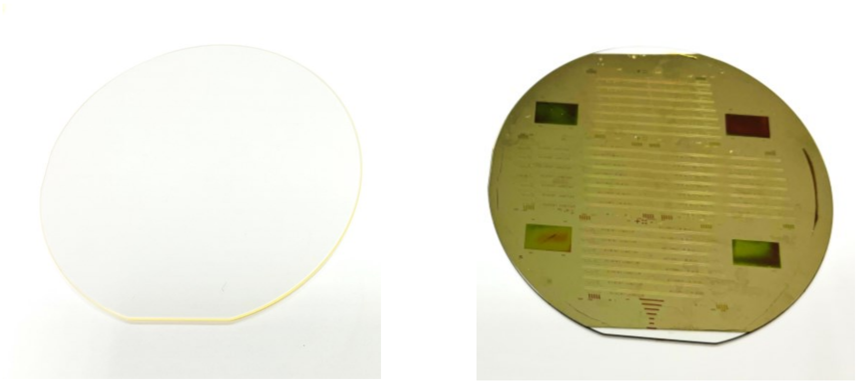

(a) (b)

Figure 3.47. LiNbO3 wafer (a) before the fabrication process, (b) with waveguide patterns

After development of the photoresist, Ti metals that were not protected by the resist on the wafer is dip-etched in a diluted HF solution 30:1:1 DI-water:H_2O_2:HF. When dip-etching process is completed, the remaining photoresists are removed to prepare the wafer for titanium diffusion as shown in Figure 3.48.

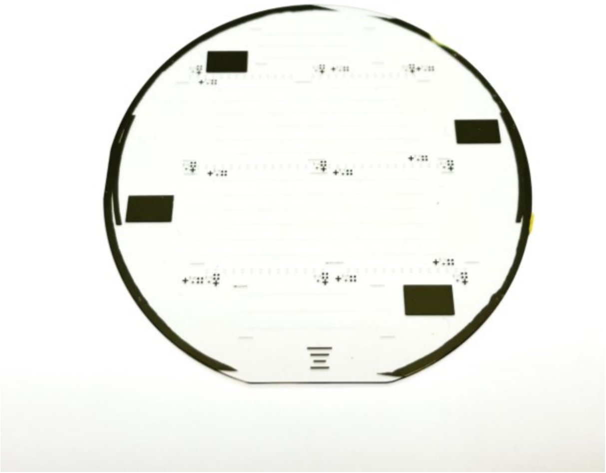

Figure 3.48. LiNbO3 wafer after Ti-etch

As a detailed on microscope, the y-coupler region and width of the waveguides are viewed in detail for process monitoring. Microscope images of y-coupler region and 7um width waveguide are seen in Figure 3.49.

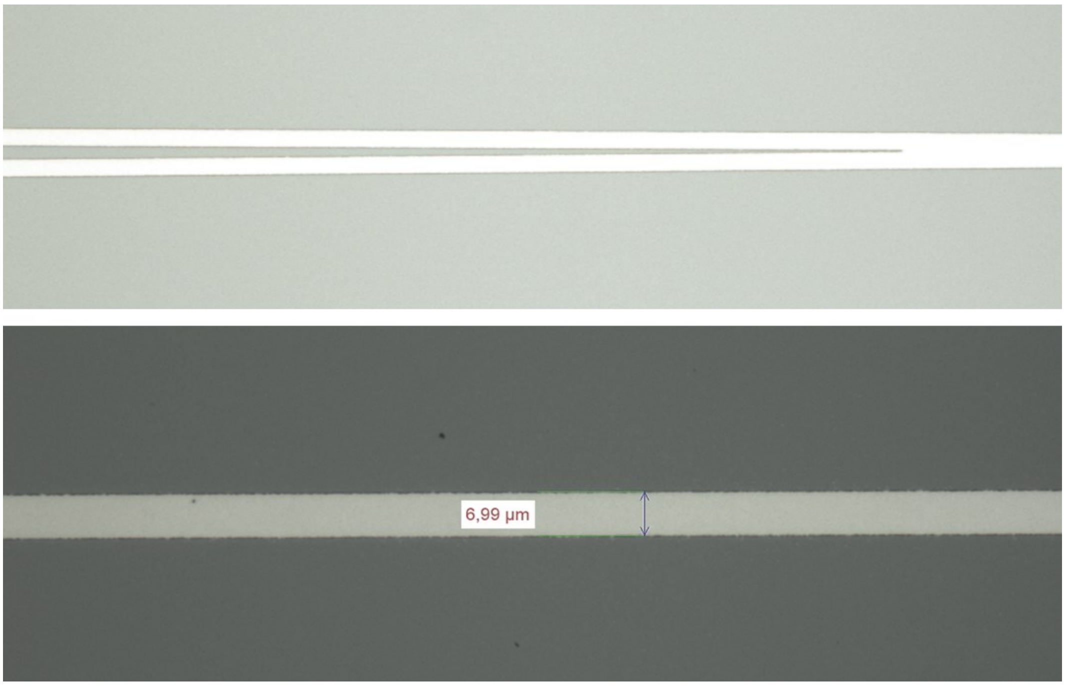

Figure 3.49. Microscope image of waveguides patterned with Ti-metals (a) y-coupler region (b) 7 um waveguide

The next step of the fabricated wafer for waveguide formation is the diffusion of the Ti- metal into the LiNbO3 wafer. Various time and temperature parameters have been studied for the optimization of diffusion. For optimum efficiency, diffusion parameters were carried out in a tube furnace that gradually increased the temperature from room temperature to around 1000 degrees for 8-10 hours. Ti-ions dope into the wafer and change the refractive index in this region, and waveguides are formed in this way.

3.2.2. MIOC Fabrication with APE Method

In APE method, waveguides are formed on the $LiNbO_3$ crystal surface with proton exchange method. Titanium metal is used as a mask in the ion exchange in acid in the APE method. Photolithographic techniques are primarily used to create a waveguide pattern on the $LiNbO_3$ crystal like as Ti-diffusion method. The schematic view of the APE method is given in Figure 3.50.

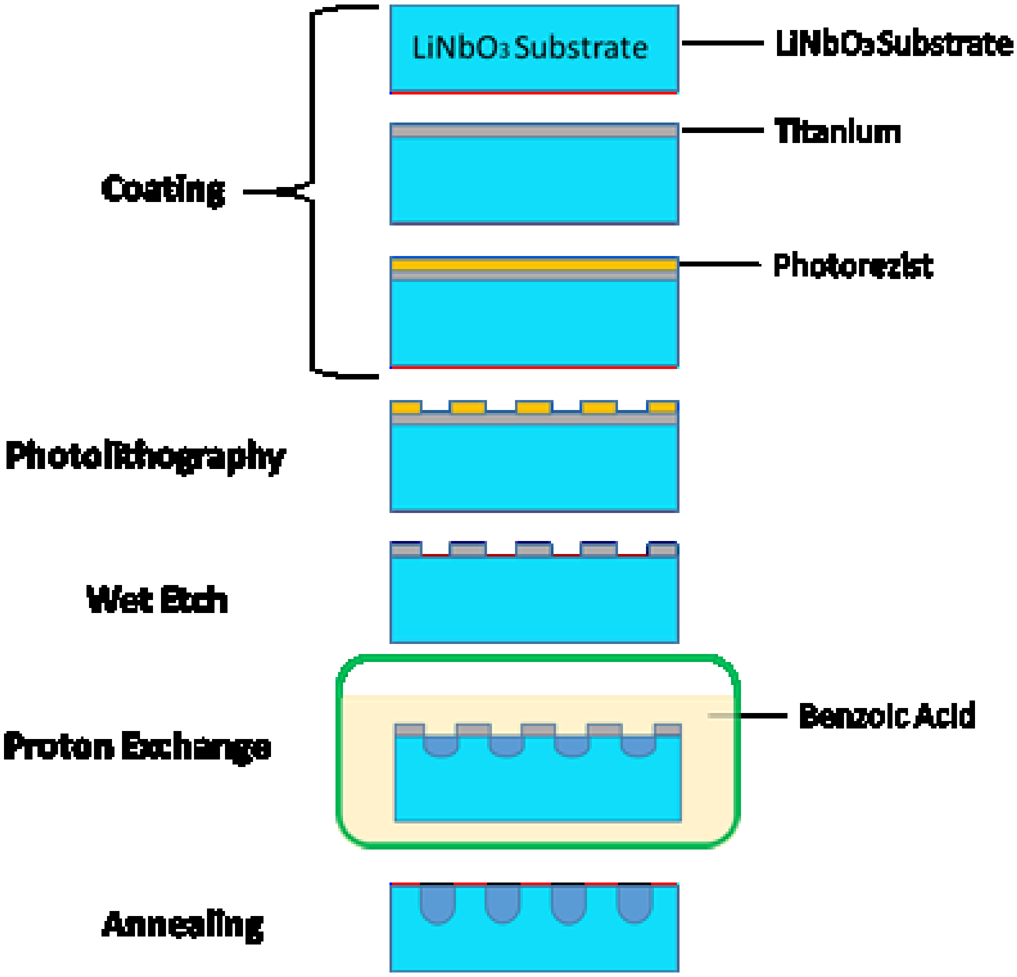

Figure 3.50. APE method for MIOC fabrication

As a first step, a 3" x-cut $LiNbO_3$ wafer is coated with 30 - 50 nm thick Ti- metal using a PVD system. After that, the wafer is coated with a positive photoresist using a generic spin coater, and then the wafer is baked around 100 °C for 2-3 minutes using a hot plate. The wafer is exposed to UV light to pattern waveguides with a special mask using a mask aligner. Then, the patterns are formed in a developer solution (Figure 3.51).

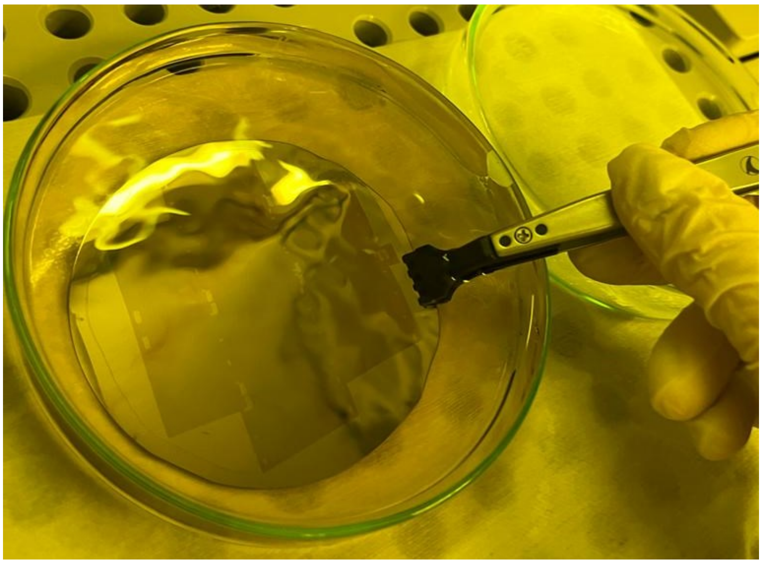

Figure 3.51. Development of patterns after UV expose

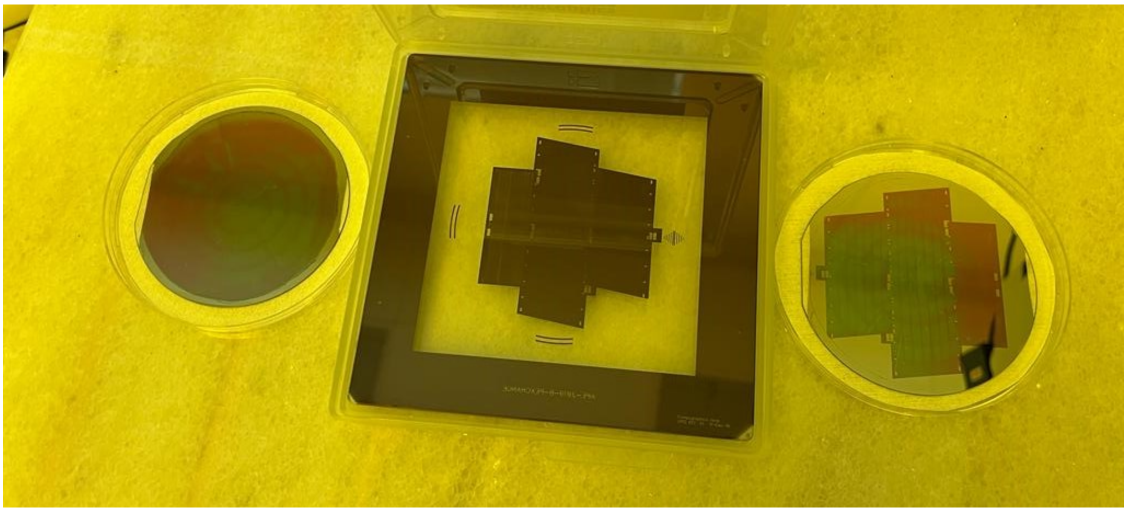

Figure 3.52. Patterning process for proton exchange

After development of the photoresist, Ti metals which not protected by photoresist, removed by the Ti-etchant solution. When etching process is done, the wafer is ready to proton exchange annealing.

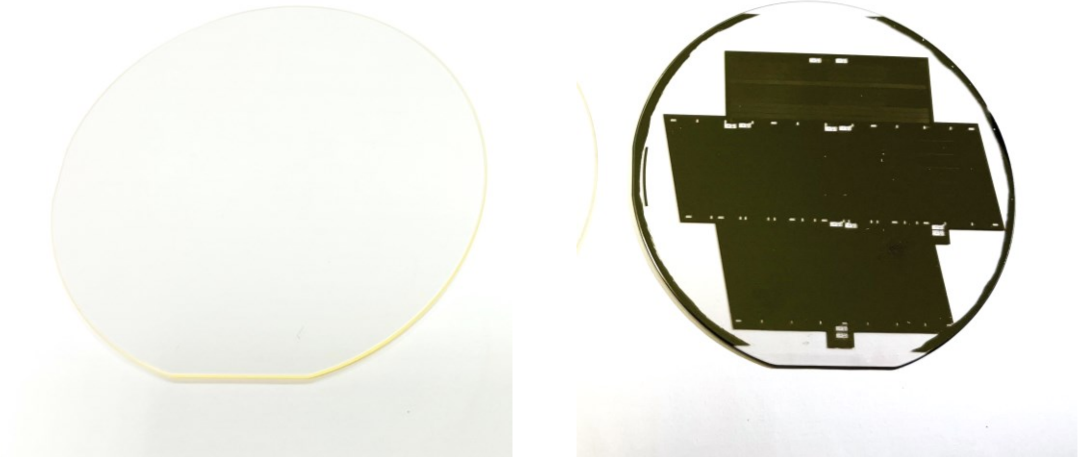

(a) (b)

Figure 3.53. LiNbO3 wafer (a) before the fabrication process and (b) patterned for the proton exchange process

As detailed on the microscope, the y-shape of the patterns and the waveguide width is measured for process monitoring. Microscope image of the waveguides is seen as shown in Figure 3.54.

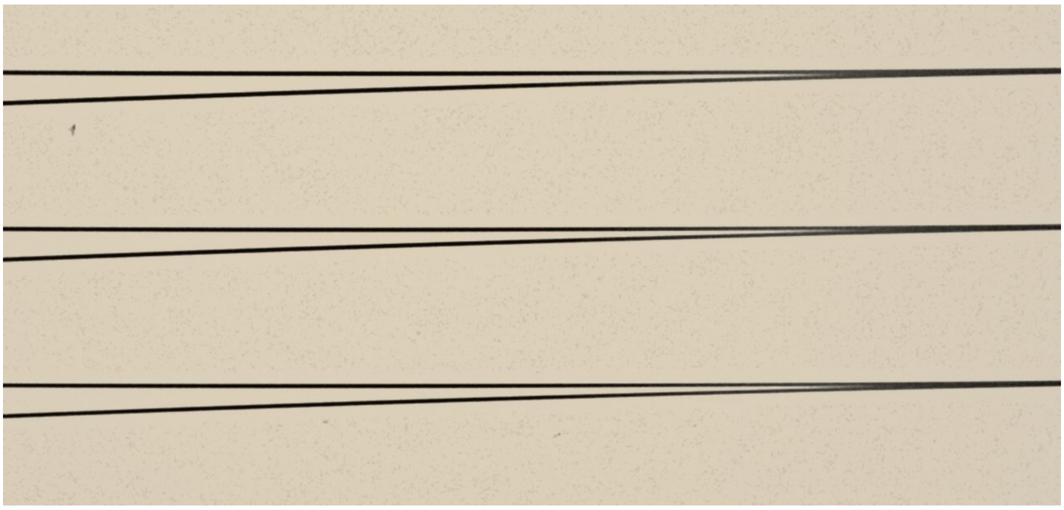

Figure 3.54. Microscope image of waveguides patterned by the PE process

At this point, proton exchange parameters such as temperature, time and rate of chemical solution have been studied for the optimum index change. The proton exchange process is done in a benzoic acid solution that is used as a proton source. The benzoic acid solution is heated up to 200-230 °C and the wafer is immersed into this hot solution and remains for 3 hours. During this 3 hour period, the lithium ions (Li+) on the surface of the $LiNbO_3$ wafer that not protected by Ti metal are exchanged with hdyrogen ions (H+) in benzoic acid. With the placement of hydrogen ions inside the LiNBO3 wafer, the refractive index increases in this region. In this way, waveguides are formed Figure 3.54. Then, the Ti metals on the wafer are etched in a Ti-etchant solution.

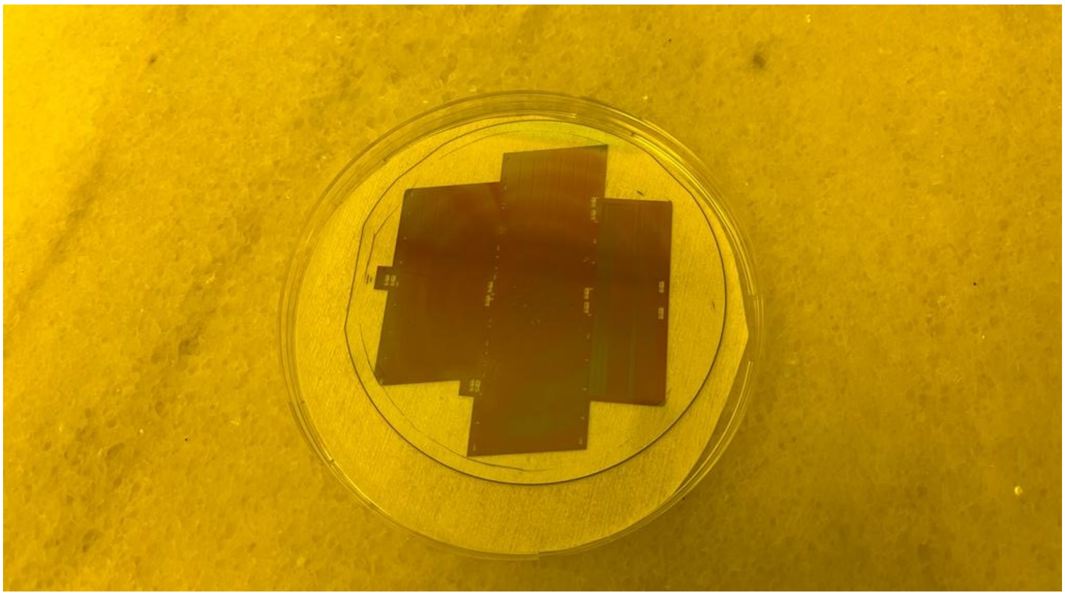

Figure 3.55. LiNbO3 wafer after proton exchange

Following the proton exchange process, the wafer is annealed at about 400 degrees, and the H ions in the waveguide parts penetrate the deeper parts of the plate, increasing the waveguide depth. After this process, the wafer is again spin coated with a negative type photoresist to pattern the electrodes. For the electrode fabrication, the same lithographic fabrication steps are applied for the APE wafer and the Ti diffused wafer. The schematic view of the fabrication steps of electrode lithography is shown in Figure 3.56.

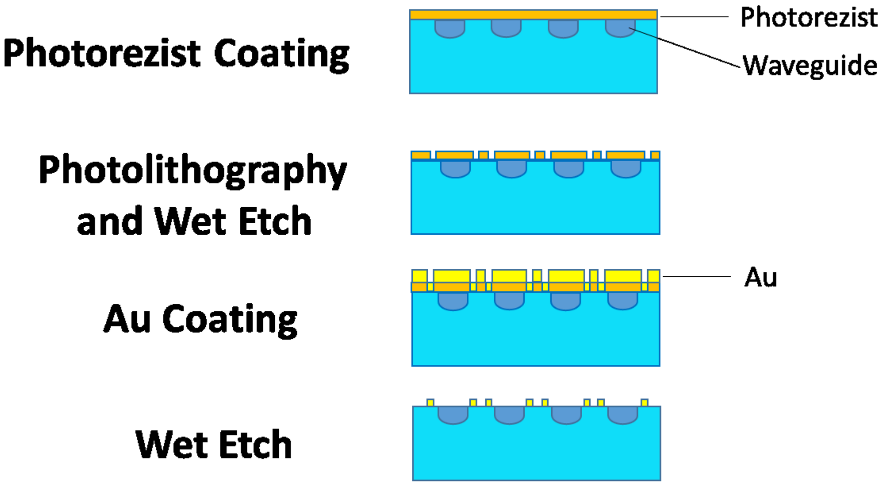

Figure 3.56. Electrode lithography

The coated photoresist is exposed to UV light with the electrode mask and developed using a suitable developer solution. The patterned wafer is then coated with 250-300nm Au metal using a PVD system. After that, the wafer is immersed in a solvent for the lift off process. After the lift-off process, electrodes are formed on the wafer. The wafer pictures before liftoff and after lift off can be seen, respectively in Figure 3.57 (a) and Figure 3.57 (b).

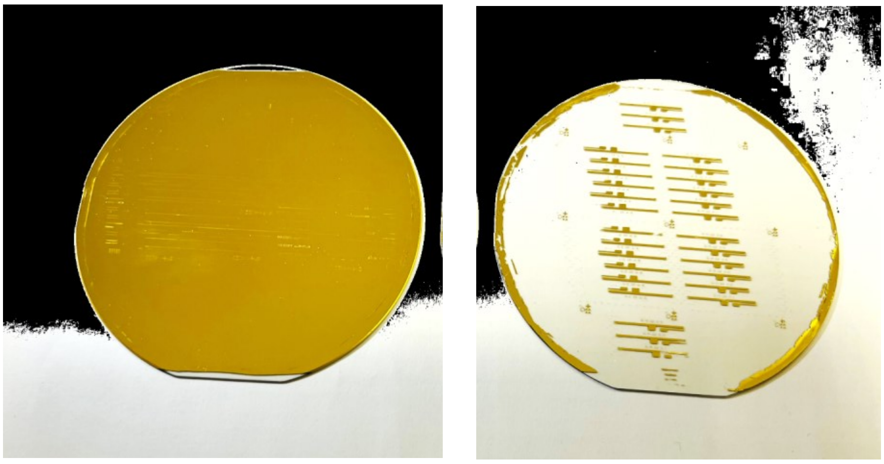

(a) (b)

Figure 3.57. LiNbO3 wafer (a) gold coated wafer for electrode fabrication (b) after electrode lift-off

With the completion of the electrode fabrication, the fabrication steps performed in the clean room are completed. In order to prevent reflection in the areas where the light enters and exits, lapping and polishing should be applied to the device inputs and outputs. For this purpose, lapping and polishing process is applied by separating the wafer into smaller device groups in the dicer and when the required optical quality is reached, the devices are cut back into the dicer one by one. In Figure 3.58, device groups and cut-off devices can be seen in the dicer, respectively.

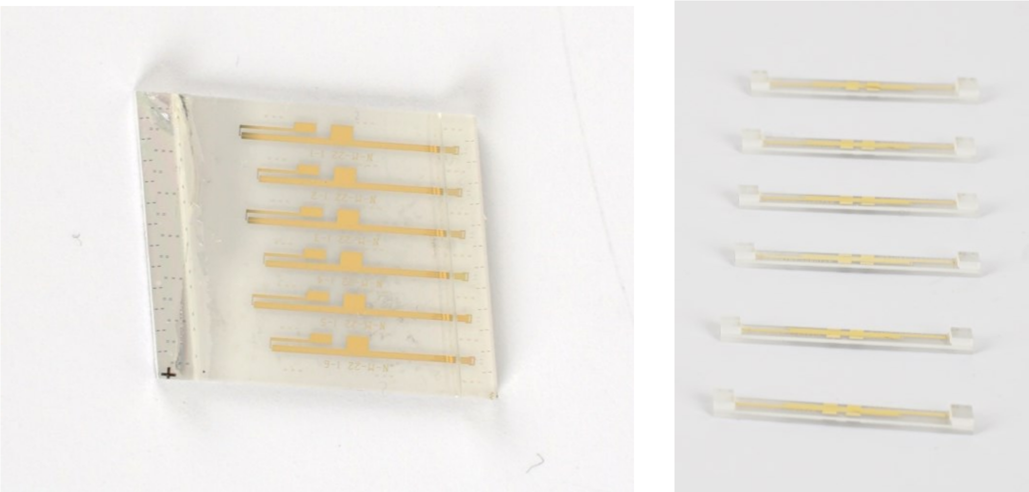

Figure 3.58. A diced LiNbO3 wafer piece for lapping and polishing process

It is connected by a wire-bond between MIOC electrode and MIOC carrier plate for the MIOC modulation connection (Figure 3.59). Afterwards, the MIOC modulation connection is ready to be completed with modulation cable solders on the Printed Circuit Board (PCB) carrier plate.

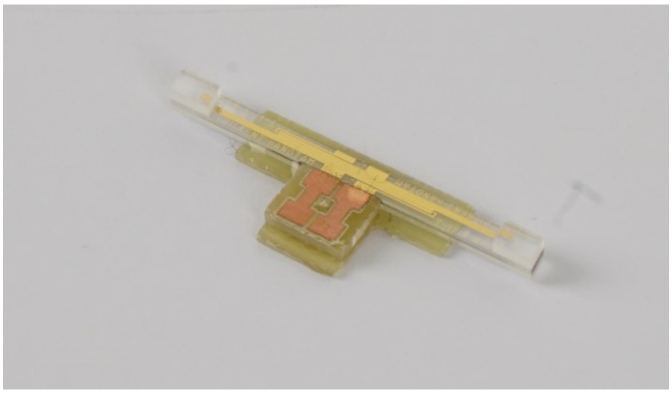

Figure 3.59. MIOC that have a wirebond

In order to connect MIOC with the coil, it must be integrated with PM fiber. MIOC's inlet and outlet surfaces are aligned with a fiber-carrying pigtail, and when UV cured epoxy is applied and UV is applied, MIOC and PM fiber connection is permanently ensured. (Figure 3.60-a). Afterwards, the MIOC is placed in a special case and the cable soldering is completed and then the MIOC production is completed from start to finish (Figure 3.60- b).

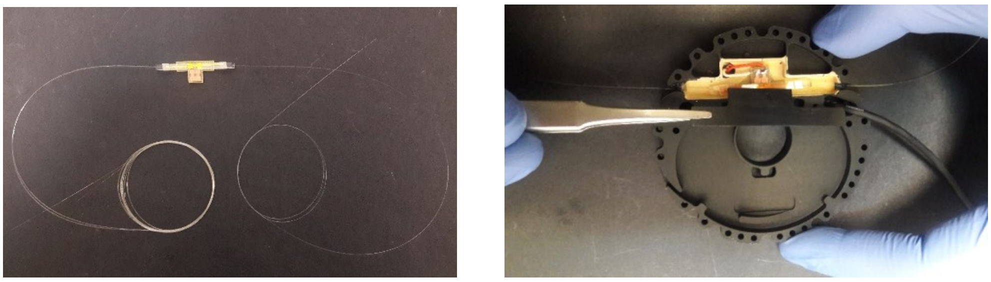

(a) (b)

Figure 3.60. MIOC (a) integrated with fiber pigtails and (b) placed in optical tray

3.2.3. Temperature Characterization of MIOC

The MIOCs fabricated with two different method is tested under temperature variations for characterization of the thermal behavior of the MIOC. In all of the measurements, the same configuration, including a light source, coupler, photodetector, polarizer, and the fiber optic coil, is used for one variable at a time, just to observe the results due to different MIOC. The specified tests are carried out in the climatic chamber at a heating and cooling rate of 1°C/min, in the temperature range of -40°C to +60°C as shown in Figure 3.74.

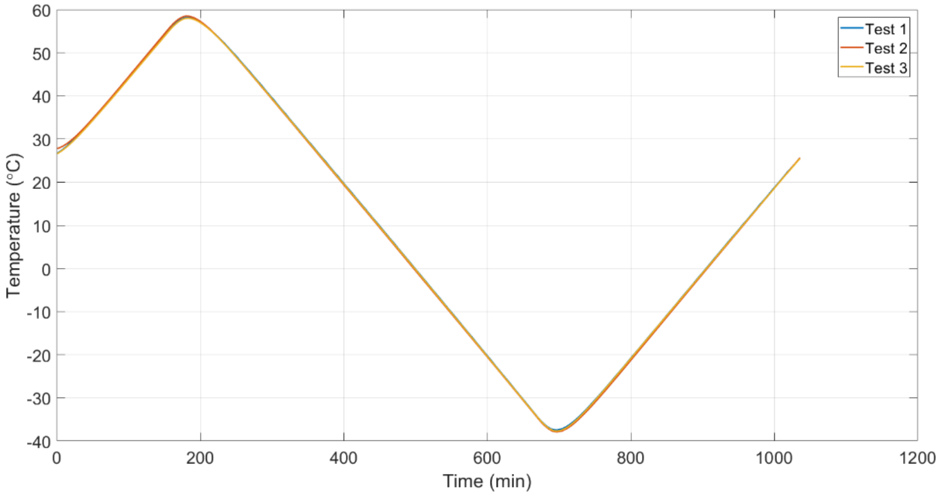

Figure 3.61. Temperature profile used in the temperature-dependent rate measurement of an IFOG

MIOC and the fiber optic coil that integrated carefully for the temperature-dependent rate measurement.

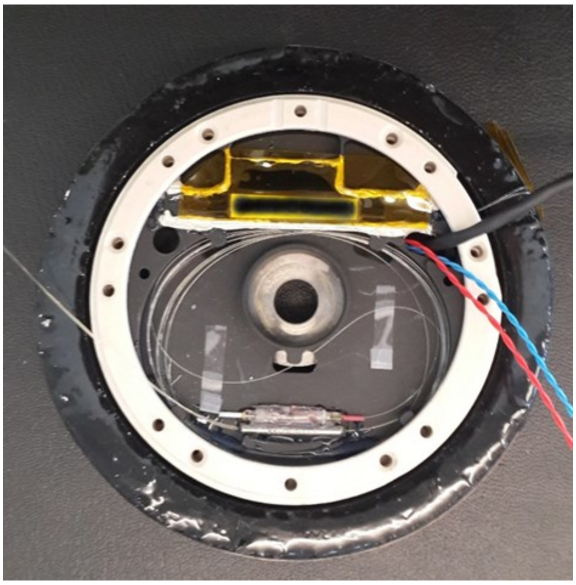

Figure 3.62. The MIOC and the fiber optic coil that integrated carefully for the temperature-dependent rate measurement

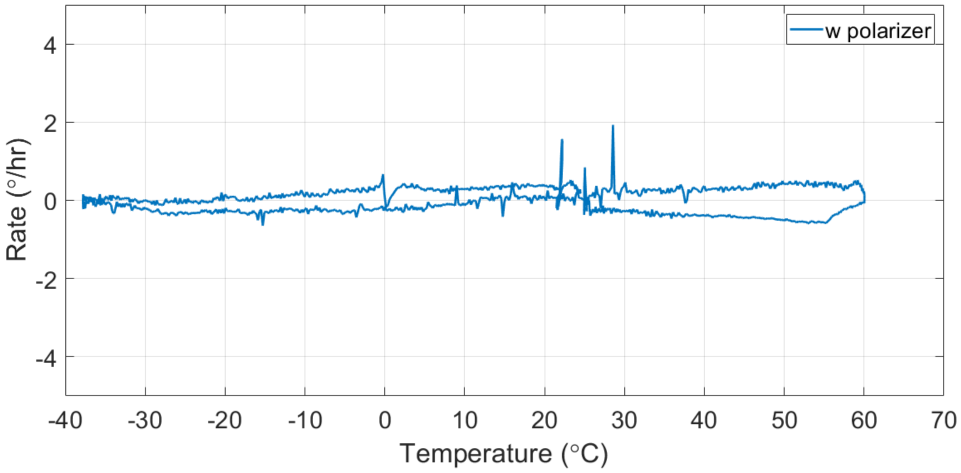

Figure 3.63. Temperature-dependent rate measurement of the IFOG integrated with the polarizer and the MIOC fabricated by the Ti-diffusion method

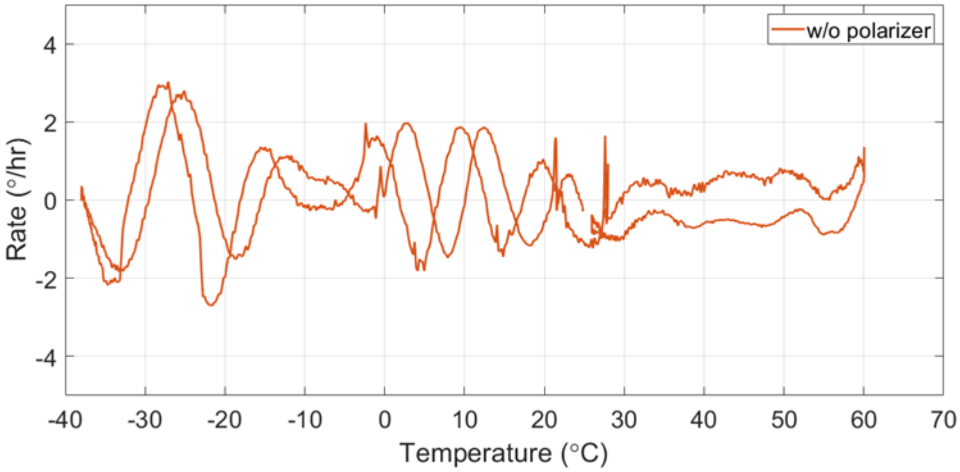

Figure 3.64. Temperature-dependent rate measurement of the IFOG integrated using MIOC fabricated by the Ti-diffusion method without polarizer

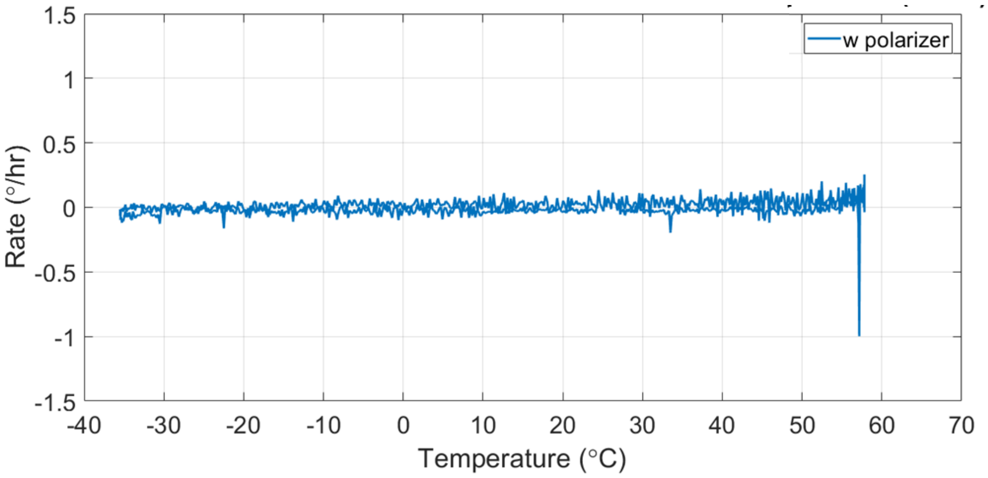

Figure 3.65. Temperature-dependent rate measurement of the IFOG integrated with polarizer and MIOC fabricated by the APE method

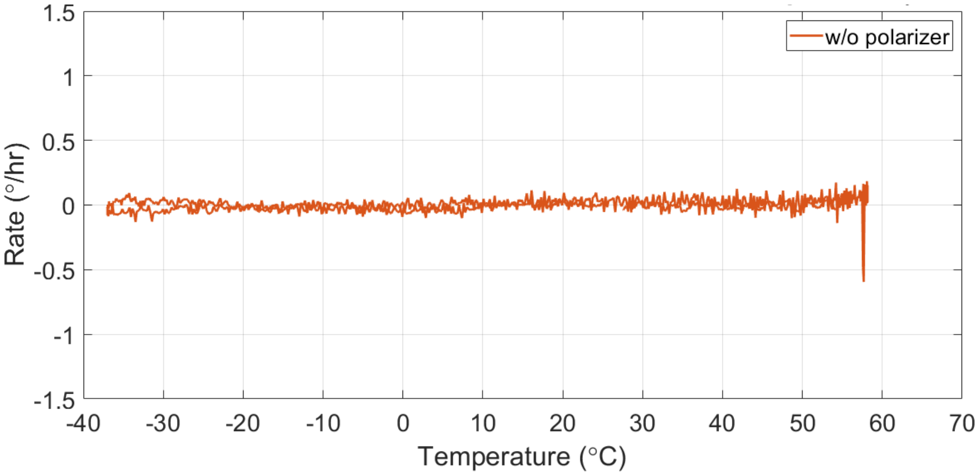

Figure 3.66. Temperature-dependent rate measurement of the IFOG integrated using MIOC fabricated by the APE method without a polarizer

The temperature-dependent rate measurement of IFOG, the performance integrated using MIOC fabricated by the APE method, and the Ti-diffusion method without a polarizer are clearly shown the Figure 3.67.

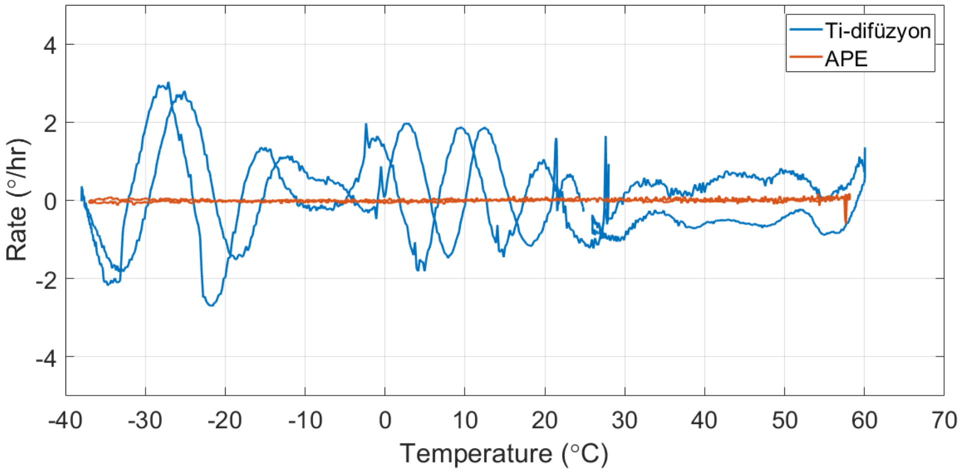

Figure 3.67. Comparison of temperature-dependent rate measurement of the IFOG integrated using MIOC fabricated by the APE method and Ti-diffusion method without a polarizer

Table 3.5. Bias error of MIOC fabricated by different methods

MIOC Fabrication Method	Polarizer	Bias Error (°/h)/(°C/min)
Ti-diffusion	w/o polarizer	1.62
Ti-diffusion	w polarizer	1.14
APE	w/o polarizer	0.08
APE	w polarizer	0.13

The temperature-dependent rate measurement of the IFOG integrated using MIOC fabricated by Annealing Proton Exchange (APE) and Titanium diffusion (Ti-diffusion) methods have been examined and characterized. The system performance of the MIOC fabricated by the APE method and Ti-diffusion method without polarizer have been analyzed and the bias error is reduced more than 20 times by using MIOC fabricated by the APE method.

3.3. Characterization of the Fiber Optic Coil

The fiber optic fiber optic coil is the heart of an optical sensor in which the mutually advancing light in moving systems is measured with the effect known as the Sagnac Effect. An IFOG has optical structures that are used to measure the amount of phase difference that occurs relative to each other due to the system movement of the counterpropagating light, consisting of meters of fiber length calculated in advance according to their sensitivity and capable of precise measurement. Time-dependent environmental factors such as temperature change, vibration, and magnetic field can directly affect the fiber optic coil performance. It is of great importance to increase the bias sensitivity in a fiber optic coil performance in order to make the phase difference measurement without an error and to minimize the environmental effects. The thermal sensitivity of IFOG is suppressed to a degree by various fiber optic coil winding methods [70,71] and novel fiber technologies are introduced to IFOG for lower thermal sensitivity [72,73].

3.3.1. Mechanical Properties of Fiber Optic Coil Adhesive

The phase difference measured by the fiber optic coil directly determines the IFOG performance; Changes in environmental conditions such as vibration and temperature, fiber optic coil winding pattern and some factors such as the elastic modululus value of the adhesive material applied during winding directly affect the measurement of the phase difference. While the temperature change causes change in the physical dimensions of the coil, the mechanical stresses caused by vibration can turn into thermal deflection, which is directly proportional to the bias error in the fiber optic coil, by causing thermal stress. In addition, the winding pattern used in the fiber optic coil, the positioning of coil on the spool, and the volume of 20-25% of the adhesive being formed, the physical properties of this adhesive significantly affect the fiber optic coil performance and thereby the IFOG performance. There is a direct proportion between the elasticity modulus of the adhesive used in the fiber optic coil and its mechanical strength; The adhesive material has a great effect on reducing the mechanical stress of the fiber optic coil.

It is of great importance to accurately measure the phase difference in the fiber optic coil, which directly determines the performance of the IFOG. In ideal conditions, it seems sufficient to use PMF in the fiber optic coil and to create the fiber optic coil flawlessly with one of the appropriate winding patterns. Due to the changes in the environmental conditions where the fiber optic coil causes disturbances in the optical path, it should be developed. Time-dependent environmental effects as described temperature fluctuations and vibration, create a mechanical stress on the fibers that are forming the fiber optic coil and this causes the phase drift of the counterpropagating light through the fiber. Therefore, the adhesive used in the fiber optic coil should be flexible enough to reduce the effects of vibration and have a high mechanical strength in order to reduce the mechanical stress caused by temperature at the same time. Adhesives with an elastic modulus of around 10 MPa are suitable to absorb the vibration effect and reduce mechanical stress due to temperature. At that point we tried to mix some materials with each other to have optimum elasticity for fiber optic coil with high precision. The mechanical performance of the adhesive composition is determined with the tensile test.

The tensile test is one of the most important methods used to determine the mechanical properties of materials. The test is generally applied to determine the strength of materials under static loads. In this method, samples with cylindrical and sometimes different geometric sections are subjected to an ever-increasing tensile stress and their resistance against tensile stresses are investigated. The test is performed using test specimens prepared according to certain standards, and the tensile load is increased along the longitudinal axis at a constant speed and temperature until the specimen breaks. The tensile load applied to the specimen from the beginning to the end of the test and the amount of elongation that occurs in the specimen are recorded depending on time. By using the obtained data, the load-elongation ($F–\Delta L$) curve or engineering stress- strain ($\sigma–\varepsilon$) curve of the material is obtained.

The two ends of the specimen are firmly attached to the clamping head of the mechanical tester to load tension in the thinned-in-center specimen prepared according to the ISO standards. The clamping heads are moved away from each other and, in the meanwhile, the material is loaded with tensile stress.

The widespread use of the tensile test is the direct use of the material properties obtained as a result of the test in engineering calculations. By using the stress-strain curve obtained as a result of the tensile test, the following mechanical properties of the material from which the sample is prepared can be found as Modulus of elasticity - Limit of elasticity -

Maximum tensile strength - Resilience - Toughness - Yield stress - % elongation - % section contraction. Many standard organizations such as American Society of Testing Materials (ASTM), British Standards (BS), Deutsches Institut für Normung (DIN) and International Standards Organization (ISO) have prepared tensile test specifications. In these specifications, the requirements for test apparatus, test specimens and test processes are determined. Standard tensile tests are performed using specially prepared tensile specimens with specific geometric properties as shown in the ASTM standard.

A tensile test sample prepared according to the ISO standard is shown in Figure 3.68. Although the tensile test samples used for different materials are the same in geometrical shape, changes can be seen in the dimensions given in Figure 3.68. The two ends of the specimen are firmly attached to the clamp heads of the mechanical tester to create stress in the thinned specimen. The clamping heads are moved away from each other and meanwhile, the material is loaded with tensile stress.

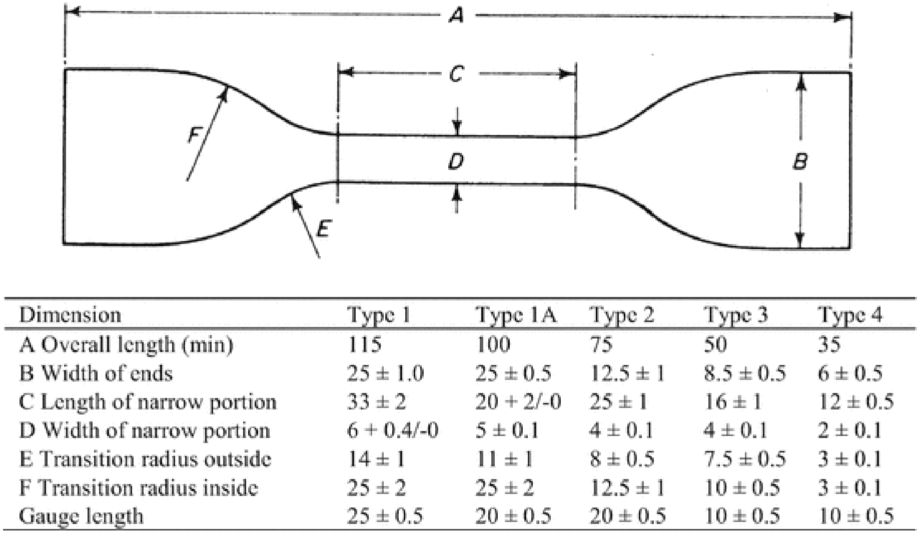

Dimension	Type 1	Type 1A	Type 2	Type 3	Type 4
A Overall length (min)	115	100	75	50	35
B Width of ends	25 ± 1.0	25 ± 0.5	12.5 ± 1	8.5 ± 0.5	6 ± 0.5
C Length of narrow portion	33 ± 2	20 + 2/-0	25 ± 1	16 ± 1	12 ± 0.5
D Width of narrow portion	6 + 0.4/-0	5 ± 0.1	4 ± 0.1	4 ± 0.1	2 ± 0.1
E Transition radius outside	14 ± 1	11 ± 1	8 ± 0.5	7.5 ± 0.5	3 ± 0.1
F Transition radius inside	25 ± 2	25 ± 2	12.5 ± 1	10 ± 0.5	3 ± 0.1
Gauge length	25 ± 0.5	20 ± 0.5	20 ± 0.5	10 ± 0.5	10 ± 0.5

Figure 3.68. ISO-37 specimen geometry

Stress is the load acting on the unit area, denoted by the symbol (σ) and calculated with the following Equation,

$$\sigma = P/A_0 \qquad (N/mm^2) \tag{3.3}$$

Strain is defined as the elongation per unit length and it is calculated by the following Equation,

$$\varepsilon = \frac{L - L_0}{L_0} = \frac{\Delta L}{L_0} \qquad \text{(mm/mm)} \tag{3.4}$$

In the linear region of the tensile curve, the metal sample deforms elastically. That is, the sample returns to its initial length when the load on the sample is removed. The slope of the linear region in this first part of the stress-strain diagram obtained as a result of the tensile test gives the elastic modulus or Young's modulus (E) of the material. In the stress-strain diagram, the Equation given below and called Hooke's Law is valid in the elastic region where the modulus of elasticity is calculated.

$$dE = \sigma E \, / \, \varepsilon E \tag{3.5}$$

3.3.2. Tensile Stress Measurements of an Adhesive Mixture

An Adhesive mixture developed to reduce random errors that occur as a result of mechanical stress on the fiber optic coil due to time-dependent changes in environmental conditions such as temperature change and vibration in IFOGs has been analyzed. In this study, samples of a homogeneous adhesive with high mechanical strength and moisture resistance, containing a base material, drying agent, carbon black (C) and bifunctional organosilane-containing surface agent, used in fiber optic coil is studied. The adhesive mixture composition is basically; a base material with a soft structure and low fluidity, operating in the temperature range of -50°C to +200°C, with a viscosity of 2-4 Pa and a tensile strength of 5.5-8.7 MPa at 24°C; a colorless and hydrophobic drying agent with a low viscosity, preferably 50-150 mPa at 24°C, allowing to increase the number of bonds in the three-dimensional polymer network. It contains carbon black (C) with a particle size of 200-300 nm mixed to increase the mechanical properties and a surface agent containing bifunctional organosilane with high surface adhesion and moisture resistance, colorless, low viscosity, and hydrophobic structure.

The base material is preferably selected as a silicone (Si) based adhesive. The silicone-based adhesive is a polymeric material consisting of hydrogen (H), oxygen (O), and carbon (C) atoms or combinations of these atoms bonded with the silicon atom, preferably selected from the group of silanol (SiH_4O), alkoxy (R–O–), or vinyl ($-CH=CH_2$). It has a soft structure with a hardness degree of Shore A class 40-65 and a structure that can be cured with heat curing.

The drying agent in the mixture is used to increase the number of bonds in the three-dimensional polymer network and preferably has a polymeric structure consisting of amine or polyamide group elements. The drying agent, which is colorless and hydrophobic, is preferably added in an amount of 5% by weight based on 100% of the total adhesive composition.

The carbon black is added in order to increase the modulus of the adhesive mixture. In the mixture, the C is used in powder form with a particle size of 200-300 nm, preferably 40% by weight based on 100% of the total adhesive composition.

Due to the hydrophobic property of the bifunctional organosilane-containing surface agent, the moisture resistance of the adhesive composition is increased. A surface agent containing preferably glycidyl ($C_3H_6O_2$) and silane (SiH_4) selected from the bifunctional organosilane group is used, preferably 3-glycidyloxypropyltrimethoxysilane (GPTMS: $C_9H_20_5Si$) material is used. GPTMS material has a light turpentine smell, colorless, low viscosity liquid structure. It is a soluble material in alcohol (CnH2n+1OH), ketone (CnH_2NO) and aliphatic (CnH2n+2, CnH2n, CnH2n-2) or aromatic hydrocarbons. In another application of the invention, a vinyl (−CH=CH2) and silane (SiH4)-containing surface agent selected from the bifunctional organosilane group is used. Vinyltrimethoxysilane (VTMO) material has a colorless and low viscosity liquid structure with a typical aromatic odor. During the fiber optic coil winding, the use of the adhesive composition ensures that the mechanical stress that may occur on the fiber, the fiber optic coil is minimized due to moisture. The surface agent is preferably added in an amount of 1% by weight based on 100% of the total adhesive composition.

The method of obtaining a homogeneous adhesive composition with high mechanical strength is as follows:

– add carbon black (C) and surface agent in the base material in the specified proportions,

– mixed preferably for 15-20 minutes in a magnetic stirrer to obtain a homogeneous mixture,

– add 50% by weight of methanol to the resulting mixture to ensure complete dissolution of the carbon black,

– The mixture to which methanol is added is mixed with the help of a magnetic stirrer for about 20-30 minutes on a heating plate at 60°C, and homogenized by ensuring that all the methanol evaporates,

- drying agent is added to the homogenized mixture obtained by the evaporation of all methanol as a result of the mixing process,

– After adding the drying agent, it is mixed preferably in a magnetic stirrer for 15-20 minutes to obtain a homogeneous mixture,

– The adhesive mixture is heated from room temperature (25°C) to 75°C with a heating rate of 1°C/min. Then kept at 75°C for 18 hours, and then cooled from 75°C to 25°C with a cooling rate of 1°C/min.

In order for the adhesive composition to function adequately, the adhesive mixture prepared by the method described in detail above needs to be cured, and Figure 3.69 shows the temperature profile used for curing. The adhesive mixture is heated in a controlled oven or air-conditioning chamber from room temperature (25°C) to 75°C with a heating rate of 1°C/min for 50 minutes and then kept at 75°C for 18 hours. A curing profile is completed by decreasing from 75°C to room temperature for 50 minutes with a cooling rate of 1 °C/min. Curing temperature profile takes a total of 19 hours and 40 minutes. In the graph, the "Determined Value" expressed with a solid line represents the profile applied for curing, and the "Test Value" expressed with a dashed line represents the temperature value applied while the adhesives are curing in the chamber.

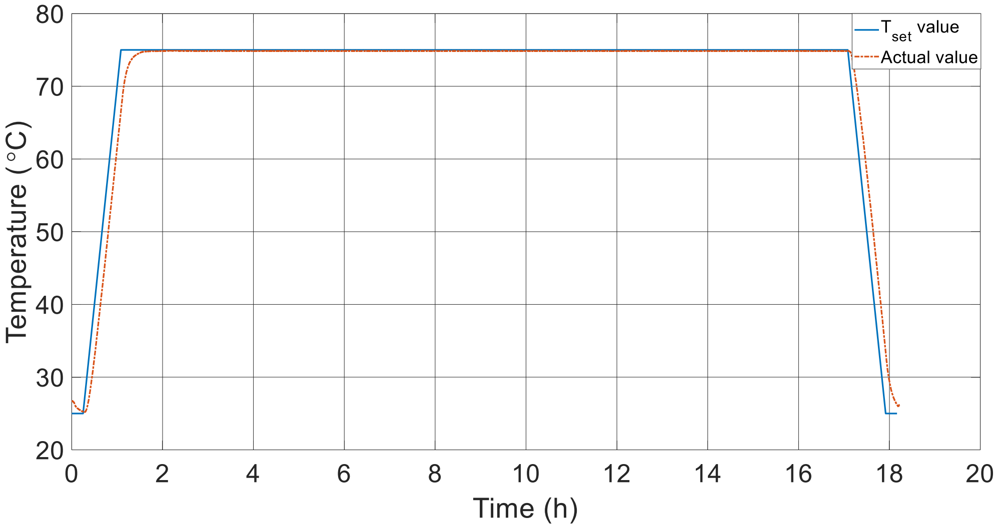

Figure 3.69. Temperature profile approved for the curing mixture of adhesive

The weight ratios of the base material, drying agent, C, and surface agent constituting the adhesive composition are 54%, 5%, 40%, and 1%, respectively. If the weight ratios of the base material, drying agent, carbon black, and surface agent of another adhesive mixture tested are 63%, 6%, 30%, and 1%, respectively, and for another test, the weight ratios of base material, drying agent, carbon black and surface agent is mixed as 72%, 7%, 20%, and 1%, respectively.

Figure 3.70. Specimen prepared with Universal ISO-37.1 die cutter for tensile tests

The base material, curing agent, C, and adhesion promoter are prepared and cured mixture is prepared with universal ISO-37.1 die cutter for the preparation of sample adhesive mixture specimens for tensile stress tests. On the basis of ASTM standards, a subsize rectangular tensile specimen have a gauge length of 23 mm, a width of 3.2 mm, a thickness of 0.3mm for the tensile test. The cured mixtures are prepared with universal ISO-37.1 die cutter for preparation of sample adhesive mixture specimens for tensile tests (Figure 3.70). The sample drawing speed is determined as 5 mm/min and according to the results, the data obtained for 4 samples are given in Figure 3.71.

Table 3.6. Compositions of adhesive mixtures

	Base material (%)	**Curing agent (%)**	**Cabon black (%)**	**Adhesive promoter (%)**
Adhesive Mixture #1	91	9	-	-
Adhesive Mixture #2	55	5	40	-
Adhesive Mixture #3	54	5	40	1
Adhesive Mixture #4	54	5	40	1

A stress-strain measurement of the adhesive compositions has been proven 4 times and the comparative stress-strain graphics of the adhesive compositions are given in Figure 3.71.

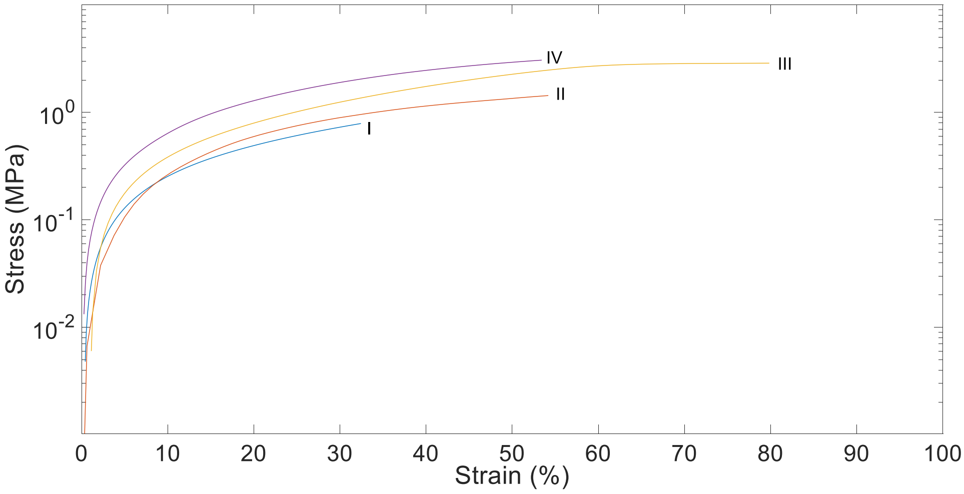

Figure 3.71. Stress-strain graphic of four adhesive mixtures with a different composition

The curve shown in this graph with the number "I" is the mixture obtained with the base material in an amount of 91% by weight of the total composition, and the drying agent in an amount of 9% by weight, on a 100% composition. The curve shown with the number "II" shows the mixture obtained with the base material preferably in an amount of 55% by weight, the drying agent in an amount of 5% by weight, and the carbon black in an amount of 40% by weight, on the basis of 100% of the total composition.

In the stress-strain graph given in Figure-1, the elastic modulus value of the mixture given in the curve shown with the number "I" and the elastic modulus value of the mixture given in the curve indicated with the number "II" are calculated as 2.75 Mpa and 3.14 MPa, respectively.

The curve shown with the number "II" shows the mixture obtained with the base material preferably in an amount of 55% by weight, the drying agent in an amount of 5% by weight, and the carbon black in an amount of 40% by weight, on the basis of 100% of the total composition.

The curves indicated with the numbers "III" and "IV" in the graph in Figure-1 refer to the different application of the adhesive composition; each application of the adhesive composition is based on 100% of the total adhesive composition, preferably 54% by weight of base material, 100% by weight of the total adhesive composition, preferably 5% by weight of drying agent, 100% by weight of the total adhesive composition, preferably 40% by weight of carbon black, and the total adhesive composition. It contains surface agent preferably in an amount of 1% by weight on a 100% basis. The adhesive composition given in the curve shown with the number "III" contains a surface agent containing vinyltrimethoxysilane. The adhesive composition given in the curve shown with the number "IV" contains a surface agent containing GPTMS. In the graph in Figure-1, the modulus of elasticity of the adhesive composition given in the curve shown with the number "III" is calculated as 8.37 Mpa and the elastic modulus value of the adhesive composition given in the curve with the number "IV" is calculated as 9.34 Mpa. As can be clearly seen from the graph given in Figure-1, the adhesive composition (curves III and IV) containing the base material, carbon black, drying agent and surface agent provides an increase in the elasticity modulus value and, therefore, a homogeneous adhesive composition with high mechanical strength and moisture resistance is provided by the related technique.

Table 3.7. Young modulus table of adhesive mixture

	Base material (%)	**Curing agent (%)**	**Cabon black (%)**	**Adhesive promoter (%)**	**Young Modulus (MPa)**
Adhesive Mixture #1	91	9	-	-	2.75
Adhesive Mixture #2	55	5	40	-	3.14
Adhesive Mixture #3	54	5	40	1	8.37
Adhesive Mixture #4	54	5	40	1	9.34

3.3.3. Temperature Characterization of a Fiber Optic Coil

The manufacturing method of a fiber optic coil includes the following processing steps. A spool containing at least one wall and cylindrical mandrel preferably made of metal material such as aluminum (Al), titanium (Ti), stainless steel (SS), is cleaned with alcohol to stick adhesive. An air gap is created between the mandrel and the fiber optic coil with the help of a cylindrical surface. That is temporarily placed by passing through the mandrel between the wall and the cylindrical core. With a thickness of 0.01-3 mm, an adhesive material is filled and preferably on an external spool with a thickness of 0.5-3 mm obtained from fiber and adhesive material is placed and a buffer is obtained. The buffer obtained on the spool is vitrified by keeping it at room temperature for at least 12 hours. with a total length of 1,100 m using polarization maintaining fiber with a diameter of 165 µm, with a quadruple symmetrical winding pattern consisting of sequential and cylindrical 48 layers with 85 turns of fiber. Fiber turns in each layer until the determined length and number of layers on the buffer is wounded. Fiber optic coil is wounded. During the making of a fiber optic coil, the fiber, preferably in each turn, preferably by a dispenser, adhesive unit or a brush, etc. with the help of a homogeneous adhesive material is applied, while the fiber moving from the transfer spools to the winding spool.

The fiber preferably passes through an adhesive reservoir and the entire outer surface of the fiber is coated homogeneously with the adhesive material. The fiber optic coil, the winding process that is completed, is vitrified at 35°C for 20 hours and cured at 70°C for 28 hours. In order to apply the symmetrical winding patterns applied during the winding of fiber optic coil, it is necessary to start from the midpoint of the fiber used. One half of the fiber of the pre-calculated length is divided into the first transfer spool and the other half equal to the second transfer spool. The winding of the fiber optic coil begins in such a way that the middle point of the fiber, which is in two equal lengths and on two separate transfer spools, comes into contact with the fiber optic coil spool. The fiber tours mentioned in the production of the fiber optic coil, starting from the middle point of the fiber, and moving toward its two ends, are placed on the buffer formed on at least one wall of the spool and around the cylindrical surface. It is wound on the outer surface of the created air space. Each fiber layer forming the fiber winding starts from at least one wall of the spool and continues until it reaches the previously calculated number of turns. The strands of fiber wound on the spool for each layer are positioned side by side with an equal number of turns on each layer.

The fiber optic coil contains a buffer layer that reduces the contact between the spool and the fiber optic coil, and this buffer layer consists of two separate layers. In the first layer of the buffer layer, there is an adhesive mixture filled with a thickness of 0.5-0.7 mm between the said wall and the cylindrical core. The second layer placed on top of the first layer is a layer of 2-3 mm thick fiber and adhesive mixture.

In order to reduce the thermal sensitivity of the fiber optic coil, there is an air gap created between the spool and the fiber optic coil. Instead of this air gap, adhesive mixture or gel can also be used.

Figure 3.72. Cross sectional schematic view of the fiber optic coil with adhesive and buffer layer

In the winding process of fiber optic coil, PM fiber with a total length of 1,100 m and a diameter of 165 μm is used. The fiber optic coil (6) produced in the study has a quadrupole winding pattern, which consists of 48 layers with 85 turns on each layer, and preferably contains adhesive mixture in a homogeneous structure with each turn.

Before the curing process, the coil is placed in the climatic chamber, one end of the fiber optic coil is spliced to a test setup that provide a polarized light and the output end of the test fiber is attached to the extinction ratio meter to record the PER value change in the fiber with the changing temperature.

Temperature-dependent rate tests are carried out with an IFOG system that includes a light source, coupler, polarizer, photo- detector, and MIOC provided with a fiber optic coil. IFOG systems used in these tests include four different coils with identical geometry, in which only the adhesive material used changes, provided that all conditions remain the same, and only a fiber optic coils placed in the climatic chamber.

A detection unit includes of a coupler, a photodetector and a polarizer are placed at the output of the ASE light source consisting of 300 mW LD, hybrid component and 10 m Er-doped fiber. IFOG performance measurements of the coil wound with the adhesives characterized in Section 0. The overall view of the Fiber optic coil-MIOC tested in this way is given in Figure 3.73.

(a) (b) (c)

Figure 3.73. The photographs of (a) a fiber optic coil on a spool, (b) MIOC plate with a polarizer and a 1x2 coupler, (c) a combined MIOC and a fiber optic coil.

The specified tests are carried out in the climatic chamber at a heating and cooling rate of 0.5°C/min, in the temperature range of -40°C to +60°C as shown in Figure 3.74.

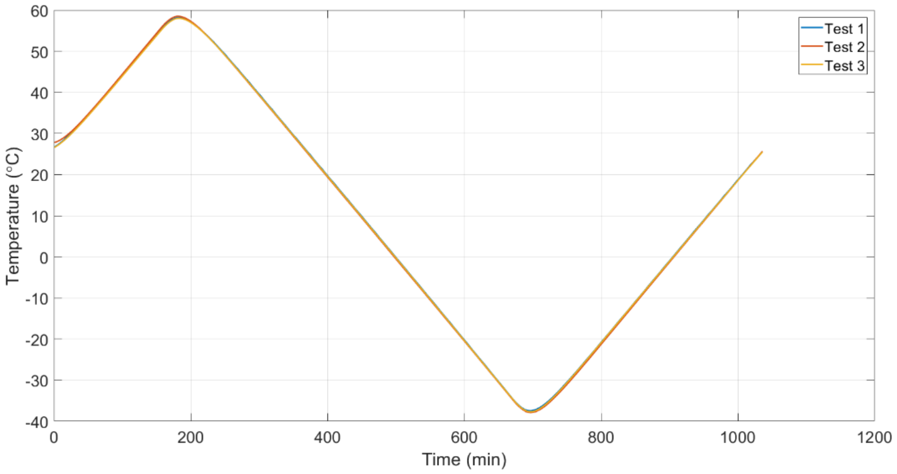

Figure 3.74. Temperature profile approved for the IFOG Performance

After that, this fiber optic coil is integrated with MIOC and the temperature-dependent performance of the system is examined. The temperature-dependent rate performance results for 4 different adhesive compositions are given in Figure 3.75,Figure 3.76, Figure 3.77, and Figure 3.78.

A temperature dependent rate measurement of the IFOG installed with an adhesive-free fiber optic coil is given in Figure 3.75. The fiber optic coil of the IFOG, whose graphic is given here, the fiber is wound without using any adhesive while the calculated turn winding is completed.

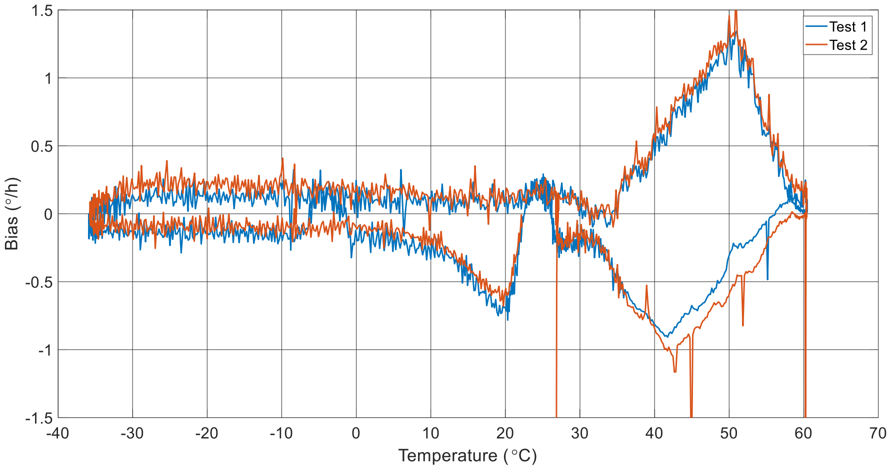

Figure 3.75. Temperature dependent rate performance of the IFOG installed with an adhesive-free fiber optic coil

When the temperature-dependent rate measurement of the fiber optic coil given in this graph is examined, it is seen that random errors that occur as a result of stress under temperature change are evident. Although an inhomogeneous behavior is observed in the behavior of the adhesive-free winding used here under temperature change, there are irregular jumps especially at positive temperatures, and it is clearly observed that the temperature-dependent rotation sensitivity increases at high temperatures. According to the results obtained from the graph here; The rotation sensitivity of the adhesive-free fiber optic winding, for which temperature-dependent rotation measurements are made, is calculated as an average of 3.0 (°/h)/(°C/min) over the entire temperature range. Especially at high temperatures, this value is calculated as approximately 8 (°/h)/(°C/min) and it is clearly observed that the rotation sensitivity of the temperature change is high in the entire temperature range.

An example temperature dependent rate measurement of IFOG built with a fiber optic coil containing silicon as adhesive is given in Figure 3.76. The fiber is wound using a silicone-based adhesive prepared with a mixture of base adhesive and drying agent while the calculated turn of winding is completed to make a fiber optic coil.

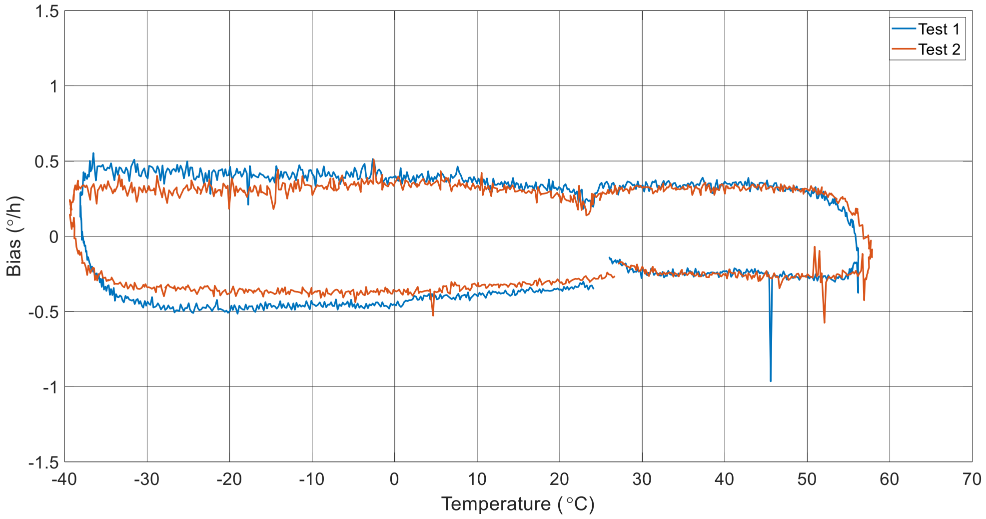

Figure 3.76. Temperature dependent rate performance of the IFOG installed with fiber optic coil wound using a silicone adhesive

When the temperature-dependent rate measurement of the fiber optic coil produced with the base adhesive and drying agent mixture given in this graph is examined, it is clearly seen that there are random errors that occur as a result of stress due to temperature change.

Although an inhomogeneous trend is observed in the behavior of the fiber optic coil containing adhesive, used here under temperature change, there are irregular peaks, especially at negative temperatures. According to the results obtained from the graph here; the rate sensitivity of the fiber optic coil produced with a mixture of base adhesive and drying agent, for which temperature-dependent rate measurements are made, is calculated as an average of 1.85 (°/h)/(°C/min) over the entire temperature range.

Figure 3.77 gives an example temperature dependent rate graphic of IFOG installed with a fiber optic winding containing carbon black and silicon as the adhesive. During the winding of the fiber optic coil of the IFOG graphed here, each fiber turn is wound using a silicone-based adhesive prepared with a mixture of base adhesive, drying agent and carbon black.

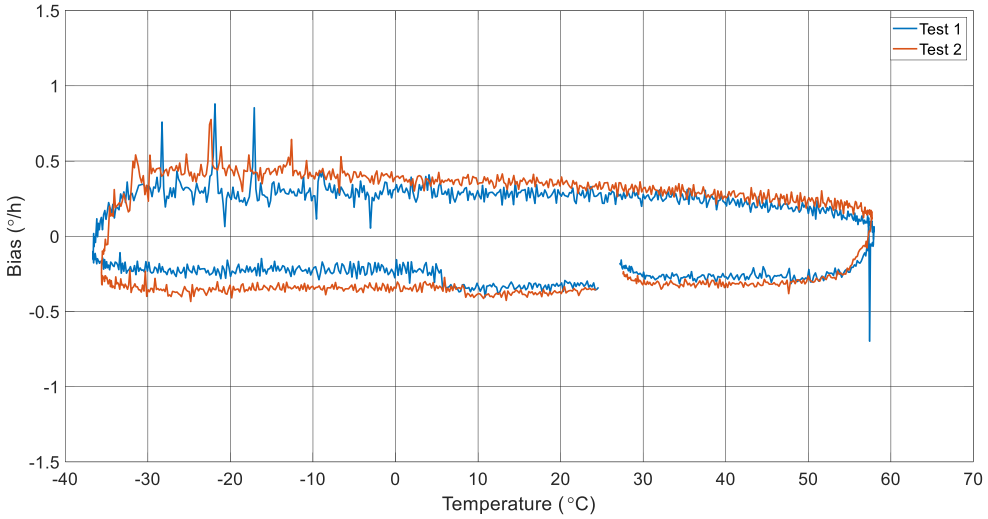

Figure 3.77. Temperature dependent rate performance of the IFOG installed with fiber optic coil wound using a silicone adhesive prepared with a mixture of base adhesive, drying agent and carbon black

When the temperature-dependent rate measurement of the fiber optic winding produced with the mixture of base adhesive, drying agent and carbon black given in the graph in Figure 3.77 is examined, it is seen that random errors occur as a result of stress under temperature change. Although the behavior of the adhesive-containing fiber optic coil used here is homogeneous under temperature change, it is clearly seen that the temperature-dependent rate change also behaves differently if the temperature is increasing or decreasing. According to the results obtained from the graph here, the rotation sensitivity of the fiber optic coil produced with a mixture of base adhesive, drying agent, and carbon black, for which temperature-dependent rate measurements are made, is calculated as an average of 1.39 (°/h)/(°C/min) over the entire temperature range, depending on the temperature change.

An example temperature dependent rate graphic of IFOG installed with fiber optic coil containing adhesive material is given in Figure 3.78. During the winding of the fiber optic coil of the IFOG graphed here, each fiber turn is wound using an adhesive material prepared with a mixture of base adhesive, drying agent, carbon black, and surface agent.

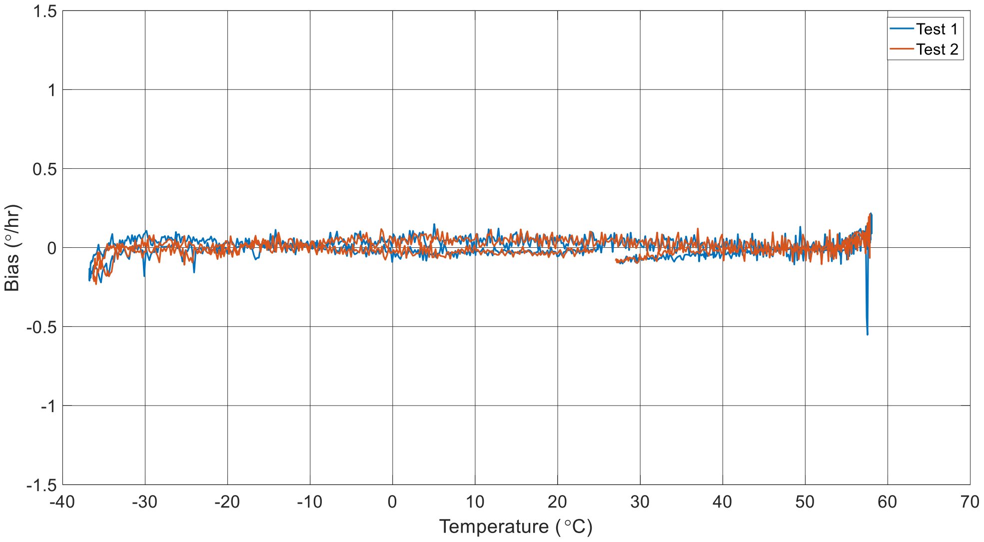

Figure 3.78. Temperature dependent bias performance of the IFOG installed with fiber optic coil wound using a silicone adhesive prepared with a mixture of base adhesive, drying agent, carbon black and surface agent.

When the temperature-dependent rate measurement of the fiber optic coil produced with the adhesive material given in the graph in Figure 3.78 is examined, it is seen that the bias errors that occur as a result of the stress under the temperature change and the results of the fiber optic coil are significantly reduced compared to the fiber optic coils whose results are given in Figure 3.75, Figure 3.76 and Figure 3.77. Although a homogeneous behavior is observed in the behavior of the fiber optic coil containing the adhesive material used here under temperature change, it is clearly seen that the temperature-dependent rotation change is not affected even if the temperature is in the increasing or decreasing direction.

According to the results obtained from the graph here, the rate sensitivity of the fiber optic coil, which contains an adhesive material with high mechanical strength, for which temperature-dependent rate measurements are made, is calculated as an average of 0.16 (°/h)/(°C/min) over the entire temperature range. Since the fiber optic coil contains an adhesive material with high mechanical strength, the spin sensitivity resulting from mechanical stress against temperature change is at least 10 times greater than the results of fiber optic coil produced with a mixture of base adhesive and drying agent, with the results of fiber optic coil without any adhesive. It is clearly observed that it has improved at least 18 times compared with the other design.

As a result, 4 different fiber optic coils have different adhesive mixture that is wound in a quadrupole winding pattern at low tension with a 1100m length of PM fiber. The coils are featured as a function of temperature with respect to rate and the results are shown in Table 3.8. This study suggests that one coil can obtain a higher performance over a large temperature range by using accurate adhesive mixture is shown in Figure 3.78.

Table 3.8. Bias error of Fiber optic coils with different adhesive mixtures

# of Coil	Adhesive	Bias Error (°/h)/(°C/min)
Coil #1	-	3.01
Coil #2	Adhesive Mixture #1	1.85
Coil #3	Adhesive Mixture #2	1.39
Coil #4	Adhesive Mixture #4	0.16

4 NOVEL METHOD: A FIBER OPTIC GYROSCOPE FOR THE SUPPRESSION OF A FARADAY EFFECT-INDUCED BIAS ERROR

In this chapter, a new, to the best of our knowledge, a fiber optic coil design is proposed to reduce magnetic field sensitivity without adding any optical components or electronic algorithms to the IFOG system. It is shown that this design can be applied without disturbing the simplest IFOG structure. Considering the fact that the magnetic field has an invertible effect on polarization, the compensation of the Faraday-effect-induced bias error has been demonstrated theoretically and experimentally by allowing two different polarizations to travel inside the fiber optic coil.

4.1. Technical Research

Among the undesired effects, phase drift that is caused by a magnetic field results in a Faraday Effect induced bias error in IFOGs [74]. This is due to the phase drift of the counterpropagating light pass-through of the fiber optic coil. This phase drift that will generate in the presence of a radial magnetic field is related to PNR errors in the fiber of fiber optic coil [75].

The Faraday effect is not the principal error source of axial magnetic field drift [66]. In general, the drift caused by the axial direction unable to take the advantage of optical compensation [76]. In other words, the Faraday Effect induced bias error is directly related to the phase drift caused by PNR errors in the fiber optic coil. The Faraday Effect induced bias error of IFOG can be suppressed by using a magnetic shield case with highly permeable metal [77] and photonic crystal fiber (PCF) based fiber-optic coil [78].

In addition to the above-mentioned suppression methods, optical compensation methods are proposed for PNR error control in IFOGs. Pan Liu et al. have shown that the two orthogonal polarizations have opposite polarities and suppress the Faraday Effect induced phase drift effectively by using a dual-polarization IFOG with the polarization beam coupler (PBC) method [79]. Yanru Zhou et al. have shown a new optical method for suppressing the radial magnetic effect by inserting a single-mode (SM) suppressing section fiber between depolarizer and fiber optic coil [80]. Although these methods effectively decrease the magnetic errors, using new sections that violate the minimum scheme for IFOG brings new drawbacks such as complexity in design and high cost.

In this section of the present thesis, a new optical compensation method called Inverse Symmetric Polarization Interferometric Fiber-Optic Gyroscope (ISP-IFOG) is presented and the proposed method keeps the simplest IFOG structure. It is shown by theoretical analysis that two orthogonal polarities caused by the Faraday Effect are effectively suppressed by the proposed method and the experimental results are in good agreement with the theoretical analysis.

4.2. Theorical Analysis

The Faraday effect is only valid when there is a twist which is inevitable in practice while the process of drawing the fiber and winding the PM-fiber around the spool [81]. Therefore, as shown Figure 4.1 dz is the micro unit to show the random twist. Then the basic Equation of input and output electrical field E, under magnetic field is given by [61]

$$\begin{bmatrix} \hat{E}_x \\ \hat{E}_y \end{bmatrix} = exp(-j\beta_{av}z)C(\phi,\zeta)\begin{bmatrix} \hat{E}_x \\ \hat{E}_y \end{bmatrix} \tag{4.1}$$

$$C(\phi,\zeta) = \begin{bmatrix} C_{11} & C_{12} \\ C_{21} & C_{22} \end{bmatrix} \tag{4.2}$$

where

$$C_{11} = C_{22}^{*} = \cos\eta z - j\frac{\Delta\beta}{2\eta}\sin\eta z \tag{4.3}$$

$$C_{12} = -C_{21} = \frac{\phi-\zeta}{\eta}\sin\eta z \tag{4.4}$$

$$\beta_{av} = \frac{\beta_x+\beta_y}{2} \tag{4.5}$$

$$\eta = \sqrt{(\frac{\Delta\beta}{2})^2 + (\phi-\zeta)^2} \tag{4.6}$$

The birefringence, the twist and the Faraday rotation per unit length are represented by $\Delta\beta$, ϕ, ζ, respectively [82]. H and V can be change with temperature variations, and these two main parameters assumed as a constant in these calculations. When $\Delta\beta >> \phi$ and ζ converged to

$$C(\phi,\zeta) = F(\phi,\zeta) + G(\phi,\zeta) \tag{4.7}$$

where

$$F(\phi,\zeta) = \begin{bmatrix} \cos\eta z - j\sin\eta z & 0 \\ 0 & \cos\eta z + j\sin\eta z \end{bmatrix} \tag{4.8}$$

$$G = \begin{bmatrix} g_1 & 1 \\ -1 & g_1^* \end{bmatrix} \cdot g_2 sin\eta z \tag{4.9}$$

$$g_1 = j\frac{\phi - \zeta}{\eta + \Delta\beta/2} \tag{4.10}$$

$$g_2 = \frac{\phi - \zeta}{\eta} \tag{4.11}$$

The total transfer matrix of fiber spool for each section can be expressed by

$$S = C_n C_{n-1} \ldots C_1 = (F_n + G_n)(F_{n-1} + G_{n-1}) \ldots (F_1 + G_1) \tag{4.12}$$

To ensure that each section is short enough, the fiber can be divided

$$\eta_k z_k = 2\pi \quad \text{where} \quad k = 1,2,\ldots.,n-1 \tag{4.13}$$

$$z_k = \frac{2\pi}{\eta_k} \simeq 2\frac{2\pi}{\Delta\beta}. \tag{4.14}$$

By using this condition, the transfer matrix S can be written as a unit matrix.

$$S = (F_n + G_n)\begin{bmatrix} \exp(-j \cdot 2(n-1)\pi) & 0 \\ 0 & \exp(j \cdot 2(n-1)\pi) \end{bmatrix} \tag{4.15}$$

Applying Equation 15 the cw and ccw light can be written as

$$S_{cw} = (F_{cw_n} + G_{cw_n})\begin{bmatrix}\exp(-j\cdot 2(n-1)\pi) & 0 \\ 0 & \exp(j\cdot 2(n-1)\pi)\end{bmatrix} \quad 4.16$$

$$S_{ccw} = (F_{ccw_1} + G_{ccw_1})\begin{bmatrix}\exp(-j\cdot 2(n-1)\pi) & 0 \\ 0 & \exp(j\cdot 2(n-1)\pi)\end{bmatrix} \quad 4.17$$

where

$$\eta_{cw_k} = \sqrt{(\frac{\Delta\beta}{2})^2 - (\phi_{cw_k} - \zeta_{cw_k})^2} \quad 4.18$$

$$\eta_{ccw_k} = \sqrt{(\frac{\Delta\beta}{2})^2 + (\phi_{ccw_k} + \zeta_{ccw_k})^2} \quad 4.19$$

Ideally, the polarizer element has an infinite extinction ratio such that only $(1,1)$ elements of S_{cw_n,ccw_n} can be considered. Additionally, when $\eta \simeq \Delta\beta >> \phi$ and ζ assumed then $(1,1)$ elements of G_{cw_n,ccw_n} can be neglected due to low impact of the second order [61]. Therefore, the light equation of cw and ccw becomes

$$S_{cw} = F_{cw_n}\exp(-j\cdot 2(n-1)\pi) \quad \text{and} \quad S_{ccw} = F_{ccw_1}\exp(-j\cdot 2(n-1)\pi) \quad 4.20$$

By using Equation 13, the phase difference is given by

$$\begin{aligned}\Delta\psi &= \sum_{k=1}^{n} (\eta_{cw_k} z_{cw_k} - \eta_{ccw_k} z_{ccw_k}) = \int_0^L (\eta_{cw} - \eta_{ccw})\,\mathrm{d}z \\ &= \int_0^L (\frac{4\phi\zeta}{\eta_{cw} + \eta_{ccw}})\,\mathrm{d}z\end{aligned} \quad 4.21$$

where z_{cw_k}, and z_{cw_k} are too small, and L is the total length of the fiber, and ϕ, ζ, η_{cw}, and η_{ccw} depend on function of z. Since $\eta_{cw,ccw} \simeq \Delta\beta/2$ the Equation 21 becomes

$$\Delta\psi = \int_0^L (\frac{4\phi\zeta}{\Delta\beta})\,\mathrm{d}z \quad \text{where} \quad \zeta = \zeta_0 sin(\frac{z}{r} - \theta_0) \quad 4.22$$

ζ_0 is the Faraday rotation per unit length along the fiber depends on magnetic field H_0 and radius of fiber loop r. Then the bias can be rewritten as

$$\Delta\psi = \frac{4\zeta_0}{\Delta\beta}\int_0^L \phi(z) \cdot \sin(\frac{z}{r} - \theta_0)\mathrm{dz} \tag{4.23}$$

Rewriting as $\theta = z/r$, $dz = rd\theta$, and $L = 2m\pi r$ (m = turn number),

$$\Delta\psi = \frac{4\zeta_0 r}{\Delta\beta}\int_0^{2m\pi} \phi(\theta) \cdot \sin(\theta - \theta_0)\mathrm{d}\theta = \frac{4\zeta_0 r}{\Delta\beta}(a\cos\theta_0 - b\sin\theta_0) \tag{4.24}$$

where

$$a = \int_0^{2m\pi} \phi(\theta) \cdot \sin(\theta)\mathrm{d}\theta \tag{4.25}$$

$$b = \int_0^{2m\pi} \phi(\theta) \cdot \cos(\theta)\mathrm{d}\theta \tag{4.26}$$

by using $\xi = \tan^{-1}(b/a)$, Equation 24 becomes

$$\Delta\psi = \frac{4\zeta_0 r}{\Delta\beta} \cdot \sqrt{a^2 + b^2} \cdot \cos(\theta_0 + \xi) = \frac{4\zeta_0 r}{\Delta\beta} \cdot \sqrt{|\Phi|} \cdot \cos(\theta_0 + \xi) \tag{4.27}$$

where

$$\Phi = \int_0^{2m\pi} \phi(\theta) \cdot \exp(-j\theta)\mathrm{d}\theta \tag{4.28}$$

[Φ] is the energy spectrum component of the twist period and coincides with one turn of the loop. If m is large enough then

$$W = \frac{|\Phi|^2}{2m\pi} \tag{4.29}$$

By using Equations 4.28 and 4.29, then bias becomes

$$\Delta\psi = \frac{4\zeta_0 r}{\Delta\beta} \cdot \sqrt{2m\pi W} \cdot \cos(\theta_0 + \xi) \qquad 4.30$$

cosine term can take any value between [-1, 1] when the magnetic field direction changes. These values can be regarded as drift and expressed as drift δ,

$$\delta = \frac{8\zeta_0 r}{\Delta\beta} \cdot \sqrt{2m\pi W} \qquad 4.31$$

or

$$\delta = \frac{8\zeta_0 r}{\Delta\beta} \cdot \sqrt{2AW} \qquad 4.32$$

where A is the area of the fiber loop and W is the twist power spectrum.

By using the phenomena that the drift caused by the Faraday effect in the fast and slow axes of PM fiber has opposite polarities [66]. Therefore, the overall drift caused by the Faraday effect as described in Eq. 4.32 can be eliminated when the whole path of two polarizations is balanced.

Presented ISP-IFOG configuration as shown in Fig. 1(a) ensures that s and p polarizations can travel through the fiber optic coil simultaneously. To get two orthogonal polarization to run symmetrically inside the fiber optic coil, we need a 90°splice in the middle of the fiber of that used coil as shown in Figure 4.1.

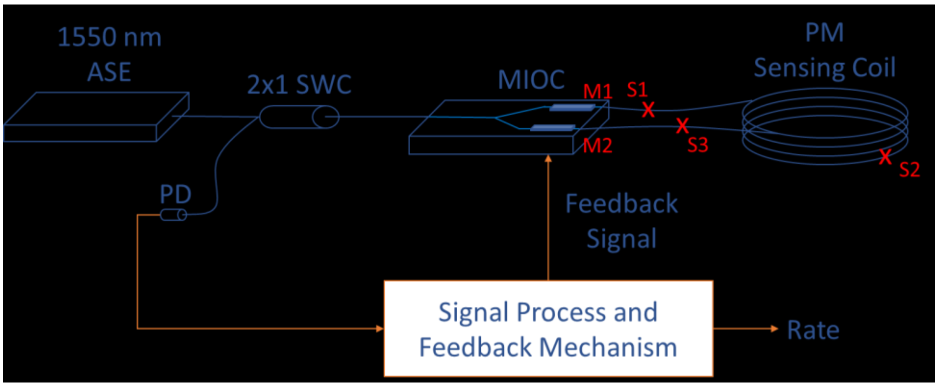

Figure 4.1. Optical configuration of ISP-IFOG

By using this effect, it is aimed to absorb the external magnetic field inside the coil as a result of the light interfering in the fiber optic coil moving in the same way in fast and slow axes. In this configuration, unlike a simple IFOG structure, a reverse symmetrical polarization effect is created in the coil.

As the two orthogonal polarizations run symmetrically inside the fiber optic coil, we need a 90° splice in the middle of the fiber of that used coil to propagate the two orthogonal polarization simultaneously, S1 and S3 must be cross splicing such as 0° and 90° or vice versa. Moreover, we need a 90° splice to provide the two orthogonal polarization to run symmetrically inside the fiber optic coil and allow CW and CCW lights to pass through the MIOC again. This 90° splice (S2) is intentionally selected at the midpoint of the PM fiber optic coil as shown in Figure 4.2 to be sure that the total amount of time for s and p polarization on the CW and CCW path will be identical. Therefore, two orthogonal polarizations are induced by two different signs and the same magnitude of bias shifting due to the magnetic field effect.

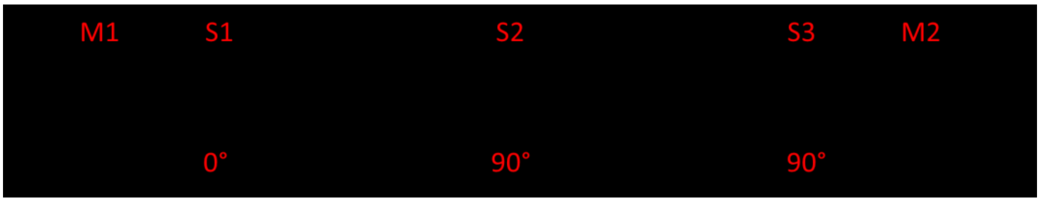

Figure 4.2. Light path of fiber optic coil in ISP-IFOG configuration

The transfer matrix S can be written as a combination of fiber sections between the connection points (M1, S1, S2, S3, M2) as shown in Figure 4.1 and Figure 4.2, and the unit matrix becomes

$$\mathrm{S} = \mathrm{S}_1 + \mathrm{S}_2 + \mathrm{S}_3 + \mathrm{S}_4 \qquad 4.33$$

where

$$S_{cw_n} = S_{cw_{n_1}} + S_{cw_{n_2}} + S_{cw_{n_3}} + S_{cw_{n_4}}, \qquad 4.34$$

$$n = n\_1 + n\_2 + n\_3 + n\_4 \qquad 4.35$$

$$S_{cw} = \left(F_{n_1} + G_{n_1}\right)U(n_1)R(\alpha_1)\left(F_{n_2} + G_{n_2}\right)U(n_2)R(\alpha_2) \left(F_{n_3} + G_{n_3}\right)U(n_3)R(\alpha_3)\left(F_{n_4} + G_{n_4}\right)U(n_4) \quad 4.36$$

$$S_{ccw} = \left(F_{n_4} + G_{n_4}\right)U(n_4)R(\alpha_3)\left(F_{n_3} + G_{n_3}\right)U(n_3)R(\alpha_2) \left(F_{n_2} + G_{n_2}\right)U(n_2)R(\alpha_1)\left(F_{n_1} + G_{n_1}\right)U(n_1) \quad 4.37$$

$$\mathrm{U(n)} = \begin{bmatrix} \exp(-\mathrm{j}\cdot 2(\mathrm{n}-1)\pi) & 0 \\ 0 & \exp(\mathrm{j}\cdot 2(\mathrm{n}-1)\pi) \end{bmatrix} \quad 4.38$$

$$\mathrm{R}(\alpha) = \begin{bmatrix} cos\alpha & -sin\alpha \\ \sin\alpha & cos\alpha \end{bmatrix} \quad 4.39$$

R(α) is used to represent the degree of splice points that is shown in Figure 4.2. In ISP-IFOG, the configuration 0-90-90° angle of the splice is used for α_1, α_2, and α_3, respectively. In addition to that, the polarizer element of MIOC has an infinite extinction ratio such that only (1,1) elements of S_{cw_n}, S_{ccw_n} can be considered. In addition, when $\eta\,\Delta\beta \gg \phi$ and $\eta\,\Delta\beta \gg \zeta$ are assumed, then (1,1) elements of G_{cw_n} and G_{ccw_n} can be neglected due to low impact of the second order [83]. Therefore, the phase difference is given by Equations 4.40 and 4.41,

$$\Delta\psi = \int_0^{l_1+l_2} (\eta_{cw} - \eta_{ccw})\mathrm{d}\,z = \int_0^{l_1+l_2} \left(\frac{4\phi\zeta}{\eta_{cw} + \eta_{ccw}}\right) \mathrm{d}z \quad 4.40$$

$l_1 + l_4$ is the total length of the MIOC pigtail fibers, and ϕ, ζ, η_{cw}, and η_{ccw} depend on z. This phase difference can be expressed as drift δ,

$$\delta = \frac{8\zeta_0 r}{\Delta\beta}\cdot\sqrt{2m\pi W} \quad , \quad m = \frac{l_1 + l_4}{2\pi r} \quad 4.41$$

When the fiber segments of fiber optic coil l_2 and l_3 have equal length, it has been shown that the derivation of phase drift is totally suppressed in the fiber optic coil, where W power spectrum of the twist. Although the phase drift is dependent on both the fiber length of the fiber optic coil and the fiber length of the MIOC pigtail in IFOG configuration, the Faraday Effect induced bias error is dependent on only fiber length of the MIOC pigtails l_1 and l_4 in ISP-IFOG configuration. In addition, the bias can be linearly reduced to zero while fiber length of the MIOC pigtails l_1 and l_4 are shorten enough.

When S1, S2, and S3 are 0°, s-polarization mode propagates in the fiber optic coil, while S1 and S3 are 90°, and S2 is 0°, p-polarization mode propagates in the fiber optic coil. To propagate the two orthogonal polarizations simultaneously, S1 and S3 must be cross splicing such as 0° and 90° or vice versa. In addition, we need a 90° splice both to provide the two orthogonal polarizations to run symmetrically inside the fiber optic coil and allow CW and CCW lights to pass through the MIOC again. This 90° splice (S2) is intentionally selected at the midpoint of PM fiber optic coil as shown in Figure 4.2 to be sure that the total amount of time for s and p polarization on the CW and CCW path will be identical. Therefore, two orthogonal polarizations are induced by two different signs and the same magnitude of bias shifting due to the magnetic field effect. As a result of this, the polarization nonreciprocity (PNR) errors in PM fiber optic fiber optic coil are canceled.

4.3. Advanced Modeling

The Faraday Effect induced bias error is calculated numerically by Matlab using Eq. 4.41 for IFOG and ISP-IFOG with the MIOC pigtail fiber length 1.5 m and the fiber optic coil fiber length 1100 m.

The radius of the fiber optic coil is 42.5 mm and the fiber optic coil has 48 layers of fiber with 80 turns in each layer. To model the Faraday Effect induced bias error, there is a 80x48 turn for the 1100 m length of fiber optic coil and 80x48/330 turn calculated for the 1.5 m length of MIOC pigtail fiber.

In the calculations of our model, the twist power spectrum of fiber optic coil is defined as comparable with experimental results of 0.29 mT for IFOG. The value of twist power spectrum is defined as a constant value of 150 $\mathrm{rad}^2/\mathrm{m}^2$. A short Matlab code is generated for the simulate of the bias error for the IFOG and the ISP-IFOG configuration as described in Chapter 4.

The Faraday Effect induced bias error of the traditional IFOG configuration with slow axis polarization is calculated for seven magnetic field value of different intensities. According to the results is given in the Figure 4.3, the bias erro is increase linearly with applied magnetic field intensity increased for s-polarization in the traditional IFOG. Based on these experimental results, the bias error of IFOG is calculated as 9.58 °/h/mT for slow axis polarization.

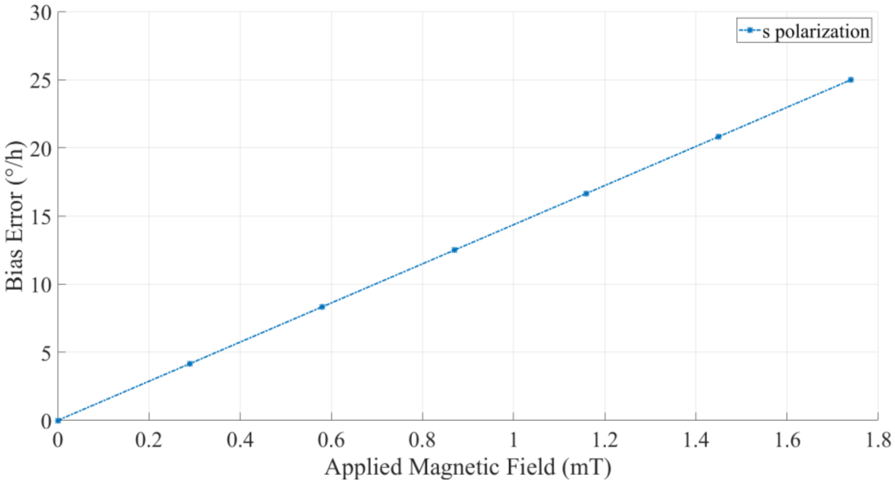

Figure 4.3. Simulation results of the slow polarity axes of an IFOG calculated for the different magnetic field intensities.

The Faraday Effect induced bias error of the traditional IFOG configuration with fast axis polarization is also calculated for seven magnetic field value of different intensities.

According to the results is given in the Figure 4.4, the bias error is decreased linearly with applied magnetic field intensity increased for p-polarization in the traditional IFOG. Based on these experimental results, the bias error of IFOG is calculated as -9.64 °/h/mT for fast axis polarization.

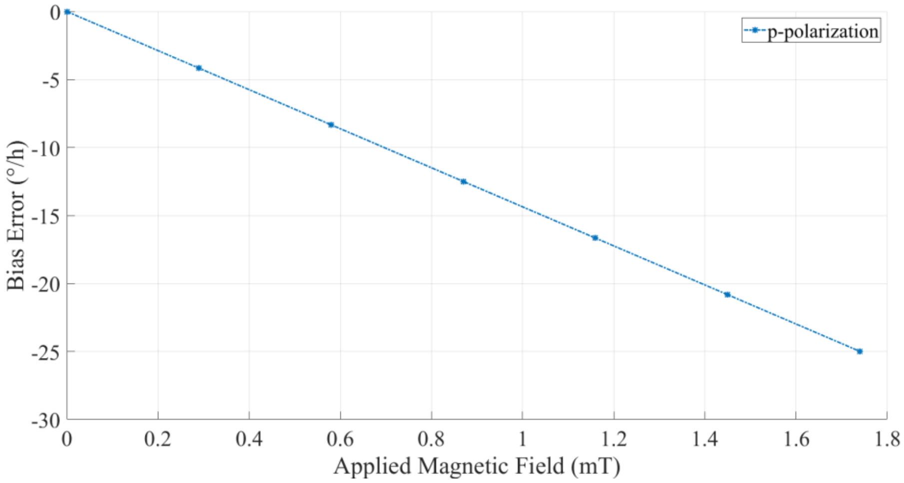

Figure 4.4. Simulation results of the fast polarity axes of an IFOG calculated for the different magnetic field intensities.

The Faraday Effect induced bias error of the ISP-IFOG configuration with the + x direction of magnetic field is calculated for seven magnetic field value of different intensities. According to the results given in Figure 4.5, the bias error is increased linearly with applied magnetic field intensity increased for the ISP-IFOG when magnetic field is applied in the +x direction. Based on these experimental results, the bias error of the ISP- IFOG is calculated as 0.47 °/h/mT for the +x direction of a magnetic field.

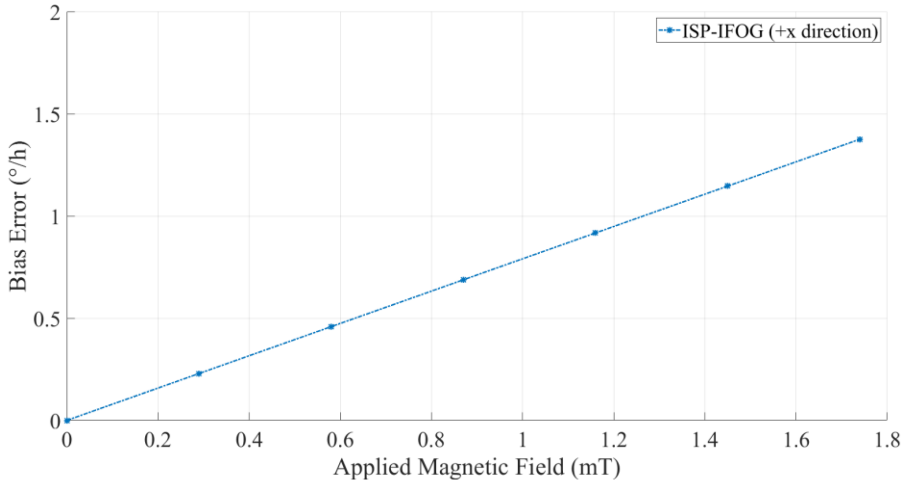

Figure 4.5. Simulation results of the + x direction of the ISP-IFOG calculated for the different magnetic field intensities.

The Faraday Effect induced bias error of the ISP-IFOG configuration with - x direction of magnetic field is also calculated for seven magnetic field value of different intensities. According to the results given in Figure 4.6, the bias error is decrease linearly with applied magnetic field intensity increased for the ISP-IFOG when magnetic field is applied in -x direction. Based on these experimental results, the bias error of the ISP- IFOG is calculated as 0.47 °/h/mT for the -x direction of a magnetic field.

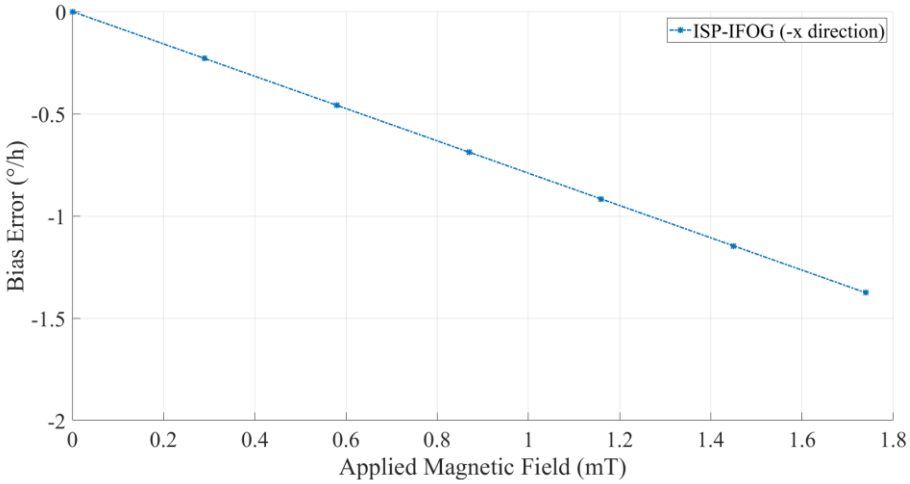

Figure 4.6. Simulation results of the - x direction of the ISP-IFOG calculated for the different magnetic field intensities

The simulation results for the different magnetic field intensities of the two orthogonal polarity axes of IFOG and ISP-IFOG are compared and the results are given in the Figure 4.7.

It can be clearly seen that the bias error of the gyroscope under a magnetic field can be reduced considerably with ISP-IFOG design, theoretically. Due to the fact that the slow and fast polarization axes under the magnetic field have an inverse polarization, the Faraday Effect can be greatly reduced when both the slow and fast axes that travel in the fiber optic coil are equal. According to the theoretical results, more than 20 times lower from 9.61 °/h/mT to 0.47 °/h/mT magnetic field sensitivity is obtained in the radial direction.

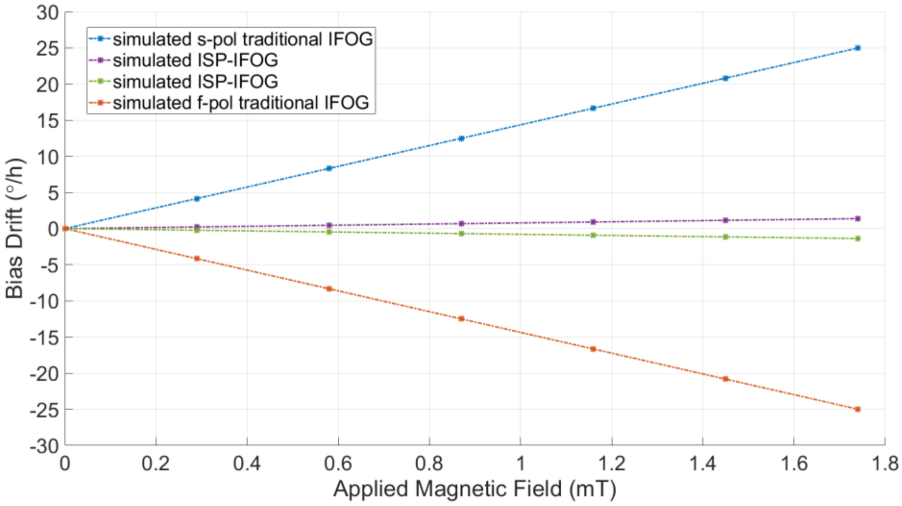

Figure 4.7. Simulation results of the two orthogonal polarity axes of IFOG and ISP-IFOG recorded for the different magnetic field intensities.

4.4. Experimental Results

The fiber optic coil with 77.0 mm inner diameter and 12.5 mm thickness is produced on a 2.7 mm thickness passive PM fiber and adhesive with a Shore-A class special silicone adhesive.

Figure 4.8. Free standing fiber optic coil

The fiber optic coil that was produced on the spool, is separated from the spool and became a free-standing fiber optic coil. The photograph of this coil is shown in Figure 4.8, and the properties of the coil according to the design are given in Table 4.1.

Table 4.1. Fiber optic coil

Length	1116 m
Effective diameter	85.3 mm
Width	12.5 mm
Total # of turn	3840
Type of PM Fiber	Panda
Fiber coating diameter	165 µm
Adhesive	Silicone (Shore A)

As shown in Figure 4.1, to eliminate the interference errors due to splice angle errors, back reflections, and poor quality of polarization maintaining optical components, a broadband ASE light source that has a central wavelength at 1550 nm is used as it used and coupled to a-3 dB optical coupler. Phase modulation is given by a MIOC fabricated by the APE method that has functioned as a > 40 dB polarizer, a 3 dB coupler, and a phase modulator. PM Fiber with 80 µm cladding and 165 µm coating diameter is chosen to wound around average in an 85 mm diameter spool to make the fiber optic coil. A fiber optic coil formed with a quadruple winding pattern of 1100 m length consist of PM-Panda fiber is made up of 48 layers of fiber with a quadrupole winding pattern. A photodetector is implemented to detect the interfered signal that comes from the fiber optic coil. A closed-loop modulation technique is used for the rate measurement to increase the stability and linearity of the scale factor. The most important feature of ISP-IFOG that makes it more competent than IFOG is the splice point in the middle of the fiber optic coil that provides two orthogonal polarizations to travel into the fiber optic coil simultaneously.

The ISP-IFOG scheme planned to be implemented for this is as shown in Figure 16. Here, M1 and M2 are MIOC pigtail points, S1-S2 and S3 points are fiber splicing points, the path of the light between these points passes through the M1-S1-S2-S3-M2 points in the clockwise direction, respectively, in the counterclockwise direction M2-S3- It passes through the points S2-S1-M1. Accordingly, the light moving clockwise and counterclockwise will be exposed to equal effect between the MIOC-Fiber optic coil and the total effect is expected to damp each other under the external magnetic field.

In an IFOG, light from one orthogonal polarization of slow and fast axis (s or p polarization) propagates in a PM fiber optic coil. Unlike IFOG, in ISP-IFOG , it is aimed to have two orthogonal polarizations of light, s and p, propagate in the PM fiber optic coil, simultaneously. M1 and M2 points in Figure 4.1, which are the outputs of the MIOC, have s-polarization around 40 dB, and S1, S2, and S3 indicators show the splice points. By changing the splice degree of the points indicated as S1, S2, and S3 in Figure 4.1, the design has the potential to simultaneously provide two orthogonal polarizations of light to propagate in the PM fiber optic coil.

As shown Figure 4.2 polarized light propagating in CW direction passes through M1, S1, S2, S3, and M1, respectively, while light propagating in the CCW direction passes through M1, S3, S2, S1 and M2, respectively. It is clearly seen in Figure 4.2 that the MIOC pigtail fiber segments are identified as l_1 , l_4 The fiber segments of fiber optic coil identified as l_2 , l_3 which have a splice point S2 between two fiber segments have the same length.

When the splice points S1, S2, and S3 are at a 0° splice angle, s-polarization mode propagates in the fiber optic coil, while the splice points S1 and S3 are at a 90° and S2 is at a 0° splice angle, p-polarization mode propagates in the fiber optic coil as in the fiber optic coil of IFOG.

It can also be thought that these splice points angle error could cause an additional drift. It is briefly desribed by Hotate that the drift caused by the Faraday Effect is not enhanced by any misalignment of the polarization axes but just the intensity of the optical power changes measured by the photo-detector [83]. By using a broadband light source, the coherence length is reduced as much as possible and interference between residual signals and main signals is prevented [1]. Besides, the polarization error effects in the opposite axis are eliminated by the MIOC with a high polarization value [1].

The Helmholtz coil, which is made up of copper wire, is used to provide uniform magnetic field as shown in Figure 4.9. The fiber optic coil is placed in the center of the Helmholtz coil and the magnetic field direction is adjusted parallel to the sensitivity axis of the fiber optic coil. The magnitude of the magnetic field can be controlled by a DC power supply that is altered between + 1.75 mT and - 1.75 mT.

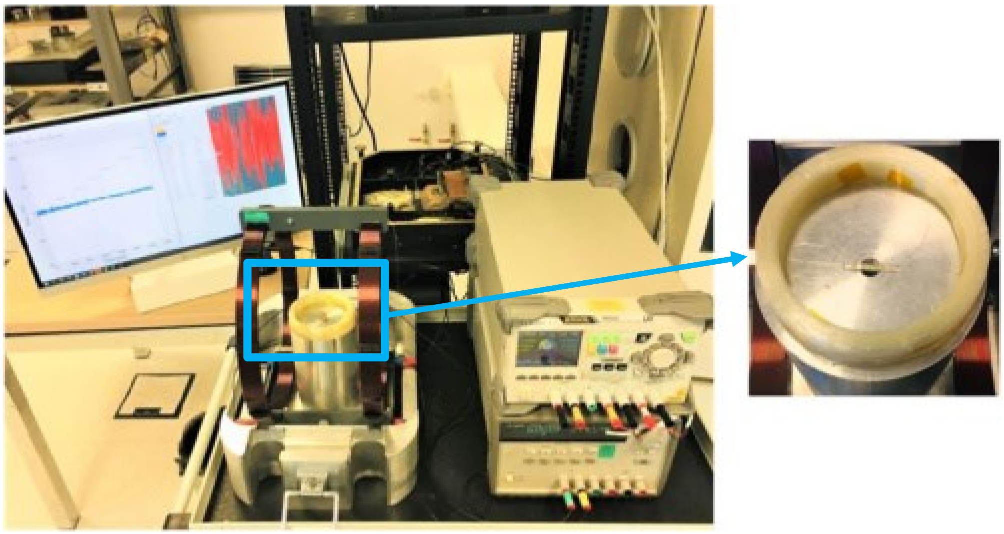

Figure 4.9. Experimental measurement setup for fiber optic coil and MIOC under a radial magnetic field.

In the experimental measurement set-up for IFOG, two orthogonal polarities (slow and fast axes) of light traveling in a fiber optic coil are individually measured. The radial magnetic field is varied from 0 to 1.75 mT by 0.29 mT steps and it is observed that the phase drift of two orthogonal polarization gives the same magnitude bias error with different signs. Sensitivity to a temperature change called a Shupe error has been eliminated by performing a measurement under constant room temperature. Before the experimental analysis of the Faraday Effect induced bias error, it is confirmed that this configuration had a small bias error by testing the IFOG and ISP-IFOG in a static environment without an external magnetic field. And it is confirmed that additional splice point at the middle of the coil had not cause zero drift. According to the results, the bias of IFOG and ISP-IFOG are measured 9.6 (°/h) and 9.8 (°/h), respectively in Nanotechnology Research Center (NANOTAM). Power and polarization measurements are done after each splice point in this configuration and it is measured that there isn’t additional splice loss. Using the measurement results of bias drift, the bias error around zero is calculated for the IFOG and ISP-IFOG.

To measure Faraday Effect induced bias error, seven measurements are made for each configuration by applying seven different magnetic fields of different intensities each with a period of 180 seconds.

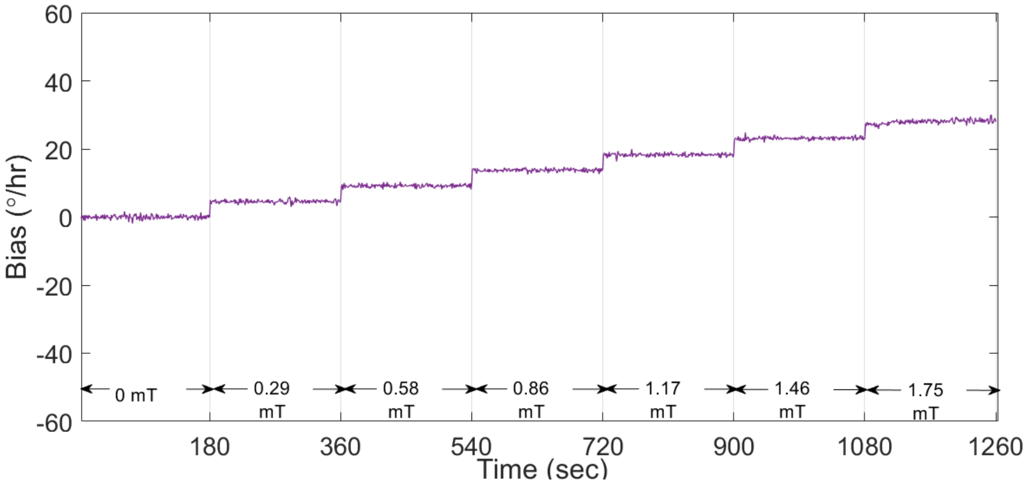

Figure 4.10. Magnetic Field induced bias error in slow axis (s-pol)

For the magnetic field set up, under the radial magnetic field, the rotation error measurements related to the magnetic field related to the polarization of the fiber optic coil in the slow axis are made, and it is observed that the rotation error increased with the increasing magnetic field (Figure 4.10). Similarly, under the radial magnetic field, rotation error measurements due to the magnetic field related to the polarization of the fiber optic coil in the fast axis are made, and it is observed that the rotation error increased in the reversible direction with the increasing magnetic field (Figure 4.11).

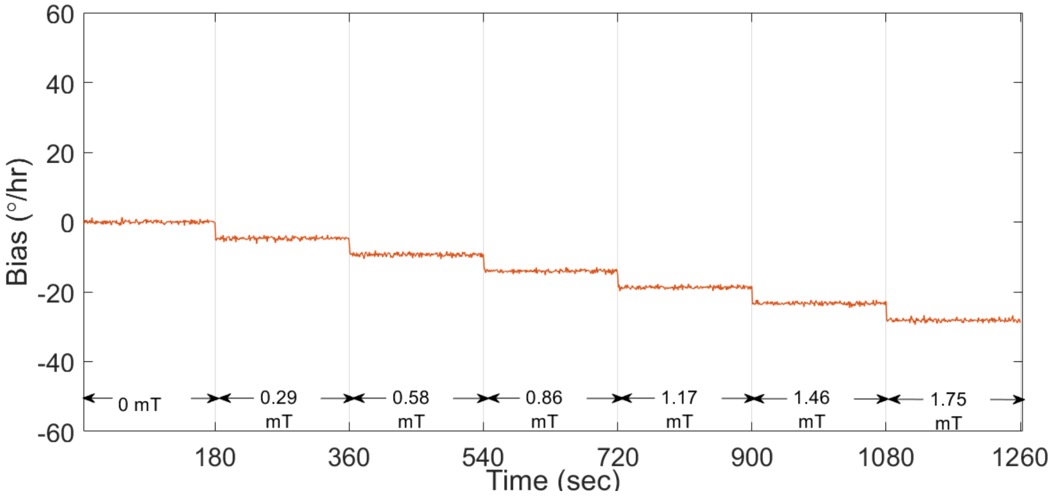

Figure 4.11. Magnetic Field induced bias error in the fast axis (p-pol)

According to the experimental results given in Figure 4.10 and Figure 4.11 the bias error (°/h) increases linearly by the magnetic field intensity. Based on these experimental results, the bias error of IFOG is calculated as 9.58 °/h/mT and -9.64 °/h/mT for slow axis and fast axis polarization, respectively. It should be noted that, in IFOG configuration, the magnitude of the bias error is almost the same with different signs for two orthogonal polarizations. The data obtained as a result of the measurements made are given in Table 4.2.

Table 4.2. Magnetic Field induced bias error in different polarization axes

Voltage (V)	Magnetic Field (mT)	Bias s-pol (°/h)	Bias f-pol (°/h)
0	0	0	0
1	0.29	4.7	-4.5
2	0.58	9.5	-9.6
3	0.86	14	-14.2
4	1.17	18.5	-19
5	1.46	23	-23.2
6	1.75	27.5	-27.8

The same measurement set-up is used to measure the bias error of ISP-IFOG with the same magnetic field intensities. The degree of splicing angle is rotating from 0°-90°-90° for the points S1, S2, S3 Figure 4.1, respectively.

The bias error of ISP-IFOG for the +x and -x directions of a magnetic field are 0.47 °/h/mT and -0.50 °/h/mT are measured, respectively, in Figure 4.12. It is clearly seen that the bias error is significantly suppressed. The reason of small amount of bias is due to the fiber length of the MIOC pigtails l_1 and l_4 which are 1.5 m and same polarity axes (s polarization).

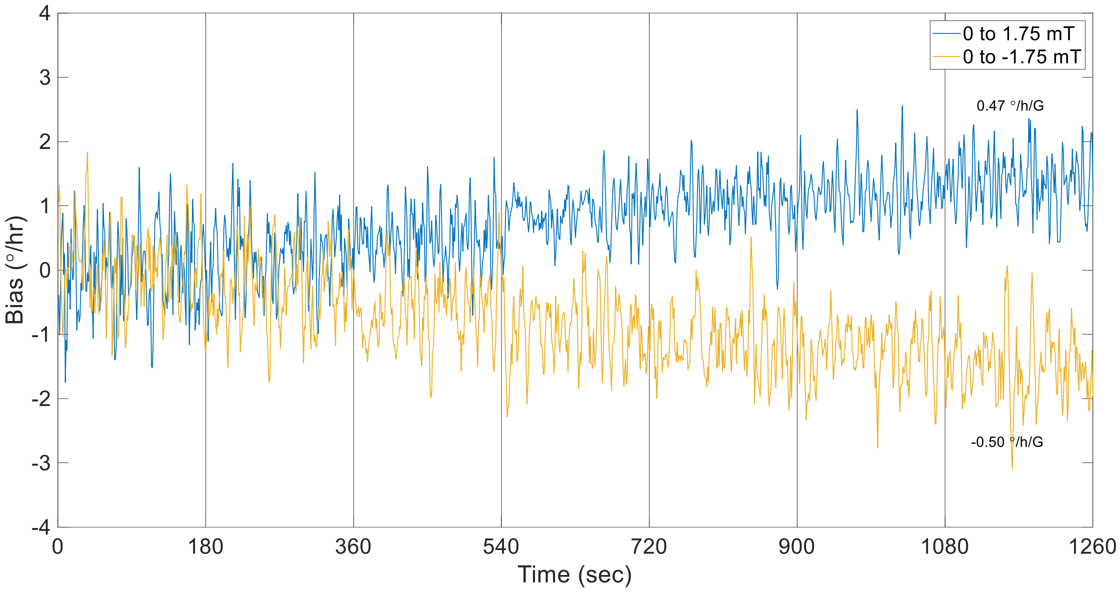

Figure 4.12. Magnetic Field induced bias error in ISP-IFOG for the +x and -x directions of a magnetic field

It can be clearly seen that the bias error of the gyroscope under a magnetic field can be reduced considerably with ISP-IFOG design. Total phase difference is equal to the sum of the phases of the light traveling through the fiber optic coil in slow and fast polarization axes according to Eq. 4.41.

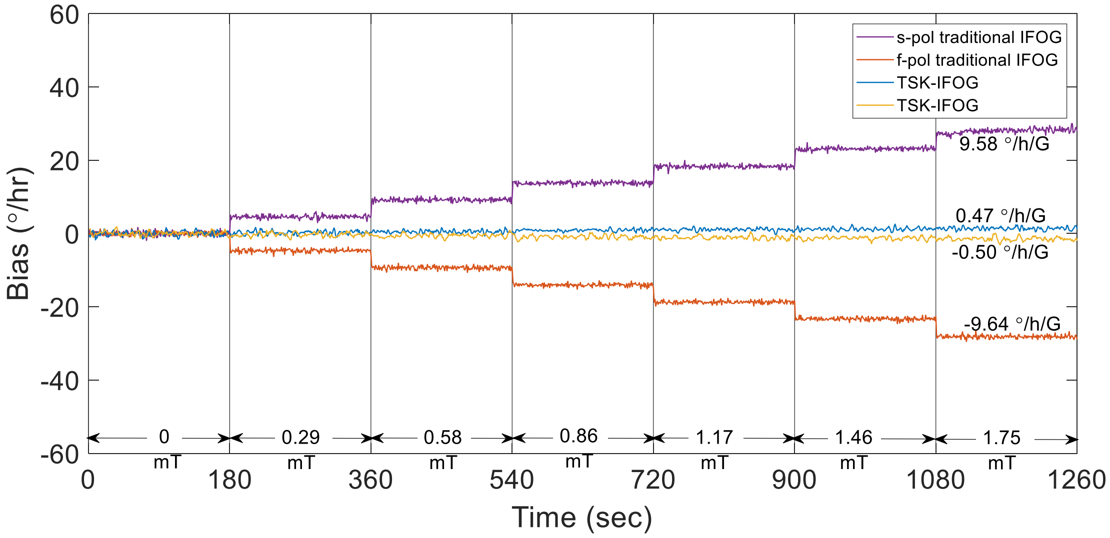

Figure 4.13. Experimental results of two different polarity axes of IFOG and ISP-IFOG recorded for the different magnetic field intensities over a period of 180 s.

Due to the fact that the slow and fast polarization axes under the magnetic field have an inverse polarization, the Faraday Effect can be greatly reduced when both the slow and fast axes that travel in the fiber optic coil are equal. This can be achieved by using two equal lengths of the fiber segments l_2 and l_3 as shown in. This is proven by theoretical analysis and verified by experimental results. According to the ISP-IFOG phase drift measurements under a magnetic field, the bias error is calculated as less than 0.50 °/h/mT of ISP-IFOG. This error can be due to the fact that both the lengths of l_2 and l_3 have small differences due to practical limitations and the lengths of l_1 and l_4 have same polarization axes.

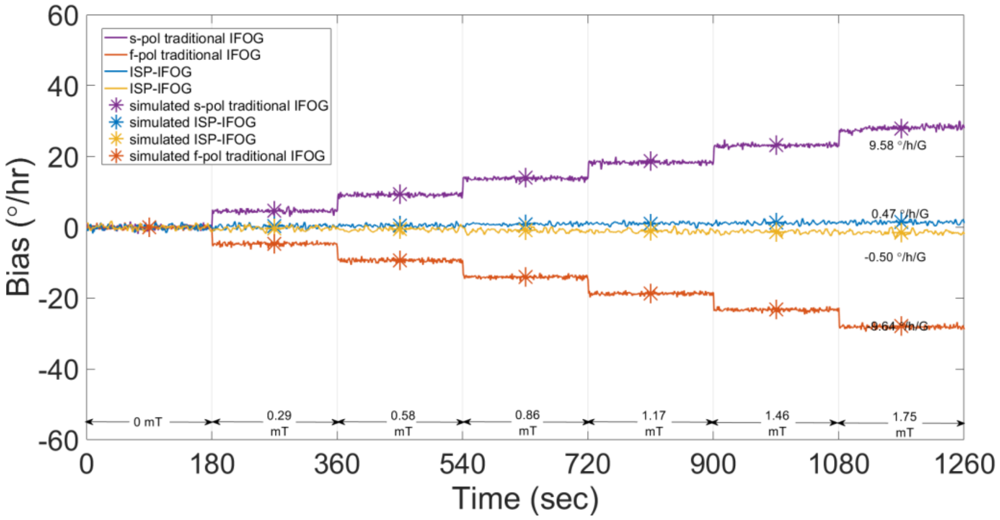

Figure 4.14. Experimental and simulation results of two different polarity axes of IFOG and ISP-IFOG recorded for the different magnetic field intensities over a period of 180 s.

The ISP-IFOG configuration is tested and shown that the radial magnetic field sensitivity is decreased considerably, without generating an optical and electronic algorithm in the IFOG system. Due to the invertible effect of the magnetic field on the polarization of the light inside the fiber, it has been observed that the Faraday Effect induced bias error in the IFOG system is suppressed ~20 times from 9.6 °/h/mT to 0.5 °/h/mT without decreasing the sensitivity of IFOG. Therefore, ISP-IFOG offers a promising way for the substantial suppression of the bias error caused by the Faraday Effect in an IFOG. This configuration also has a potential to decrease the sensitivity of the temperature dependence of phase drift [84].

The theoretical results show that the bias error caused by the Faraday effect changes with temperature in PM fiber optic coil. This phenomenon is caused by the temperature dependence of linear birefringence and the Verdet constant of the PM fiber as seen in Eqs. 4.41 and 4.42 [5].

$$\Delta\beta = \Delta\beta(T_0) + \frac{d\Delta\beta}{\Delta T}(T - T_0) \qquad 4.42$$

where $\Delta\beta = 2027\ rad/m$ at $T_0 = 20°C$ and $\frac{d\Delta\beta}{\Delta T} = -3.04\ \mathrm{rad/m/°C}$.

$$\Delta V = V(T_0) + \frac{dV}{\Delta T}(T - T_0) \qquad 4.43$$

where $V = 2027\ \mathrm{rad/m/mT}$ at $T_0 = 20°C$ and $\frac{dV}{\Delta T} = 6.04\mathrm{x}10^{-4}\ \mathrm{rad/m/mT/°C}$.

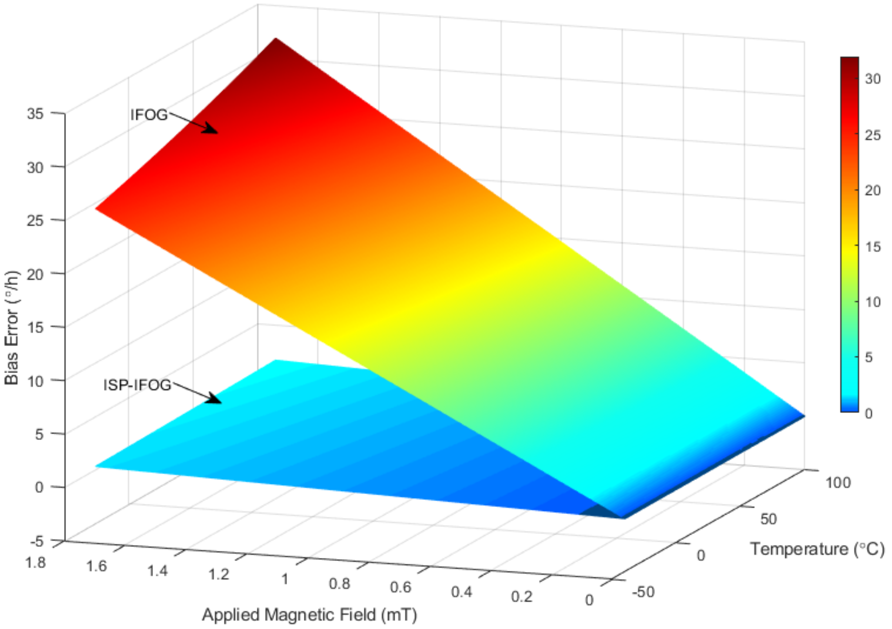

Figure 4.15. Simulation results of the temperature dependence of the bias error compared with ISP-IFOG and conventional IFOG

5 RESULTS AND DISCUSSION

In this thesis study, we proposed a low noise high performance configuration for the IFOG, that enables a light source, a MIOC and a Fiber optic coil. The first part of this thesis explores the underlying theory behind the fiber optic gyroscope based on the Sagnac interferometer. A main objective of this thesis study describes the design process of such optical parts with focus on the error reduction.

The light source has a low noise, high stability, and a wide spectral band is preferred in high performance IFOG systems. The commonly preferred light sources for fiber optic gyroscopes are fiber-based ASE source and a SLD, and these sources have been characterized as the light source providing these specifications. We propose that a spectral width of the ASE light source has been improved 62%, the temperature dependence of wavelength have been improved fourfold, and the spectral width has been improved fivefold versus the minimum configuration of the ASE light source.

The MIOC that is fabricated by the Ti-diffusion and the APE method has been characterized within the IFOG. A fiber optic coil wound with quadrupole winding pattern detailly characterized in Section-3.4. This section also gives the temperature-dependent rate measurement and performance of IFOG that includes the two MIOCs fabricated by the APE method and Ti-diffusion method integrated to the system without polarizer. The FOG performance with these two MIOCs have been analyzed and the bias error is reduced more than 20 times by using MIOC fabricated by the APE method.

In this thesis, an adhesive composition was developed to reduce random errors that occur because of mechanical stress on the fiber optic coil due to time-dependent changes in environmental conditions. The performance of FOG with a different adhesive mixture has been analyzed. The proposed adhesive mixture, includes homogeneous adhesives with high mechanical strength and moisture resistance, containing a base material, drying agent, carbon black (C), and a bifunctional organosilane-containing surface agent. The mixture obtained with the base material in an amount of 54% by weight of the total composition, the drying agent in an amount of 5% by weight, the carbon black (C) in an amount of 40% by weight and bifunctional organosilane-containing surface agent in an amount of 1% by weight on a 100% composition. Therefore, a homogeneous adhesive composition with high mechanical strength and moisture resistance is provided to the related technique and the Young Modulus of the adhesive has been improved 3 times from 2.7 MPa to 9.3 MPa with the proposed composition. For the fiber optic coil that contains the proposed adhesive material with high mechanical strength temperature-dependent rate measurements are made, rate sensitivity of the fiber optic coil is calculated as an average of 0.16 (°/h)/(°C/min) over the entire temperature range. It has been clearly observed that it has improved at least 18 times compared with the other designs.

The last part of the dissertation introduces the Faraday Effect induced bias drift suppression under Magnetic field. This achievement is clarified thorough theoretical and experimental study of the Faraday-effect-induced bias error in a FOG. On the theoretical side, the mathematical expressions are driven to analyze the suppression of the Faraday Effect induced bias drift under Magnetic Field. Prior to this work, the Faraday Effect induced bias drift can be suppressed with different methods described in a number of publications in the literature.

In this part of the thesis, a new, the best according to our knowledge in terms of performance, cost, manufacturability, and simplicity, fiber optic coil design is proposed to reduce magnetic field sensitivity without adding any optical components or electronic algorithms to the IFOG system. It is shown that this design can be applied without disturbing the simplest IFOG structure. It is verified by theoretical analysis that two orthogonal polarities caused by the Faraday Effect are effectively suppressed by the proposed method and the experimental results are in good agreement with the theoretical analysis. According to the experimental results, the bias error is reduced approximately 20 times from ±9.6 °/h/mT to ±0.5 °/h/mT.

In summary, a low-noise and high-sensitivity IFOG has been developed as the output of this thesis. During this development, many innovative studies have been carried out and these studies have made significant contributions to the literature. An article titled "Suppression of a Fiber-optic gyroscope for the Faraday-effect-induced bias error" has been published in the Optics Letters within the scope of this thesis. For future work, the investigation of the temperature dependent bias error of ISP-IFOG under a magnetic field is planned to be examined.

REFERENCES

[1] H.C. Lefevre, The Fiber-Optic Gyroscope, Artech house, 2014.

[2] X. Chen, R. Liu, in: T. Ye, S. Hu, Y. Li, X. Luo, X. Bao (Eds.), 6th International Symposium on Advanced Optical Manufacturing and Testing Technologies: Design, Manufacturing, and Testing of Smart Structures, Micro- and Nano-Optical Devices, and Systems, SPIE, 2012, pp. 410 – 415.

[3] E.J. Friebele, K.J. Long, C.G.. . Askina, M.E.. . Gingerich, M.J. Marrone, D.L. Griacom, Radiation Effects on Optical Materials 0541 (1985) 70.

[4] C. Shen, X. Chen, J. Yu, J. Wu, in: 2011 IEEE International Instrumentation and Measurement Technology Conference, 2011, pp. 1–5.

[5] G.A. Pavlath, Fiber Optic Gyros: 20th Anniversary Conference 2837 (1996) 46–60.

[6] M.J.F. Digonnet, J.N. Chamoun, in: E. Udd, G. Pickrell, H.H. Du (Eds.), 2016, p. 985204.

[7] O. Deppe, G. Dorner, S. König, T. Martin, S. Voigt, S. Zimmermann, Sensors 17 (2017) 567.

[8] Michel J.F. Digonnet, Rare-Earth-Doped Fiber Lasers and Amplifiers, 2nd ed., 2001.

[9] V.M.N. Passaro, A. Cuccovillo, L. Vaiani, M. de Carlo, C.E. Campanella, Mdpi.Com (n.d.).

[10] L. Xuyou, Z. Yong, Y. Qiang, in: Proceedings of 2008 IEEE International Conference on Mechatronics and Automation, ICMA 2008, 2008.

[11] X. Li, Y. Zhang, C. Zhang, in: Proceedings - 5th International Conference on Wireless Communications, Networking and Mobile Computing, WiCOM 2009, 2009.

[12] C. Zhang, S. Zhang, X. Pan, J. Jin, Opt Express 26 (2018).

[13] R.J.P. Menéndez, Modulation in Electronics and Telecommunications [Working Title] (2019).

[14] Digital Phase Modulator for Fiber Optic Sagnac Interferometer, US5137359A, 1991.

[15] W. Burns, Chin-Lin Chen, R. Moeller, Journal of Lightwave Technology 1 (1983) 98–105.

[16] J.L. Wagener, M.J.F. Digonnet, H.J. Shaw, Journal of Lightwave Technology 15 (1997) 1689–1694.

[17] T. Kumagai, N. Ashizuka, H. Nakai, H. Kajioka, Opt Laser Technol 25 (1993) 263.

[18] Y. Korkishko, … V.F.-I.O., undefined 2003, Spiedigitallibrary.Org 4944 (2003) 262.

[19] Y. Wang, L. Ren, J. Xu, … J.L.-A.M., undefined 2014, Trans Tech Publ (n.d.).

[20] Z. Yu, J. Yang, Y. Yuan, H. Zhang, … S.T.-I.T., undefined 2018, Ieeexplore.Ieee.Org (n.d.).

[21] S. Dönertaş, M. Gökkavas, … E.Ö.-G.U.J. of, undefined 2021, Dergipark.Org.Tr 8 (2021) 135–145.

[22] E. Wooten, K. Kissa, … A.Y.-Y.-I.J. of, undefined 2000, Ieeexplore.Ieee.Org (n.d.).

[23] J. Liu, C. Zhang, Y. Zheng, … J.S.-J. of L., undefined 2020, Ieeexplore.Ieee.Org (n.d.).

[24] U. Tripathi, N. Dixit, … A.K.-, & I.R., Sensorsresearchsociety.Org (n.d.).

[25] Y. Li, T. Lan, D. Yang, M. Xiang, J. Dai, … C.L.-M.R., undefined 2020, Iopscience.Iop.Org (2020).

[26] J. Yao, K. Li, B. Li, C. Wang, C. Kan, … X.S.-J. of L., undefined 2018, Osapublishing.Org (n.d.).

[27] J. Yang, Y. Yuan, A. Zhou, J. Cai, … C.L.-J. of L., undefined 2014, Ieeexplore.Ieee.Org (n.d.).

[28] A. Cordova, R.A. Patterson, J. Rahn, L.K. Lam, D.M. Rozelle, in: Fiber Optic Gyros: 20th Anniversary Conference, 1996.

[29] Z. Li, Z. Meng, T. Liu, X.S. Yao, Opt Express 21 (2013).

[30] US532349A Method for Tuning Fiber Optic Sensor Coils, n.d.

[31] US5506923 Apparatus and Method for Trimming of Fiber Optic Winding, n.d.

[32] Z. Meng, X. Steve Yao, Z. Li, Z. Ding, L. Wang, al Zhuo Meng, J. Can, J. Xu, T. Liu, Https://Doi.Org/10.1117/12.975222 8421 (2012) 1353–1356.

[33] US5847829A Reduction of Fiber Optic Gyroscope Vibration and Temperature-Ramp Sensitivities by Controlling Coil Geometrical Parameters, n.d.

[34] US5546482 Potted FOG Sensor Coil for Stringent Vibration and Thermal Environments, n.d.

[35] US6980709 Polymeric Material with Voids That Compress to Allow the Polymeric Material to Absorb Applied Force and Decrease Reaction Force to One or More Sensor Fibers, n.d.

[36] US5486922 Sensor Coil with Thermomechanically-Matched Spool for Fiber Optic Gyroscope, n.d.

[37] US6980709 Polymeric Material with Voids That Compress to Allow the Polymeric Material to Absorb Applied Force and Decrease Reaction Force to One or More Sensor Fibers, n.d.

[38] US6898364B Buffer Layer Promotion of Decrease of One or More Strain Gradients in Optical Fiber Winding, n.d.

[39] US5973783 Fiber Optic Gyroscope Coil Lead Dressing and Method for Forming the Same, n.d.

[40] H. Keskin, H.A. Vural, B. Altinöz, Ü. Bektik, H. Altan, J Sens 2022 (2022).

[41] NATO-RTO, Rto-Ag-339 Ac/323(Sci)Tp/9 323 (1999).

[42] R. Bergh, H. Lefevre, H. Shaw, Journal of Lightwave Technology 2 (1984) 91–107.

[43] J.L. Davis, S. Ezekiel, in: S. Ezekiel, G.E. Knausenberger (Eds.), 1978, pp. 131–136.

[44] S.W. Lloyd, M.J.F. Digonnet, S. Fan, Journal of Lightwave Technology 31 (2013).

[45] R.A. Bergh, H.C. Lefevre, H.J. Shaw, Opt Lett 7 (1982).

[46] J.N. Chamoun, M.J.F. Digonnet, Journal of Lightwave Technology 33 (2015).

[47] N.J. Frigo, H.F. Taylor, L. Goldberg, J.F. Weller, S.C. Rashleigh, in: 1983.

[48] A. Cordova, R.A. Patterson, E.L. Goldner, D.M. Rozelle, in: R.P. DePaula (Ed.), 1994, pp. 164–180.

[49] B.Bednarz, Fiber Optic Sensing Coil, n.d.

[50] R. Ulrich, Opt Lett 5 (1980) 173.

[51] E. Jones, W. Parker, Electron Lett 22 (1986) 54–56.

[52] K. Böhm, P. Marten, K. Petermann, E. Weidel, R. Ulrich, Electron Lett 17 (1981) 352–353.

[53] Z. Wang, Y. Yang, Y. Li, X. Yu, Z. Zhang, Z. Li, Opt Express 20 (2012) 25421.

[54] C. Peng, Y. Yang, D. Zhao, Z. Zhang, Z. Li, Z. Wang, P. Lu, C. Liu, Optics Express, Vol. 22, Issue 5, Pp. 4908-4919 22 (2014) 4908–4919.

[55] S.L.A. Carrara, B.Y. Kim, H.J. Shaw, Opt Lett 12 (1987) 214.

[56] B. Szafraniec, J. Blake, Journal of Lightwave Technology 12 (1994) 1679–1684.

[57] D.S.-A. optics, undefined 1980, Opg.Optica.Org (n.d.).

[58] F. Mohr, F. Schadt, F. Schadtb, Https://Doi.Org/10.1117/12.566654 5502 (2004) 410–413.

[59] H.J. Arditty, H.C. Lefèvre, Opt Lett 6 (1981) 401.

[60] H.C. Lefèvre, The Fiber-Optic Gyroscope, 2014.

[61] K. Hotate, K. Tabe, Appl Opt 25 (1986) 1086.

[62] V.L.-J. of C.T. and, undefined 2006, Springer 51 (2006) 836–840.

[63] J. Noda, T. Hosaka, Y. Sasaki, R.U.-E. letters, undefined 1984, Ieeexplore.Ieee.Org (n.d.).

[64] P. Kumar, G. Purohit, J. Nayak, T. Srinivas, Journal of Optics (India) 41 (2012) 231–234.

[65] J. Cruz, M. Andres, M.H.-A. optics, undefined 1996, Osapublishing.Org (n.d.).

[66] P. Liu, X. Li, X. Guang, Z. Xu, W. Ling, H. Yang, Opt Commun 394 (2017) 122–128.

[67] I.A. Andronova, G.B. Malykin, Physics-Uspekhi 45 (2002) 793–817.

[68] Amado Cordova, US5371593 Sensor Coil for Low Bias Fiber Optic Gyroscope, 1992.

[69] G.P. Agrawal, Nonlinear Fiber Optics, 2019.

[70] F. Mohr, Journal of Lightwave Technology 14 (1996).

[71] N.J. Frigo, in: Fiber Optic and Laser Sensors I, 1983.

[72] S. Blin, H.K. Kim, M.J.F. Digonnet, G.S. Kino, Journal of Lightwave Technology 25 (2007).

[73] V. Dangui, H.K. Kim, M.J.F. Digonnet, G.S. Kino, Opt Express 13 (2005).

[74] H.C. Lefevre, in: E. Udd, H.C. Lefevre, K. Hotate (Eds.), Fiber Optic Gyros: 20th Anniversary Conference, SPIE, 1996, pp. 2 – 17.

[75] Y. Zhao, Y. Zhou, D. Zhang, J. Yang, Y. Zhou, S. Shi, X. Shu, C. Liu, IEEE Sens J 15 (2015) 5128–5132.

[76] Y. Zhou, Y. Zhao, D. Zhang, X. Shu, S. Che, Sci Rep 8 (2018).

[77] K. Böhm, K. Petermann, E. Weidel, Opt Lett 7 (1982) 180.

[78] H. Wen, M.A. Terrel, H.K. Kim, M.J.F. Digonnet, S. Fan, Journal of Lightwave Technology 27 (2009) 3194–3201.

[79] Y. Yang, Z. Wang, Z. Li, Opt Lett 37 (2012) 2841.

[80] Y. Zhou, Y. Zhao, H. Tian, D. Zhang, T. Huang, L. Miao, X. Shu, S. Che, C. Liu, Optical Engineering 55 (2016) 126106.

[81] T. Saida, K. Hotate, Journal of Lightwave Technology 17 (1999) 222.

[82] T. Okoshi, Journal of Lightwave Technology 2 (1984).

[83] K. Hotate, K. Tabe, Appl. Opt. 25 (1986) 1086–1092.

[84] A. Yertutanol, Ö. Akçaalan, S. Öğüt, E. Özbay, A. Ceylan. Optics Letters, Vol. 46, Issue 17, Pp. 4328-4331 46 (2021) 4328–4331.

APPENDIX

APPENDIX-1 SIMULARTION PARAMETERS

VPI Photonics simulation parameters that studied in this thesis are placed below. The doped fiber parameters are listed below (Figure 0.1 and Figure 0.2).

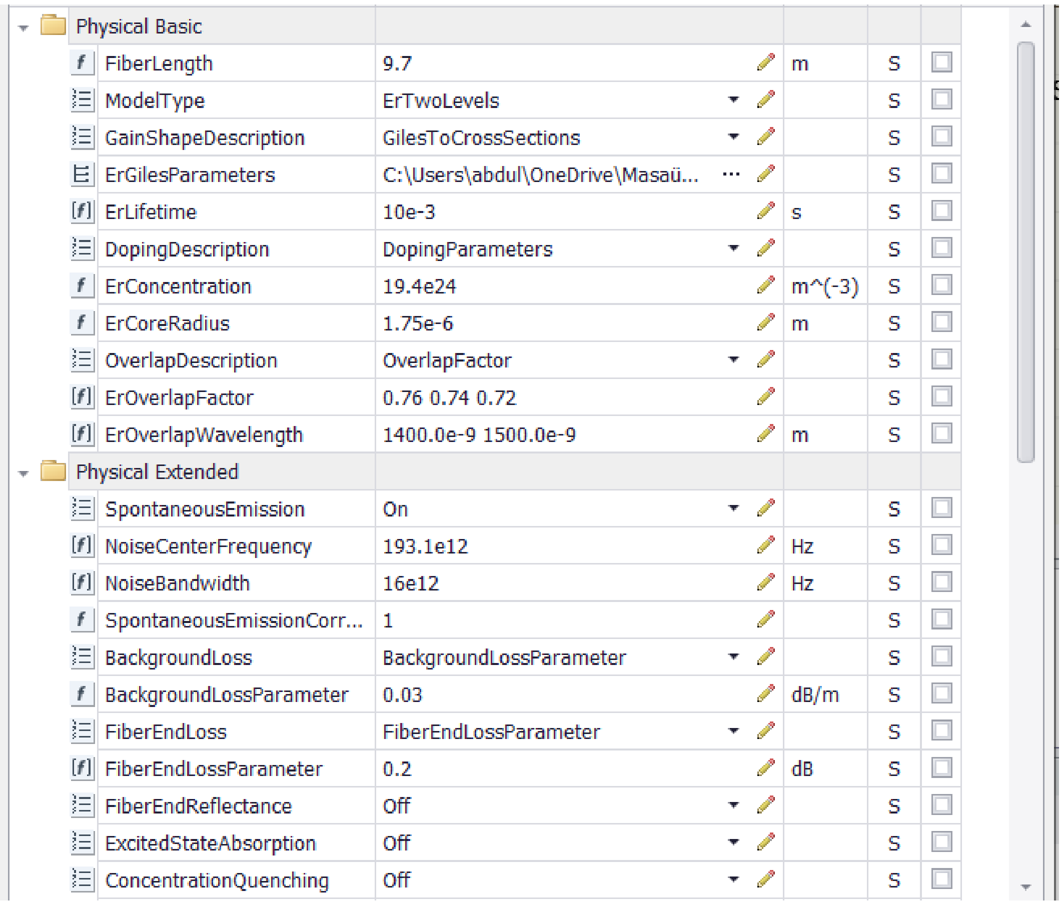

Physical Basic				
FiberLength	9.7	m	S	☐
ModelType	ErTwoLevels		S	☐
GainShapeDescription	GilesToCrossSections		S	☐
ErGilesParameters	C:\Users\abdul\OneDrive\Masaü...		S	☐
ErLifetime	10e-3	s	S	☐
DopingDescription	DopingParameters		S	☐
ErConcentration	19.4e24	m^(-3)	S	☐
ErCoreRadius	1.75e-6	m	S	☐
OverlapDescription	OverlapFactor		S	☐
ErOverlapFactor	0.76 0.74 0.72		S	☐
ErOverlapWavelength	1400.0e-9 1500.0e-9	m	S	☐
Physical Extended				
SpontaneousEmission	On		S	☐
NoiseCenterFrequency	193.1e12	Hz	S	☐
NoiseBandwidth	16e12	Hz	S	☐
SpontaneousEmissionCorr...	1		S	☐
BackgroundLoss	BackgroundLossParameter		S	☐
BackgroundLossParameter	0.03	dB/m	S	☐
FiberEndLoss	FiberEndLossParameter		S	☐
FiberEndLossParameter	0.2	dB	S	☐
FiberEndReflectance	Off		S	☐
ExcitedStateAbsorption	Off		S	☐
ConcentrationQuenching	Off		S	☐

Figure 0.1. Doped fiber parameters

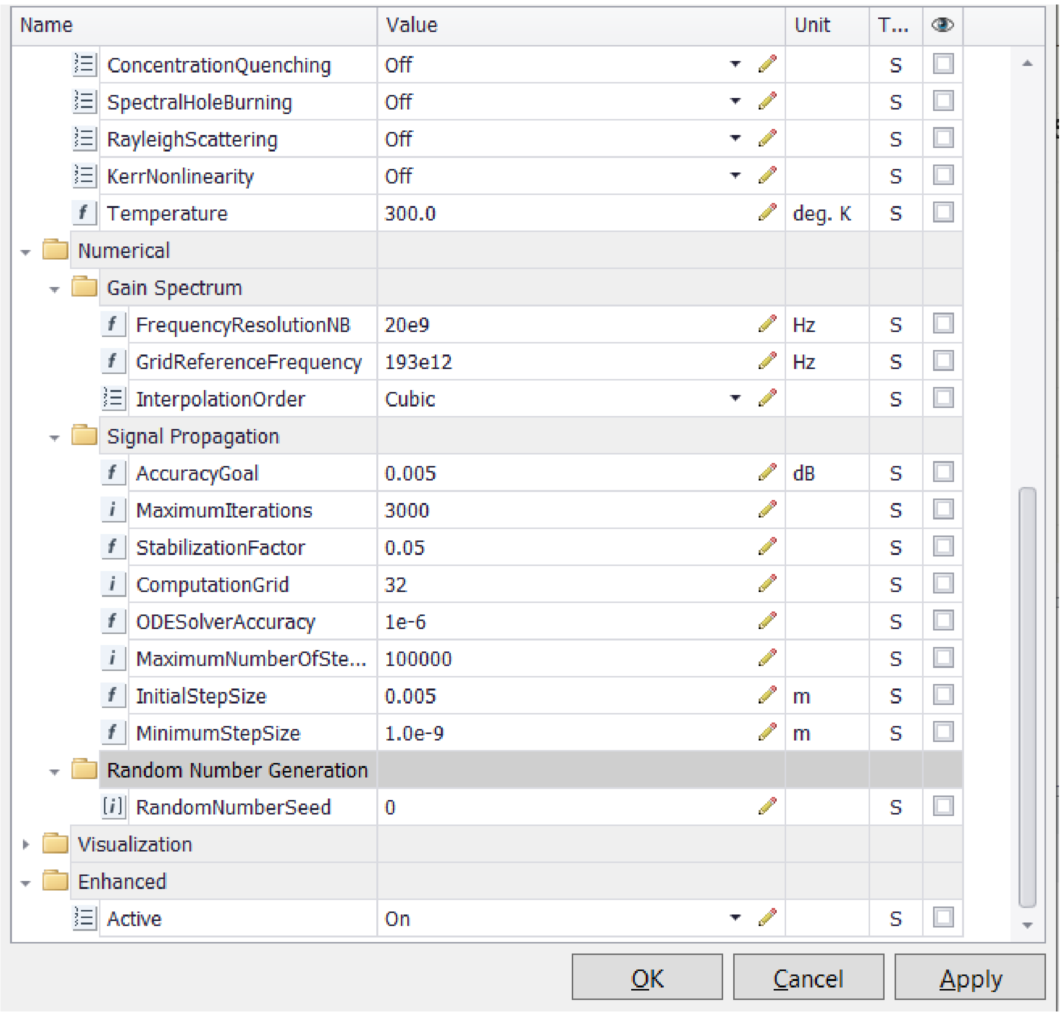

Name	Value	Unit	T...	
ConcentrationQuenching	Off		S	☐
SpectralHoleBurning	Off		S	☐
RayleighScattering	Off		S	☐
KerrNonlinearity	Off		S	☐
Temperature	300.0	deg. K	S	☐
Numerical				
Gain Spectrum				
FrequencyResolutionNB	20e9	Hz	S	☐
GridReferenceFrequency	193e12	Hz	S	☐
InterpolationOrder	Cubic		S	☐
Signal Propagation				
AccuracyGoal	0.005	dB	S	☐
MaximumIterations	3000		S	☐
StabilizationFactor	0.05		S	☐
ComputationGrid	32		S	☐
ODESolverAccuracy	1e-6		S	☐
MaximumNumberOfSte...	100000		S	☐
InitialStepSize	0.005	m	S	☐
MinimumStepSize	1.0e-9	m	S	☐
Random Number Generation				
RandomNumberSeed	0		S	☐
Visualization				
Enhanced				
Active	On		S	☐

Figure 0.2. Doped fiber parameters

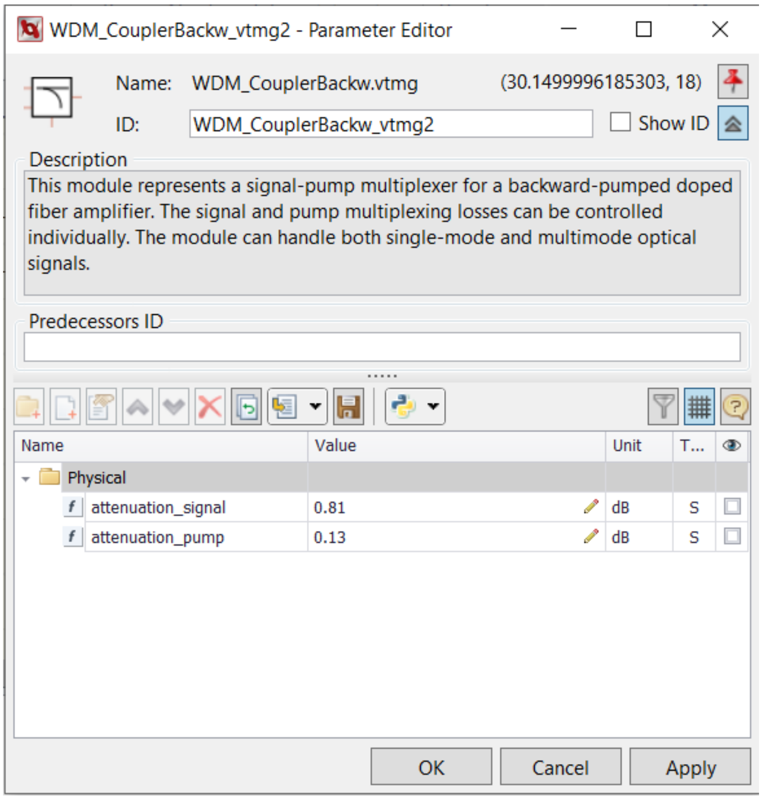

WDM_CouplerBackw_vtmg2 - Parameter Editor

Name: WDM_CouplerBackw.vtmg (30.1499996185303, 18)

ID: WDM_CouplerBackw_vtmg2 ☐ Show ID

Description

This module represents a signal-pump multiplexer for a backward-pumped doped fiber amplifier. The signal and pump multiplexing losses can be controlled individually. The module can handle both single-mode and multimode optical signals.

Predecessors ID

Name	Value	Unit	T...	👁
Physical				
attenuation_signal	0.81	dB	S	☐
attenuation_pump	0.13	dB	S	☐

Figure 0.3. WDM parameters

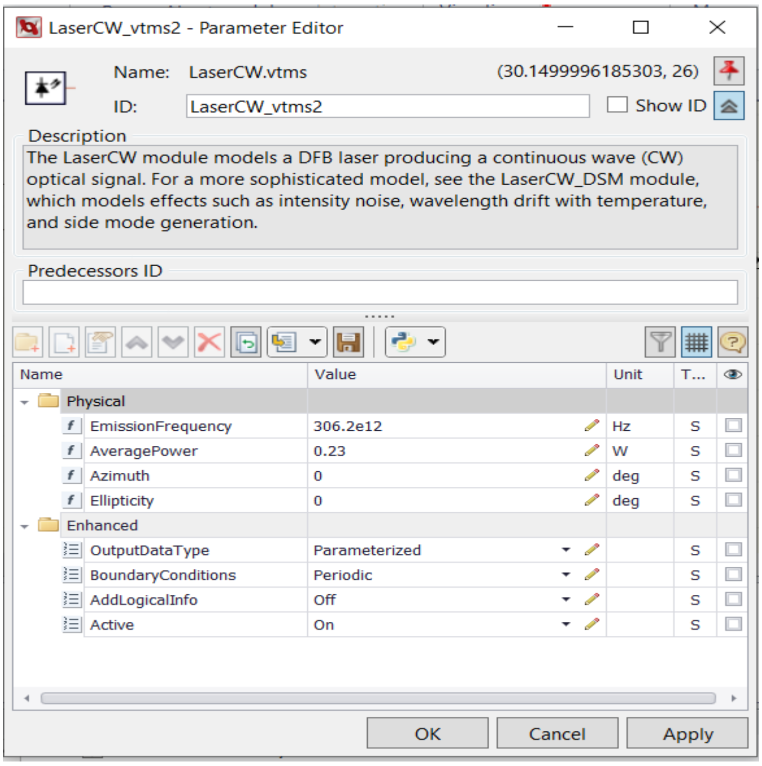

LaserCW_vtms2 - Parameter Editor

Name: LaserCW.vtms (30.1499996185303, 26)

ID: LaserCW_vtms2 ☐ Show ID

Description

The LaserCW module models a DFB laser producing a continuous wave (CW) optical signal. For a more sophisticated model, see the LaserCW_DSM module, which models effects such as intensity noise, wavelength drift with temperature, and side mode generation.

Predecessors ID

Name	Value	Unit	T...	👁
Physical				
EmissionFrequency	306.2e12	Hz	S	☐
AveragePower	0.23	W	S	☐
Azimuth	0	deg	S	☐
Ellipticity	0	deg	S	☐
Enhanced				
OutputDataType	Parameterized		S	☐
BoundaryConditions	Periodic		S	☐
AddLogicalInfo	Off		S	☐
Active	On		S	☐

Figure 0.4. Laser diode parameters

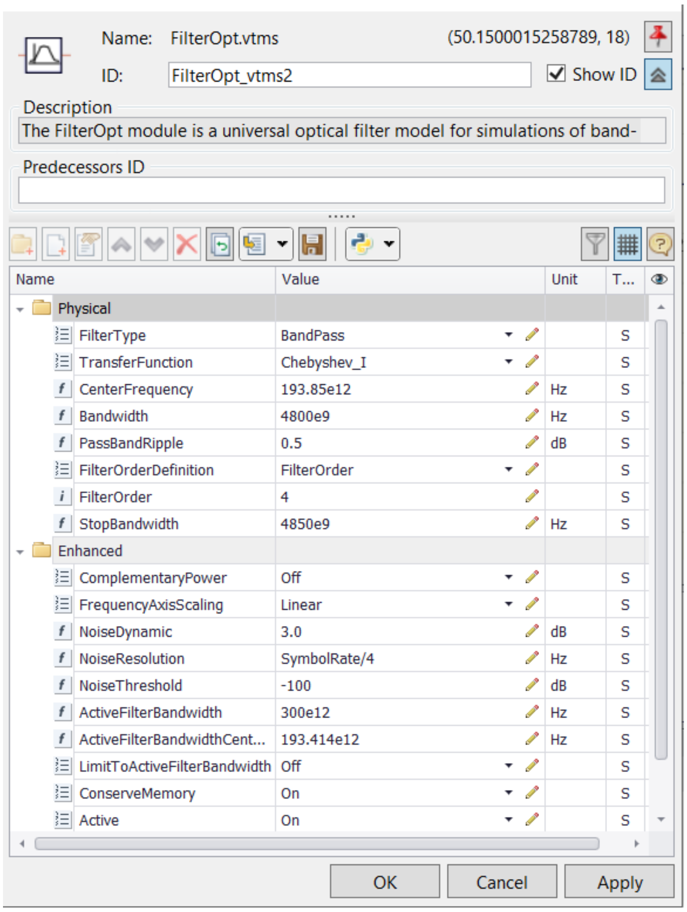

Name: FilterOpt.vtms (50.1500015258789, 18)

ID: FilterOpt_vtms2 ☑ Show ID

Description

The FilterOpt module is a universal optical filter model for simulations of band-

Predecessors ID

Name	Value	Unit	T...
Physical			
FilterType	BandPass		S
TransferFunction	Chebyshev_I		S
CenterFrequency	193.85e12	Hz	S
Bandwidth	4800e9	Hz	S
PassBandRipple	0.5	dB	S
FilterOrderDefinition	FilterOrder		S
FilterOrder	4		S
StopBandwidth	4850e9	Hz	S
Enhanced			
ComplementaryPower	Off		S
FrequencyAxisScaling	Linear		S
NoiseDynamic	3.0	dB	S
NoiseResolution	SymbolRate/4	Hz	S
NoiseThreshold	-100	dB	S
ActiveFilterBandwidth	300e12	Hz	S
ActiveFilterBandwidthCent...	193.414e12	Hz	S
LimitToActiveFilterBandwidth	Off		S
ConserveMemory	On		S
Active	On		S

Figure 0.5. Isolator parameters

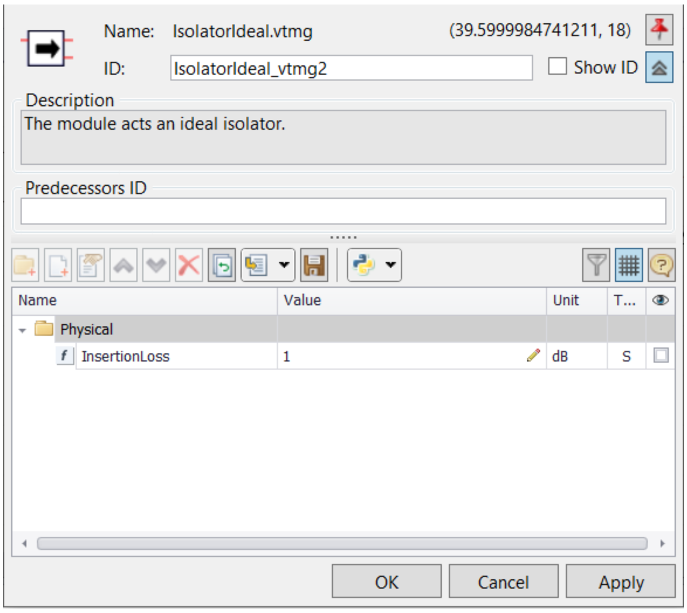

Name: IsolatorIdeal.vtmg (39.5999984741211, 18)

ID: IsolatorIdeal_vtmg2 ☐ Show ID

Description

The module acts an ideal isolator.

Predecessors ID

Name	Value	Unit	T...
Physical			
InsertionLoss	1	dB	S

Figure 0.6. Isolator parameters

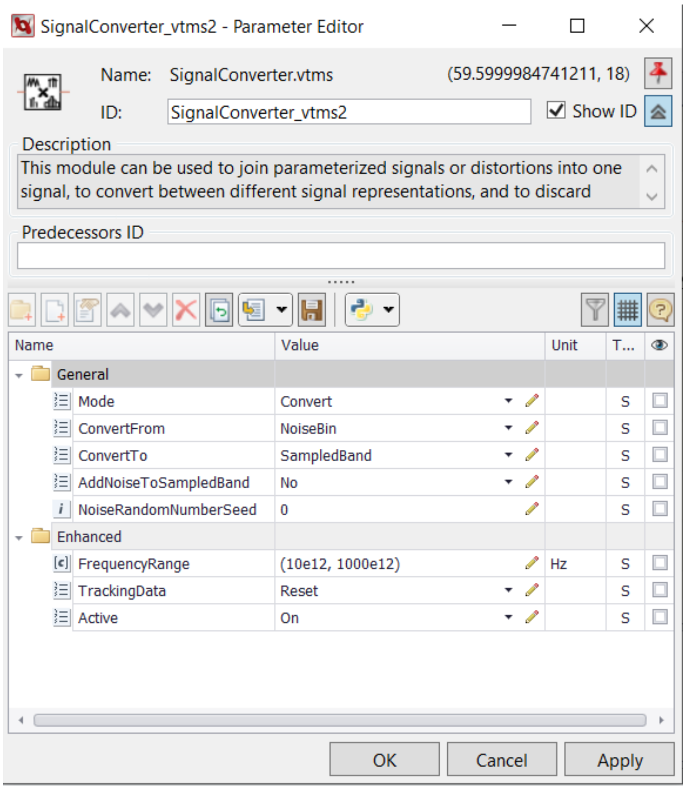

SignalConverter_vtms2 - Parameter Editor

Name: SignalConverter.vtms (59.5999984741211, 18)

ID: SignalConverter_vtms2 ☑ Show ID

Description

This module can be used to join parameterized signals or distortions into one signal, to convert between different signal representations, and to discard

Predecessors ID

Name	Value	Unit	T...
General			
Mode	Convert		S
ConvertFrom	NoiseBin		S
ConvertTo	SampledBand		S
AddNoiseToSampledBand	No		S
NoiseRandomNumberSeed	0		S
Enhanced			
FrequencyRange	(10e12, 1000e12)	Hz	S
TrackingData	Reset		S
Active	On		S

Figure 0.7. Signal Converter parameters

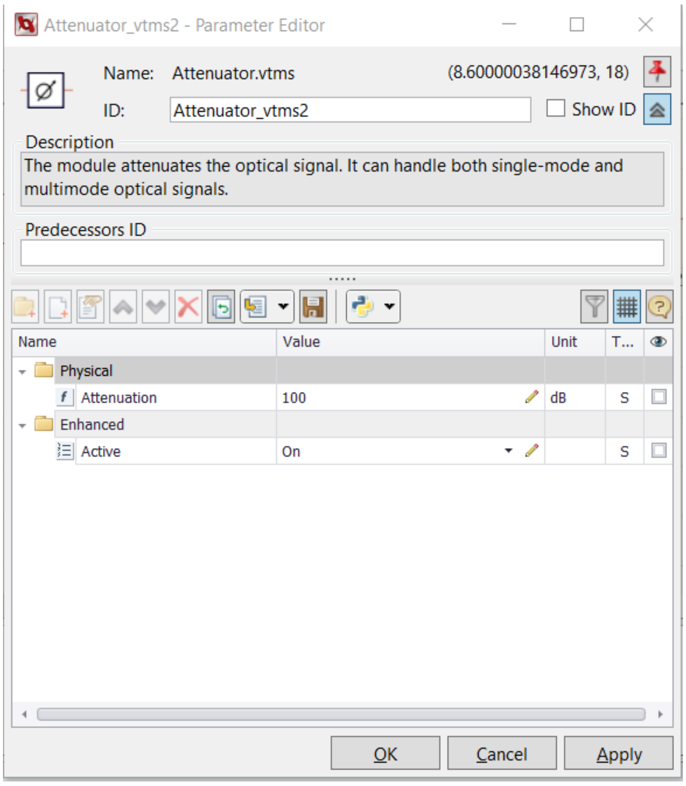

Attenuator_vtms2 - Parameter Editor

Name: Attenuator.vtms (8.60000038146973, 18)

ID: Attenuator_vtms2 ☐ Show ID

Description

The module attenuates the optical signal. It can handle both single-mode and multimode optical signals.

Predecessors ID

Name	Value	Unit	T...
Physical			
Attenuation	100	dB	S
Enhanced			
Active	On		S

Figure 0.8. Attenuator parameters

APPENDIX-2 ALGORITHMS

Algorithm 0.1. Matlab code for bias error calculations

```
hold on
clear all
%constants
   r=0.0425; %0.0425; %radius of coil (m)
   beta=5000; %Birefrigence (rad/m)
   m=80*48; %80*48/330; %fiber turn of coil
   fiber_diam=0.170 % fiber diameter(mm)
   n=1; %index of matrix
   H=1.7 % Magnetic Field (mT)
   V= 6.0168*10^-4 ;%Verdet constnt (rad/mT/m)
   zeta=0.0002; %faraday rotation per unit length (rad/m) 6*10^-4 per 20deg

  %tps (Twist Power Spectrum) rad^2/m^2
  tps=150; %W
  n=1;
   for i=0:0.29:1.75;
      H(n)=i;
      delta(n)=(8*V*H(n)*r)*sqrt(2*m*pi()*tps)/beta.*206265 % drift *206265 (deg/hr), (rad)
      n=n+1;
   end

   time=0:180:1260-90;
   time=time/180*0.29
   figure;
   plot(time,delta)
   ylabel (‘Drift (\circ/h)’),xlabel(‘Magnetic Field (mT)’)
   grid on
```

Algorithm 0.2. Matlab code for bias error calculations under thermal variation

```
hold on
clear all
%constants
    r=0.0425; %0.0425; %radius of coil (m)
    beta0=2027; %Birefrigence (rad/m)
    m=80*48; %80*48/330; %fiber turn of coil
    fiber_diam=0.170; % fiber diameter (mm)
    H=1.7;% Magnetic Field (mT)
    V0= 6.0168*10^-4; %Verdet constnt (rad/mT/m) at 20C
    %zeta=0.0002; %faraday rotation per unit length (rad/m) 6*10^-4 per 20deg
   T0=20; %C

   tps=24.6524; %W %tps (Twist Power Spectrum) rad^2/m^2
   nn=1;
   for j=-40:10:100
       V(nn)= V0 + 4.2*10^(-8)*(j-T0); % dV/dT: 4.2*10^(-8)rad/m/mT/C
       beta(nn)= beta0 + (-3.04)*(j-T0); % dbeta/dT: -3.04 rad/m/C
       n=1;
    for i=0:0.29:2;
        temp(nn)=j;
        H(n)=i;
        delta(nn,n)=(8*V(nn)*H(n)*r)*sqrt(2*m*pi()*tps)/beta(nn).*206265;  %  drift  *206265
(deg/hr), (rad)
        n=n+1;
    end
    nn=nn+1;
   end
   delta
%     time=0:180:1260-90;
%     time=time/180*0.29
%     figure;
%     plot(time,delta)
%     ylabel (‘Drift (\circ/h)’),xlabel(‘Magnetic Field (mT)’)
%     grid on
  hold on
figure;
xlin=linspace(min(H),max(H),500);
ylin=linspace(min(temp),max(temp),500);
[X,Y]=meshgrid(xlin,ylin);
Z=griddata(H,temp,delta,X,Y,’cubic’);
mesh(Y,X,Z);
figure;
contour(Y,X,Z)

figure; plotyy(temp,beta,temp,V)
```

APPENDIX-3 Thesis Derived Publications

- Yertutanol, A., Akçaalan, Ö., Öğüt, S., Özbay, E., & Ceylan, A. (2021). Fiber-optic gyroscope for the suppression of a Faraday-effect-induced bias error. Optics Letters, 46(17), 4328-4331.
- High Performance Navigation Grade IFOG with a Fiber optic coil with Reduced Mechanical Stress, 2021, 22. Ulusal Optik, Elektro-Optik ve Fotonik Çalıştayı, Aylin Yertutanol, Tuğba Andaç, Serdar Öğüt, Ekmel Özbay and Abdullah Ceylan
- All-Fiber Er-Doped ASE Source for Fiber Optic Sensors, FOTONİK 2018 | 20. Ulusal Optik, Elektro-Optik ve Fotonik Çalıştayı, Aylin Yertutanol, Önder Akçaalan, Serdar Öğüt and Ekmel Özbay
- Performance Characterization of Different Fiber Optic Gyroscope Coils, FOTONİK 2019 | 21. Ulusal Optik, Elektro-Optik ve Fotonik Çalıştayı, Tuğba Andaç, Aylin Yertutanol, Serdar Öğüt, Abdullah Ceylan and Ekmel Özbay
- Manyetik Alan Duyarlılığı Azaltılmış Fiber Optik Dönüölçer, FOTONİK 2019 | 21. Ulusal Optik, Elektro-Optik ve Fotonik Çalıştayı, Aylin Yertutanol, Önder Akçaalan, Serdar Öğüt, Abdullah Ceylan ve Ekmel Özbay